



Cite as  
Nano-Micro Lett.  
(2021) 13:38

## Strategy and Future Prospects to Develop Room-Temperature-Recoverable NO<sub>2</sub> Gas Sensor Based on Two-Dimensional Molybdenum Disulfide

Abhay V. Agrawal<sup>1</sup>, Naveen Kumar<sup>1</sup>, Mukesh Kumar<sup>1</sup> ✉

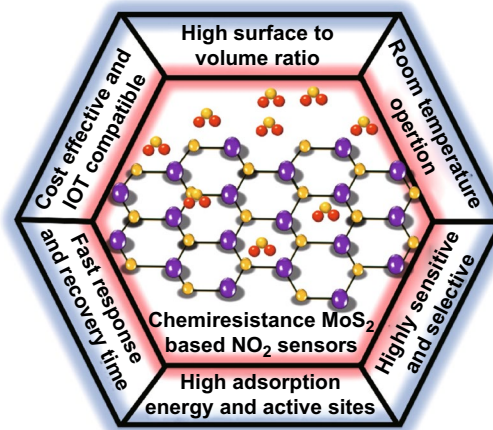
Received: 26 August 2020  
Accepted: 29 October 2020  
© The Author(s) 2020

### HIGHLIGHTS

- MoS<sub>2</sub> shows enormous potential for gas sensing due to its high surface to volume ratio, position-dependent gas molecules adsorption and easy control on morphology.
- The recent experimental and theoretical strategies to develop NO<sub>2</sub> chemiresistance sensors based on MoS<sub>2</sub> are addressed.
- A detailed overview of the fabrication of MoS<sub>2</sub> chemiresistance sensors in terms of devices, structure, morphology, defects, heterostructures, metal doping, and under light illumination are discussed.

**ABSTRACT** Nitrogen dioxide (NO<sub>2</sub>), a hazardous gas with acidic nature, is continuously being liberated in the atmosphere due to human activity. The NO<sub>2</sub> sensors based on traditional materials have limitations of high-temperature requirements, slow recovery, and performance degradation under harsh environmental conditions. These limitations of traditional materials are forcing the scientific community to discover future alternative NO<sub>2</sub> sensitive materials. Molybdenum disulfide (MoS<sub>2</sub>) has emerged as a potential candidate for developing next-generation NO<sub>2</sub> gas sensors. MoS<sub>2</sub> has a large surface area for NO<sub>2</sub> molecules adsorption with controllable morphologies, facile integration with other materials and compatibility with internet of things (IoT) devices. The aim of this review is to provide a detailed overview of the fabrication of MoS<sub>2</sub> chemiresistance sensors in terms of devices (resistor and transistor), layer thickness, morphology control, defect tailoring, heterostructure, metal nanoparticle doping, and through light illumination. Moreover, the experimental and theoretical aspects used in designing MoS<sub>2</sub>-based NO<sub>2</sub> sensors are also discussed extensively. Finally, the review concludes the challenges and future perspectives to further enhance the gas-sensing performance of MoS<sub>2</sub>. Understanding and addressing these issues are expected to yield the development of highly reliable and industry standard chemiresistance NO<sub>2</sub> gas sensors for environmental monitoring.

**KEYWORDS** MoS<sub>2</sub>; NO<sub>2</sub> gas sensors; Light illumination; Heterojunction



✉ Mukesh Kumar, [mkumar@iitrr.ac.in](mailto:mkumar@iitrr.ac.in)

<sup>1</sup> Functional and Renewable Energy Materials Laboratory, Indian Institute of Technology Ropar, Rupnagar, Punjab 140001, India



## 1 Introduction

The earth's environment consists of various chemical elements, gases, and dust particles such as  $N_2$ ,  $O_2$ ,  $CO$ ,  $CO_2$ ,  $NO_2$ ,  $NH_3$ . Among these gases,  $O_2$ , present in the environment is beneficial to living beings, while some gases, such as  $CO_2$ ,  $NO_2$ , are toxic and dangerous. The presence of these toxic gases is majorly fixed in the environment. Among all toxic and dangerous gases,  $NO_2$ , a hazardous gas, acidic in nature, highly reactive with a stinky smell is continuously being produced and liberated in the atmosphere due to human activity [1–6].  $NO_2$  is produced by fossil fuel burning, forest fires, industry and motor vehicles [7–9].  $NO_2$  has recently become a matter of concern in Europe and Australia, owing to its increased concentration. The recent satellite data revealed an unprecedented increase in  $NO_2$  concentration due to motor vehicles, power plants and wildfire in Europe and Australia in the year 2019 [10–14]. Moreover, after the worldwide outbreak of the novel COVID-19 virus, the lockdown was implemented in highly affected countries, which resulted in the shutdown of factories, manufacturing firms, and transport. This lockdown benefitted the world inadvertently with a dramatic reduction in  $NO_2$  emissions. Importantly, the high reactivity of  $NO_2$  molecules with moisture and its tendency to create an acidic environment makes  $NO_2$  production thought of concern [5, 15, 16]. It causes respiratory diseases beyond a certain  $NO_2$  concentration limit in the environment, e.g. coronary assault, cancer, asthma, pneumonia, coughing and bronchitis [16–18]. The presence of  $NO_2$  in the environment makes the air hazy and thick, which reduces the visibility of human eyes. In addition, the World Health Organization (WHO) reported that major cities around the world had failed to qualify the WHO's air quality standards [19]. An estimated 30.7 million people died due to cardiovascular disease, cancer and chronic respiratory disease in 2016 [19, 20]. Thus, considering the toxicity and hazardousness of  $NO_2$  gas, there is an urgent need to detect the precise levels of  $NO_2$  gas in the environment.

A hazardous gas in the environment can be detected by a gas sensor which is an electronic device having two-essential parts; a receptor unit and a transducer unit. Chemical information generated due to gas molecules exposure is gathered and stored in the form of chemical energy in the receptor device. The energy stored in the transducer component is

transmuted to an analytical signal [21]. Hulanicki et al. categorized the gas sensors into six classes depending on the transducer mechanism: (1) electrochemical, (2) mass sensitive, (3) magnetic, (4) optical, (5) thermoelectric, and (6) electrical. The classification of gas sensors is carried out on the basis of their transducer operating principle. In today's fast moving and unstoppable life, the rapid detection of low concentration of toxic gases is indispensable. Among all gas sensors, electrical transducer-based  $NO_2$  gas sensor has grabbed the prime attention due to their easy handling, simple fabrication process, easy to connect with IOTs, real-time gas detection provision, low-cost and power consumptions, small size and long-term stability in harsh working conditions. In electrical or chemical resistance sensors, the resistance of the sensing material is changed due to charge transfer between the gas molecules and the sensing materials whenever the gas molecules are exposed to the sensing device. The chemiresistance gas sensors have extensive applications in  $H_2$ ,  $NH_3$ ,  $NO$ ,  $H_2S$ ,  $NO_2$  gas detection in the environment, industry, cities, space science, transport, vehicles, cultivation, indoors, and various health sectors [22, 23]. Some figures of merits are specified to compare the performance of a gas sensor with different sizes, morphologies and operating conditions, i.e. sensor response, response and recovery time, and selectivity. Generally, sensor response is the ratio of change in resistance with exposure of gas molecules to the resistance of the film before the exposure of gas molecules. It is given by different forms of expression by many groups such as  $S = \frac{(R_{gas}-R_{air})}{R_{air}}$ ;  $\frac{(R_{air}-R_{gas})}{R_{air}}$ ;  $\frac{(I_{gas}-I_{air})}{I_{air}}$ ;  $\frac{R_{gas}}{R_{air}}$ ;  $\frac{R_{air}}{R_{gas}}$  [17, 24–36]. Where,  $R_{gas}(I_{gas})$  is the resistance (current) of the sensing film in the presence of the gas molecules,  $R_{air}(I_{air})$  is the resistance (current) of the sensing film in the presence of the air and  $S$  is the sensor response. The response time is the time taken by any gas sensor to attain 90% of the maximum sensor response when the gas is introduced to the sensor. The recovery time is the time taken by any gas sensor to reach 10% of the maximum sensor response when the gas is turned off. The capacity of a gas sensor to respond to a particular gas in the presence of other gases is called selectivity ability of the gas sensor. Usually, sensing films are sensitive to every gas present in the atmosphere at a same time. Also, some gases have nearly same sensor response for specific sensing film. It is therefore difficult to determine the exact change in the sensor response

generated by the target gas. Therefore, sensing film must be very selective for the target gas with highest sensor response.

Graphene as a 2D material has some unique properties such as the large surface area ( $2360 \text{ m}^2 \text{ g}^{-1}$ ), zero rest mass of charge carriers near Dirac points and high carrier mobility  $200,000 \text{ cm}^2 \text{ V}^{-1} \text{ s}^{-1}$  at room temperature (RT) [37–42]. Similarly, other 2D layered materials have numerous properties and applications in comparison to their bulk form [43–45]. The intriguing properties of 2D TMDCs are their high surface to volume ratio, absence of dangling bonds in the pristine form, strong spin–orbit coupling interaction and the high interaction ability for the gas molecules adsorption [46–52]. These features of 2D materials offer interest in exploring their new fundamental physics [32, 53]. The layer-dependent mechanical, electronic, and optical properties of 2D materials create curiosity to learn and explore their fundamental properties [54–56]. A one atom thick layer of graphene has shown an appealing role in gas sensing by detecting 1 ppb concentration of various gases such as  $\text{NH}_3$ ,  $\text{NO}_2$ ,  $\text{H}_2\text{O}$ , and  $\text{CO}$  [57]. Gas sensors based on graphene have been widely inspected and employed owing to its high carrier mobility, mechanical strengths greater than to steel, remarkable optical and electronic properties [58–60]. Despite having an impressive sensor response and response time, the  $\text{NO}_2$  sensors have suffered from long recovery time owing to the very high adsorption energy of gas molecules with graphene [61–63]. In terms of growth and production, the synthesis of graphene is very costly with the use of toxic chemicals at high temperatures [64–67]. Another challenge associated with graphene is the production of high quality and large surface area graphene film, which is very difficult to attain and the presence of any non-carbon elements disrupts the hexagonality of graphene [68]. Moreover, graphene has zero bandgap, and less environment stability which reduces the gas-sensing performance and long term stability of graphene-based sensors [47, 69].

These limitations of graphene mold the direction of research to discover new nonzero bandgap 2D materials like  $\text{MoS}_2$ ,  $\text{MoSe}_2$ ,  $\text{MoTe}_2$ ,  $\text{WS}_2$ ,  $\text{WSe}_2$ , BP, and many more [70–83]. The interaction between the gas molecules and sensing materials is the indelible part of any gas-sensing process. In 2D materials, especially  $\text{MoS}_2$ , is at the forefront in the race of an ideal gas-sensing material [84, 85]. The other substitutes of the 2D materials family are  $\text{WS}_2$ ,  $\text{WSe}_2$ ,  $\text{NbSe}_2$ ,  $\text{MoTe}_2$ , etc. [86–90]. However, most of the research on  $\text{NO}_2$  detection is carried out with  $\text{MoS}_2$ .  $\text{MoS}_2$ -based gas

sensors have achieved noticeable research interest in recent years.  $\text{MoS}_2$  has already shown emerging environmental applications in energy storage, light interaction, flexible electronic devices and in biofield due to its semiconducting nature [50, 91–96].  $\text{MoS}_2$  has two possible crystal phases, trigonal and hexagonal, where hexagonal is semiconducting while trigonal is having metallic nature [97]. The presence of weak Van der Waals force enables the easy isolation of layers from bulk  $\text{MoS}_2$ . The indirect bandgap of 1.2 eV in bulk  $\text{MoS}_2$  is converted to a direct bandgap of 1.8 eV for monolayer  $\text{MoS}_2$  [50, 98, 99]. The absence of dangling bonds provides stability to pristine  $\text{MoS}_2$  flakes in liquid and gaseous media in the presence of oxygen. These facilities make  $\text{MoS}_2$  compatible for gas-sensing application [100]. The low binding energy of 6.1 and 13.9 eV is needed to create S and Mo vacancies, respectively, which can turn the edges of  $\text{MoS}_2$  flakes into metallic sites [101, 102].  $\text{MoS}_2$  has a tunable bandgap compared to graphene which increases the overall sensing performance of  $\text{MoS}_2$  film [103]. The  $\text{MoS}_2$  flakes have strong photoluminescence (PL) absorption due to the presence of direct bandgap, helpful to design the optical gas sensors. The high on/off ratio ( $10^8$ ), the high carrier mobility of  $400 \text{ cm}^2 \text{ V}^{-1} \text{ s}^{-1}$  at RT, low effective electron mass of  $0.48 m_e$  are advantageous for developing fast gas sensors [54, 104–106]. Owing to these electronic properties, any minor change in the electron concentration of  $\text{MoS}_2$  flakes can be easily detected.  $\text{MoS}_2$  flakes have four Raman active modes ( $E_{1g}$ ,  $E_{2g}^1$ ,  $A_{1g}$ ,  $E_{2g}^2$ ). The  $E_{2g}^1$  mode is an in-plane mode and  $A_{1g}$  is an out of plane mode [107, 108]. Chakraborty et al. studied in situ Raman spectroscopy of single-layer  $\text{MoS}_2$  flakes [109]. It has been found that  $E_{2g}^1$  is not sensitive to electron doping while the  $A_{1g}$  mode is very sensitive to electron doping [109]. With higher electron concentration, the  $A_{1g}$  mode gets softened due to stronger electron–phonon coupling mode than  $E_{2g}^1$  mode [109]. These vibrational characteristics are ideal for the chemiresistance gas sensors where charge concentration has remained an important parameter. Furthermore,  $\text{MoS}_2$  film has impressive mechanical and optical properties with high Young's modulus up to 300 GPa, deformity up to 11% without any fracture and amazing transparent nature, making it a potential candidate for optical and flexible devices [110–114]. Moreover,  $\text{MoS}_2$  flakes can be bent up to the radius of 0.75 mm, without deteriorating its electronic properties [115]. Excellent gas molecules detection ability,



enormous active sites, large surface to volume ratio and presence of favorable adsorption sites have endorsed MoS<sub>2</sub> as the unique sensing material. The development and key accomplishment of MoS<sub>2</sub>-based NO<sub>2</sub> gas sensors in last 8 years are summarized in Fig. 1. With the discovery of the

graphene by mechanical exfoliation (ME) technique by the Geim and Novoselov, they further revealed in 2005 that the ME technique can also be employed to thin down the other bulk materials such as MoS<sub>2</sub> [43]. Following the uniqueness of the MoS<sub>2</sub>, Li et al. developed the NO<sub>x</sub> sensitive gas sensor

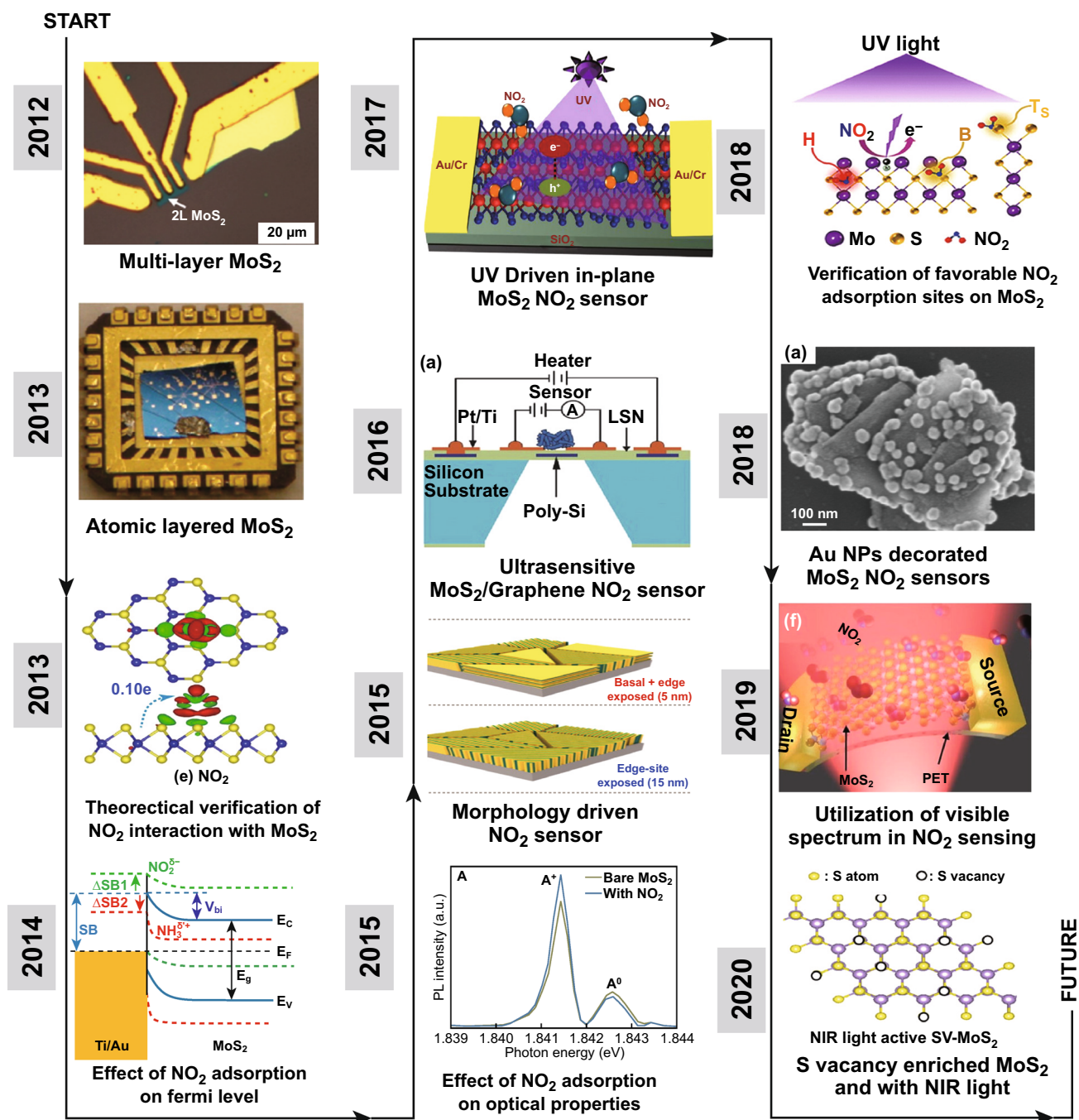


**Fig. 1** Schematic representation of the 8-year journey of MoS<sub>2</sub>-based NO<sub>2</sub> sensors. Reproduced with permission from Refs. [34, 118]. Copyright @ Wiley-VCH; Refs. [17, 32, 35, 36, 119, 120, 123]. Copyright @ American Chemical Society; Ref. [117]. Copyright @ Springer; Ref. [121]. Copyright @ AIP Publishing; Ref. [122]. Copyright @ Elsevier



[34]. In a similar year, He et al. developed the NO<sub>2</sub> sensor based on multilayer MoS<sub>2</sub> flakes and confirm the role of MoS<sub>2</sub> in NO<sub>2</sub> detection [42]. The fundamental research to study the electronic properties of MoS<sub>2</sub> was boosted after the fabrication of first MoS<sub>2</sub> transistor by Kis et al. [116]. In 2013, Late et al. studied the role of negative and positive back gate voltage on NO<sub>2</sub> sensing by fabricating the MoS<sub>2</sub> field effect transistor (FET) [17]. The year 2014–2015 was devoted to the charge transfer mechanism due to the gas molecules exposure. Yue et al. investigated theoretically and confirmed that gas molecule detection in MoS<sub>2</sub> is attributed to the charge transfer process [117]. Liu et al. demonstrated that NO<sub>2</sub> gas adsorption strongly affects the Schottky barrier height (SBH) [36]. Cho et al. performed the in-situ PL spectroscopy and investigated the p-type doping in MoS<sub>2</sub> flakes due to NO<sub>2</sub> exposure [32].

Till 2015, MoS<sub>2</sub> has been established itself as the potential candidate for the gas sensing with a well-defined gas-sensing mechanism. However, MoS<sub>2</sub>-based NO<sub>2</sub> sensors suffered from the incomplete recovery due to the high adsorption of NO<sub>2</sub> on MoS<sub>2</sub>. Cho et al. studied the role of active sites in gas sensing [35]. NO<sub>2</sub> adsorption is very high at the active sites in MoS<sub>2</sub>. The active sites are highest at the edges due to presence of dangling bonds, defects and vacancies, while the terrace of MoS<sub>2</sub> is inert due to absence of dangling bonds. Authors synthesized MoS<sub>2</sub> flakes of three different orientations: in-plane MoS<sub>2</sub>, mixed MoS<sub>2</sub> and vertical aligned MoS<sub>2</sub> flakes. The number of active sites and NO<sub>2</sub> sensing performance were highest in the case of vertical MoS<sub>2</sub> flakes. Several studies have been published in parallel years for the fabrication of hybrid MoS<sub>2</sub> heterostructures to improve the charge transfer in MoS<sub>2</sub>. Long et al. fabricated the low temperature MoS<sub>2</sub>/graphene hybrid structure and develop ultrasensitive NO<sub>2</sub> sensors up to 50 ppb [118]. Although researchers have achieved full recovery at high temperatures, but the production of RT-recoverable gas sensors has remained a challenging task.

Since 2017, light-assisted NO<sub>2</sub> sensors have attracted the worldwide scientific community. Rahul et al. in 2017, investigated the role of ultraviolet (UV) light in basal plane MoS<sub>2</sub> flakes and achieved the full recovery at RT under UV light illumination. Agrawal et al. demonstrated the role of favorable NO<sub>2</sub> adsorption sites in MoS<sub>2</sub> by synthesizing the unique morphology of MoS<sub>2</sub> flakes [119, 120]. Metal NP doping has theoretically proven to be a great combination for enhanced gas sensor response, reactivity and recovery

in the past years. Zhou et al. developed the MoS<sub>2</sub> sensor decorated with Au NPs [121]. It is important to remember that, until 2018, most of the published report used only UV light to boost the efficiency of the sensing light. In the next years, 2019 and 2020 (running) researchers fabricated the visible spectra and near infrared (NIR) spectra-driven NO<sub>2</sub> sensors [122, 123].

Thus we may conclude that gas-sensing characteristics of MoS<sub>2</sub> film-based device are highly dependent on size, shape, thickness, morphology, growth direction, polytype composition, defects, metal functionality and the hybrid structure of MoS<sub>2</sub> films. These factors can be used to classify MoS<sub>2</sub>-based NO<sub>2</sub> sensors [25, 42, 124].

Apart from the experimental efforts, theoretical studies have also played a noticeable role in designing the experiments and predicting the gas-sensing potential of the proposed materials [125]. Theoretical methods such as density functional theory (DFT) always prove their advantage in terms of time, efforts and cost [125]. DFT provides a broad and detailed view to understand the fundamental mechanism happening between the gas molecules and the sensing material [126, 127]. The key features of DFT are the pre-calculation of the charge transfer and understanding of fundamental interaction between the sensing material and gas molecules. These features are helpful to understand the physical and chemical adsorption of gas molecules, theoretical estimation of defects, their effects on electronic and optical properties and functionalizing the defects with other materials and noble metals. Very few reviews are focused on both the theoretical contribution and the experimental contribution of MoS<sub>2</sub> for NO<sub>2</sub> sensing.

The goal of this review is to discuss in detail the MoS<sub>2</sub>-based NO<sub>2</sub> gas sensors and to provide in-depth insights into previously established theoretical and experimental approaches. We focused on the various properties of MoS<sub>2</sub> which played a vital role in gas sensing. Mainly, the role of 1T and 2H MoS<sub>2</sub> phases, large surface area available in MoS<sub>2</sub> film for gas molecule adsorption, faster charge transport in MoS<sub>2</sub>, effect of modulating favourable adsorption sites via morphology, optical properties and defects available in MoS<sub>2</sub> will be discussed.

Considering all these points, we have categorized various strategies for enhancing the performances of MoS<sub>2</sub> sensors as follows: role of device structure (resistor and transistor), monolayer MoS<sub>2</sub>, multilayer MoS<sub>2</sub>, defect tailoring, morphology engineering, heterostructures, functionalizing

with noble metals and light-assisted  $\text{NO}_2$  sensors. We have focused our present review in the direction as mentioned above and a schematic view is shown in Fig. 2.

We also focus a little bit on the traditional  $\text{NO}_2$  sensing materials such as metal oxides and carbon-based nanomaterials to gain a clear difference between  $\text{NO}_2$  sensing performance of traditional materials and  $\text{MoS}_2$ .

A tremendous effort has been employed to develop fast, high sensor response, selective and low-cost  $\text{NO}_2$  electrical sensors. Various nanomaterial-based sensors from zero dimension (0D, quantum dots) [128–135] to two dimensions (2D, metal oxides, TMDCs) [27, 81, 83, 136–138] showed their exceptional detection ability to detect parts per billion (ppb)  $\text{NO}_2$  gas traces [139–143]. Every nanomaterials has its own merits and demerits in the  $\text{NO}_2$  gas detection. The traditional metal oxides (ZnO,  $\text{SnO}_2$ ,  $\text{TiO}_2$ ,  $\text{In}_2\text{O}_3$ ,  $\text{WO}_3$  etc.) based  $\text{NO}_2$  sensors showed a fast response and high sensor response. However, the highly sensitive nature of metal oxides to humidity reduces the sensor response and stability of gas sensors. Moreover, for accelerating the interaction between the gas molecules and metal oxides, metal oxides gas sensors are need to operate at a higher temperature (250–500 °C). High temperature results in the agglomeration of nanomaterials and increase the grain size of the metal oxide film [28, 143–155]. On the contrary, the carbon material-based  $\text{NO}_2$  sensors provide the high sensor response but at RT the desorption rate of gas molecules is too slow. Thus, the CNT-based  $\text{NO}_2$  sensors are suffered from long

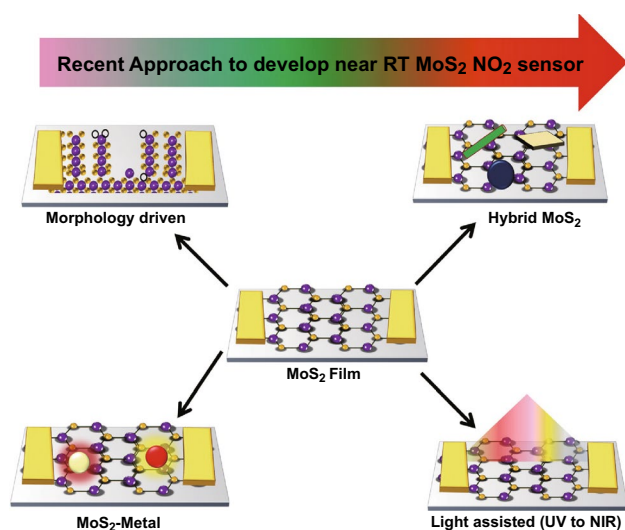


**Fig. 2** Schematic representation of strategies adopted to develop a high-performance  $\text{NO}_2$  gas sensor based on  $\text{MoS}_2$  flakes

recovery time [30, 156–158]. In summary, metal oxide and carbon-based  $\text{NO}_2$  sensors are suffered from thermal safety due to high temperature, structure complexity and complex device fabrication, which restricts the use of metal oxides in smart, wearable and next-generation device for the internet of things (IoT).

The problems associated with metal oxide and carbon-based  $\text{NO}_2$  sensor have demanded the development of new noble materials with advanced gassensing properties. In Fig. 3, we have summarized the  $\text{NO}_2$  detection performance of various reported traditional materials-based sensors such as ZnO,  $\text{SnO}_2$ , CNTs,  $\text{TiO}_2$ ,  $\text{In}_2\text{O}_3$ ,  $\text{SnS}_2$ , and  $\text{WO}_3$ , in terms of operating temperature, sensor response and recovery time [26, 91, 154, 159–197]. Most of the traditional nanomaterial-based  $\text{NO}_2$  sensors reported good sensor response at high operating temperatures (purple star) and simultaneously, they also suffered from the high recovery time (green circles). However, for an ideal gas sensor, it should be operated near RT for high sensing performances. The ideal sensor should have a high sensor response, lower response, and recovery time near to RT, as shown in star region of Fig. 3. Therefore, there is a great demand to develop a low temperature, highly sensitive and fast  $\text{NO}_2$  sensors.

The roadmap of the review is as follows. In Sect. 1, we introduced  $\text{MoS}_2$  as the  $\text{NO}_2$  sensors and addressed its benefits over the traditional metal oxide sensors. In Sect. 2, we will present some peculiar properties of  $\text{MoS}_2$ , which played a critical role in gas molecule adsorption. Section 3 is focused on the interaction mechanism of  $\text{NO}_2$  with  $\text{MoS}_2$  and effect of  $\text{NO}_2$  on electronic, optical and surface

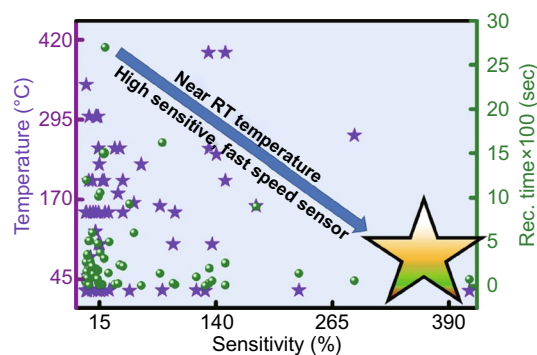


**Fig. 3** Traditional material-based  $\text{NO}_2$  gas sensors. Most of the traditional  $\text{NO}_2$  sensors have a high operating temperature requirement. The colored star area shows the ideal states for a gas sensor. Data has been taken from Refs. [26, 91, 154, 160–209]

properties. In Sect. 4, we will discuss several theoretical findings in which, interaction between  $\text{NO}_2$  and  $\text{MoS}_2$  is discussed. Section 5 covers the experimental reports where bare  $\text{MoS}_2$ , morphology-driven  $\text{MoS}_2$ , metal-doped  $\text{MoS}_2$ , vacancy-driven and photon-assisted  $\text{MoS}_2$ -based  $\text{NO}_2$  sensors will be discussed briefly. In Sect. 6, we are going to present some findings where  $\text{MoS}_2$ -based heterostructures are utilized for  $\text{NO}_2$  sensing. Finally, in Sect. 7, we will conclude our review and discussed the future of  $\text{MoS}_2$ -based  $\text{NO}_2$  sensor.

## 2 $\text{MoS}_2$ : A Unique Material for Gas Sensing

### 2.1 Structure of $\text{MoS}_2$

The single layer of  $\text{MoS}_2$  has two polymorphs: trigonal prismatic (2H- $\text{MoS}_2$  Phase) and octahedral phase (1T- $\text{MoS}_2$  Phase), belonging to  $D_{3h}$  and  $D_{3d}$  point groups, respectively. Both polytype structures are shown in Fig. 4a, c [210]. Here, H and T depict hexagonal and trigonal symmetry, respectively, while digits equate to layers repeat per unit cells. In general, the 2H phase is obtained by synthesizing  $\text{MoS}_2$  film using methods such as mechanical exfoliation (ME), chemical vapor deposition (CVD) or ultrasonication [108, 211]. The 1T phase is preferred by the Li intercalation method. The 2H and 1T phases has been widely studied experimentally and theoretically. The 2H- $\text{MoS}_2$  phase is semiconducting, while the 1T- $\text{MoS}_2$  phase exhibits metallic nature. The varied electronic nature of  $\text{MoS}_2$  can be understood using crystal field theory (CFT). In CFT, five d orbital  $d_{x^2-y^2}$ ,  $d_{z^2}$ ,  $d_{xy}$ ,  $d_{yz}$  and  $d_{zx}$  of transition metal (Mo) are non-degenerate. These d-bands are located between the bonding ( $\sigma$ ) and antibonding bands ( $\sigma^*$ ), shown in Fig. 4b, d. In trigonal prismatic ( $D_{3h}$ ), the orbitals splits into three levels,  $d_{z^2}$  ( $a_1$ ),  $d_{x^2-y^2} + d_{xy}$  ( $e$ ) and  $d_{yz} + d_{zx}$  ( $e'$ ). The octahedral group divided into levels  $e_g$  having  $d_{z^2}$  and  $d_{x^2-y^2}$  orbital and in  $t_{2g}$  having  $d_{xy}$ ,  $d_{yz}$  and  $d_{zx}$  [212]. When the highest orbitals are partially filled the  $\text{MoS}_2$  possess the metallic like conductivity (1T- $\text{MoS}_2$ , Fig. 4d) and if the highest orbitals are fully filled,  $\text{MoS}_2$  behave like semiconductor (2H- $\text{MoS}_2$ , Fig. 4b). In recent years, a lot of research work has been done on 2H- $\text{MoS}_2$  phases in gas-sensing applications and many of them addressed in the next sections [17, 34, 35, 42, 120, 213, 214]. The 1T- $\text{MoS}_2$  has higher active sites and electronic conductivity reaches up to sixfold higher

than the 2H- $\text{MoS}_2$  [99]. Mark et al. prepared a stable metallic phase of  $\text{MoS}_2$  and they observed an enhanced catalytic performance in 1T phase [215]. In addition, the metallic  $\text{MoS}_2$  showed enhanced photoluminescence due to higher sulfur vacancies [99]. Furthermore, Kappera et al. studied the device performance of both phases and observed the low contact resistance at zero bias gate voltage. The low contact resistance generates high drive current with high mobility of  $50 \text{ cm}^2 \text{ V}^{-1} \text{ s}^{-1}$  [216, 217]. These all properties showed that 1T- $\text{MoS}_2$  is an important phase for  $\text{NO}_2$  gas sensing. Thus, consideration of the role of both phases in  $\text{NO}_2$  sensing is equally important.

### 2.2 Large Surface Area for Gas Molecule Adsorption

In contrast to metal oxides, the  $\text{MoS}_2$  has a large specific surface area. The large surface area provides maximum adsorption sites for the adsorption of gas molecules and enhances the surface perturbation in the presence of gas molecules. Moreover, in chemiresistance gas sensors, sensor response is directly proportional to the change in the resistance arises due to the adsorption of gas molecules on the surface [42, 218]. Tongay et al. proposed that if one  $\text{O}_2$  molecule gets physisorbed on the unit cell of  $\text{MoS}_2$ , it withdraws  $0.04e$  per unit cell and the sheet charge density reduced up to  $5 \times 10^{13} \text{ cm}^{-2}$  [219]. Therefore,  $\text{MoS}_2$  is very sensitive and amenable to be used in gas-sensing devices. In this context,  $\text{MoS}_2$  established himself as the promising chemical sensing material due to large highly sensitive surface. CVD, ME, and hydrothermal methods are the most popular methods for synthesizing  $\text{MoS}_2$  for the gas-sensing devices. Among them, the most effective and occupied method to grow large size wafer-scale  $\text{MoS}_2$  flakes is the CVD. We have prepared a comparative graph of flakes sizes with the two most prominent methods i.e., ME and CVD. It has been observed that individual flakes size grown by the ME method can go maximum up to  $10 \mu\text{m}$ . However, with CVD,  $\text{MoS}_2$  flakes of larger size can be grown in comparison with ME. It is worth to mention, we collected data of domain size of only individual  $\text{MoS}_2$  single-layer flakes generated by ME and CVD methods for the data in Fig. 4e. CVD can grow highly uniform, high density, large area and control on morphology of the film while the ME can synthesize highly pure  $\text{MoS}_2$  flakes, which is desirable for many electrical and optical applications. Agrawal et al. synthesized uniform

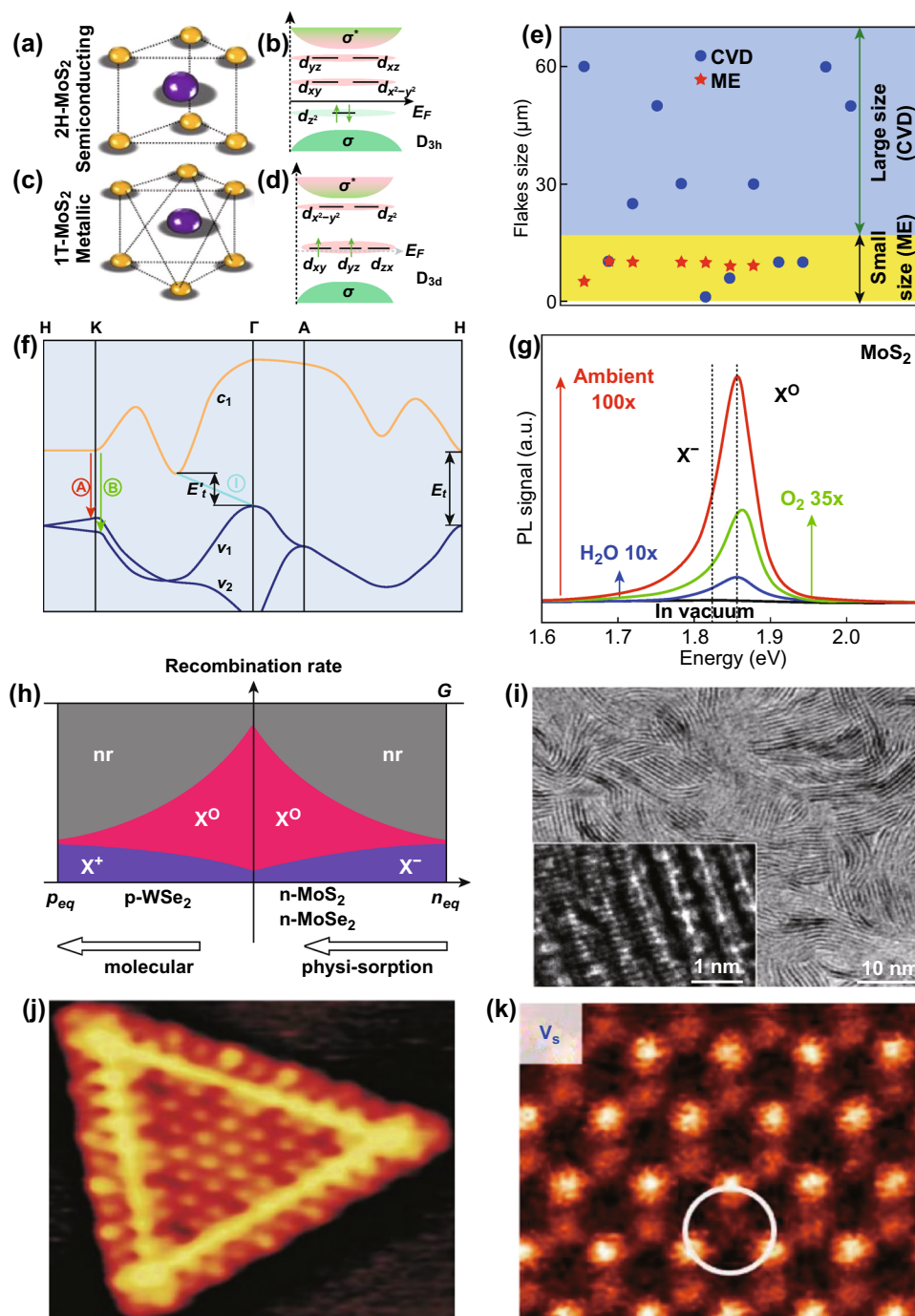


**Fig. 4** **a** Schematic structure of 2H-MoS<sub>2</sub>. **b** *d*-orbital filling of the semiconducting 2H-MoS<sub>2</sub>. **c** Schematic structure of 1T-MoS<sub>2</sub>. **d** *d*-orbital filling of the semiconducting 1T-MoS<sub>2</sub>. **e** The reported domain size of individual monolayer MoS<sub>2</sub> flakes from the ME and CVD technique. CVD provides a larger flake size compared to the ME technique. The data of MoS<sub>2</sub> flakes size has been taken from Refs. [50, 107, 220, 222–239]. **f** Band structure of MoS<sub>2</sub>. The ‘A’ and ‘B’ PL peaks are corresponding to the direct bandgap ( $E_g$ ) transition of MoS<sub>2</sub>. Reproduced with permission from Ref. [50]. Copyright (2010) American Physical Society. **g** Spectral change in PL due to exposure of O<sub>2</sub> alone, H<sub>2</sub>O alone and with both. O<sub>2</sub> and H<sub>2</sub>O incorporate p-type doping which contribute to a blue shift in the peaks. **h** Rate of recombination with neutral exciton and charge trion as a function of charge density in n-type MoS<sub>2</sub> and p-type MoSe<sub>2</sub>. Reproduced with permission from Ref. [219]. Copyright (2013) American Chemical Society. **i** TEM image of the as grown vertical aligned MoS<sub>2</sub> flakes. The edges have high catalytic activity than the basal plane and enhance the reactivity of the gas molecules. Reproduced with permission from Ref. [240]. Copyright (2013) American Chemical Society. **j** STM image of the triangular MoS<sub>2</sub> flakes where yellow perimeters were showing the presence of the metallic states at the edges. Reproduced with permission from Ref. [241]. Copyright (2001) American Physical Society. **k** ADF images of monovacancy S intrinsic defects. Reproduced with permission from Ref. [242]. Copyright (2013) American Chemical Society



vertical MoS<sub>2</sub> flakes of 1 × 2 cm<sup>2</sup> size on SiO<sub>2</sub>/Si substrate. Furthermore, Lin et al. synthesized large size MoS<sub>2</sub> flakes of 308 μm [220]. Zhan et al. synthesized the centimeter size MoS<sub>2</sub> layer by CVD method [221]. The nucleation rate, supply of precursors, S and MoO<sub>3</sub> powder, temperature and the carrier gas flow rate, by CVD is mainly responsible for large area MoS<sub>2</sub> growth [221, 222]. CVD provides great control on the nucleation rate and mass transport. MoS<sub>2</sub> flakes size is increased with time as the more and more nucleation center and sites grow over substrate. Hence, CVD is the better option to grow the large area MoS<sub>2</sub> flakes and to fabricate the gas-sensing devices.

### 2.3 Impact of Gas Adsorption on Optical Properties of MoS<sub>2</sub>

The photoluminescence (PL) is an essential characterizations to detect changed in the electron concentration of a 2D material-based gas sensor. Gas-sensing ability of 2D materials is governed by either electron depletion or accumulation that depend on the doping behavior of the exposed gas molecules.

The nature of dopants critically affect the PL spectra of MoS<sub>2</sub>. MoS<sub>2</sub> has two well-reported PL peaks 'A' and 'B'. These PL peaks are emerged due to the splitting of the valence band in  $\nu_1$  and  $\nu_2$  [50]. The valence band splitting at the K-point is the collective effect of interlayer spacing and spin-orbit coupling. Figure 4f displays the direct bandgap transition peaks (A and B) and indirect bandgap transition (I) in the MoS<sub>2</sub> crystal structure. The spectral weight of exciton and trions can be significantly tuned by the electrical gating, n-type or p-type molecular adsorption (e.g. H<sub>2</sub>O, TCNQ) doping, and defects present at the cracks [219, 243–245].

Nan et al. studied the role of molecular adsorption on the PL through oxygen exposure [246]. Micro PL analysis revealed the enhancement in PL intensity due to molecules adsorption by MoS<sub>2</sub> surface at moderate temperatures in high vacuum ambient. The PL spectroscopy was performed over the as prepared monolayer MoS<sub>2</sub> films, which were annealed for 1 h in vacuum at 350 and 500 °C. It was observed that the PL intensity was increased sixfold after annealing at 350 °C with the blue shift in energy (from 1.79 to 1.81 eV). Moreover, the PL intensity in sample annealed at 500 °C was erratic at different locations. When the MoS<sub>2</sub> film was annealed at 350 °C, the MoS<sub>2</sub> film was uniform and

environmental O<sub>2</sub> and H<sub>2</sub>O physically got adsorbed by MoS<sub>2</sub> flakes. Both O<sub>2</sub> and H<sub>2</sub>O introduced p-type doping in MoS<sub>2</sub>. When the flakes annealed at 500 °C, cracks were formed in the film with the generation of defects. At these defects' sites O<sub>2</sub> and H<sub>2</sub>O adsorbed chemically and introduced heavy p doping. DFT calculations were also performed and calculated charge transfer between the O<sub>2</sub> and pristine MoS<sub>2</sub> was 0.021e, while at the defects site, the charge transfer was 0.997e. Thus, higher charge transfers at the defective sites introduced heavy p-type doping. Tongay et al. also studied the modulation in the PL due to the physisorption of O<sub>2</sub> and H<sub>2</sub>O molecules. Physisorbed O<sub>2</sub> and H<sub>2</sub>O molecules bonded weakly with MoS<sub>2</sub> but introduced significant p doping. The variation in PL intensity due to exposure of O<sub>2</sub> alone (green), H<sub>2</sub>O alone (blue) and with both (red) shown in Fig. 4g [247]. The 0.04e and 0.01e times charges were transferred from MoS<sub>2</sub> to O<sub>2</sub> and H<sub>2</sub>O molecules, respectively. The O<sub>2</sub> and H<sub>2</sub>O molecules adsorption modulate the charge concentration in the MoS<sub>2</sub>. The electrons of the n-type MoS<sub>2</sub> flakes are depleted by both molecules. Here, the focus has been given on the low energy exciton peak which is the combination of the neutral exciton ( $X^0$ ) and charge trions ( $X^+/X^-$ ). In actual, the MoS<sub>2</sub> layer has high sheet charge density ( $n_{eq}$ ). The high  $n_{eq}$ , destabilizes the neutral exciton  $X^0$  due to electrostatic screening between the holes and free electrons while the  $X^-$  stabilizes due to high recombination rate of  $X^-$  trions [248]. Hence, with high  $n_{eq}$ , the overall PL intensity becomes low. With physisorption and chemisorption of molecules such as O<sub>2</sub> and H<sub>2</sub>O, the  $n_{eq}$  gets reduced. Hence, the number of electrons available in MoS<sub>2</sub> for trions formation is decreased. Thus, the intensity of  $X^-$  decreased and  $X^0$  enhanced with more stabilization, as can be seen from Fig. 4g, h. Moreover, it has been reported that the electronic gating and molecular doping can dramatically tune the PL [219, 244, 245, 249]. As the gas molecule adsorption introduces n or p doping, the study of PL with adsorption of molecules to MoS<sub>2</sub> is an important aspect to understand the nature of the gas molecules.

### 2.4 High Catalytic Nature and Presence of Metallic States

Another essential feature of MoS<sub>2</sub> is the presence of a large number of active sites for promoting the chemical reactions. Jaramillo et al. identified the active sites on the MoS<sub>2</sub> through

scanning tunneling microscopy (STM) [250]. The MoS<sub>2</sub> samples were synthesized on the Au substrate and STM imaging was performed in the ultra-high vacuum. The STM measurements confirmed that flat MoS<sub>2</sub> edges have bright rims which appeared as bright lines along the flakes perimeter. To validate the high activity of the edges, the hydrogen evolution reactions (HER) activity was investigated which also confirmed the high reactivity of edges. Kong et al. synthesized MoS<sub>2</sub> by the sulfurization of Mo film deposited by e-beam lithography. The tunneling electron microscopy (TEM) image of vertical aligned MoS<sub>2</sub> flakes is shown in Fig. 4i and in inset. It is evident from these studies that edges have highly active site. Thermodynamically, the growth of in-plane MoS<sub>2</sub> is highly probable than the edge oriented MoS<sub>2</sub> flakes. The high activity of the edges boosts the motivation to grow edge-enriched film by forming the various morphology of MoS<sub>2</sub> nanoflakes such as vertical aligned MoS<sub>2</sub>, MoS<sub>2</sub> nanowires, MoS<sub>2</sub> spheres etc. Kim et al. fabricated 2D SnS<sub>2</sub> and develop NO<sub>2</sub> sensor by enhancing the active sites [251]. The vertically aligned SnS<sub>2</sub> showed high NO<sub>2</sub> reactivity due to the presence of a large number of active sites in comparison to the basal plane SnS<sub>2</sub>. Shim et al. synthesized SiO<sub>2</sub> nanorods (NRs) and decorated them with MoS<sub>2</sub> flakes [252]. These SiO<sub>2</sub> NRs enhanced the catalytic activity of MoS<sub>2</sub> flakes by exposing more edges of MoS<sub>2</sub> flakes [251]. Hence, the NO<sub>2</sub> detection ability of SiO<sub>2</sub> NRs encapsulated with MoS<sub>2</sub> is increased. The MoS<sub>2</sub> surface has maximum number of active sites which enhance the chemical activity of MoS<sub>2</sub> film [240, 253, 254]. Another important feature of MoS<sub>2</sub> flakes is the presence of metallic states at the edges [241]. The MoS<sub>2</sub> edges behaved as the one-dimensional metallic wires and appeared as the bright brim of high conductance, as shown in Fig. 4j. The attention here is given to Mo edges having S dimers. The Mo edges have two metallic wave functions and generate metallic states in MoS<sub>2</sub>. Therefore, the presence of metallic edges will be helpful in the fast transfer of generated electron and holes. The generated charge can be rapidly transferred along the edges in edge-enriched MoS<sub>2</sub> and will be helpful in developing the fast responsive and recoverable gas sensors [255].

## 2.5 Impact of Gas Molecules Adsorption on Schottky Barrier Height

The gas-sensing performance of 2D materials based on chemiresistance gas sensors is critically influenced by the

metal contacts [256–259]. In 2D materials, the gas molecule adsorption affects the charge concentrations and carrier density. Depending on the nature of the gas molecules, the charge carrier density either increases or reduces and Fermi level of 2D materials is modulated with gas molecule adsorption. The equilibrium Fermi level of metal and semiconductor before and after exposure to the gas molecule will be different due to variation in the charge carrier density in the sensing film. In chemiresistance sensors, the Schottky barrier height between the metal contact and the 2D material surface can alter the surface charge transfer mechanism. Various studies have been reported to understand the role of Schottky barrier height (SBH) and Schottky barrier modulation (SBM) with gas molecule exposure in traditional gas sensors as well as in 2D material-based gas sensors [260, 261]. The band structure of metal and semiconductor can be divided into two regions: (1) alignment of the energy levels of the metal and semiconductor for charge carrier injection and (2) band bending at the space charge region for charge carrier separation [262]. If the metal and semiconductor work functions are  $\phi_M$  and  $\phi_S$  respectively, the SBH determined by the Mott–Schottky rule is given by Eq. (1):

$$\phi_b = \phi_M - \chi_S \quad (1)$$

Depending on the type of the semiconductor (n-type or p-type), the Schottky or ohmic contact nature of the junction is decided. In 2D materials, ohmic contacts are of great importance due to their low resistance and high charge transfer in terms of high mobility and current on/off ratio [104, 263, 264]. However, the ohmic contacts are not beneficial for gas-sensing point of view. The reason for this is the interaction of gas molecules with sensing film and their effect on the Schottky barrier modulation (SBM) [36, 72]. The importance of the Schottky contact is well established in the metal oxide sensors. Zhou et al. demonstrated the remarkable performance of the ZnO sensors by utilizing the Schottky contact in comparison to the ohmic contact [265]. Similarly, Wei et al. fabricated the ZnO NW-based CO sensor in such a way that one end behaved as the Schottky contact, while the other end behaved as the ohmic contact [266]. Schottky end behaves like a gate terminal and the Schottky barrier height (SBH) was tuned. Nearly 4 times enhanced sensor response with seven times reduce response and recovery time were observed. In all these reports, SBM provides an efficient and enhanced charge transport. Hence, gas-sensing performance is high in the Schottky contacted devices.

## 2.6 Role of Defects in Gas Molecule Adsorption

In case of MoS<sub>2</sub>, defects can be generated during the synthesis or transfer of MoS<sub>2</sub> due to synthesis imperfections [267–270]. In addition, these defects are susceptible to ambient environments conditions [271, 272]. Defects can also be created through the irradiations, metal doping and functionalization [273, 274]. Thus, MoS<sub>2</sub> structures unavoidably have various defects in terms of vacancies, dopants, adsorbates, adatoms, and impurities. On the contrary, the pristine MoS<sub>2</sub> is assumed to have defect free surfaces. However, the synthesis of defect free MoS<sub>2</sub> flakes is quite difficult and convoluted. Defects are easily produced during the synthesis process. Defects crucially affect various mechanical, electronic, optical and catalytic properties. Zhou et al. fabricated MoS<sub>2</sub> and studied the possible structural defects [242]. The authors studied atomic-resolution annular dark field (ADF) images of CVD-grown MoS<sub>2</sub> flakes. The defects were classified into six types (i) mono-sulfur Vacancies (V<sub>S</sub>), (ii) di-sulfur vacancies (V<sub>S2</sub>), (iii) Mo atom with three nearby sulfur (V<sub>MoS3</sub>), (iv) Mo atom with three di sulfur pairs (V<sub>MoS6</sub>), (v–vi) Antisite defects, Mo atom at S vacancy site (Mo<sub>S2</sub>) and S atom at Mo vacancy site (S<sub>2Mo</sub>). The formation energy of these vacancies is studied in term of S chemical potential. The formation energy plot revealed that mono S vacancies are most probable and need lowest formation energies. The ADF image of S vacancy site is shown in Fig. 4k. These defects could play a crucial role in the gas molecule adsorption. The benefits of defects in graphene have already received great attention [275, 276]. The findings of the reports revealed that the sensing mechanism in pristine and defective graphene is completely different. The defective graphene has higher interaction with gas molecules due to the presence of the defects. Interestingly in MoS<sub>2</sub>, defects can greatly influence the gas-sensing properties [86, 277]. Moreover, doping defects with substitutional impurities atoms can greatly improve the MoS<sub>2</sub> sensing performances. The effect of dopant and impurities is also well established in graphene. Zhang et al. studied the sensing performance of graphene-doped B, N, Si, Ca, Co and Fe, defective graphene and on pristine graphene [278]. The defective graphene doped with Ca, Co and Fe showed the highest interaction with H<sub>2</sub>S molecules. In metal-doped graphene, mixing of the graphene orbitals and metals orbitals is enhanced with H<sub>2</sub>S orbitals which leads to the strong interaction.

## 3 Charge Transfer Mechanism Between NO<sub>2</sub> and MoS<sub>2</sub>: Effect on Electronic Properties, Optical Properties, and Metal Contacts/MoS<sub>2</sub> Interface

In the present section, the nature and effect of NO<sub>2</sub> gas molecules on electrical conductivity, PL and MoS<sub>2</sub> band alignment will be addressed. NO<sub>2</sub> is a secondary product generated from the primary NO source as shown by Eq. (2) [279].

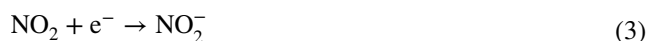


NO<sub>2</sub> has the electron acceptor nature and behaves as a strong oxidizing agent due to the unpaired electrons of nitrogen atom. NO<sub>2</sub> molecules take the electrons from the sensing materials. Generally, a chemiresistance gas sensor has a sensing layer that detects the presence of interacting gas molecules. The electrical and optical properties changes depending on the nature of interacting gas molecules and the type of semiconducting film. The gas molecules that interact can either behave like a reduction gas (electron donor) or an oxidizing gas (electron acceptor). Similarly, the semiconductor film may also have an n-type or a p-type nature.

In the case of TMDCs materials, gas molecules interaction depends on the nature of TMDC film and gas molecules. The interaction of gas molecules with TMDC film is governed via the physisorption or chemisorption process. The physisorption process occurs with pristine TMDC film while the chemisorption process happens with defective TMDC layers and on the defect sites.

In the case of pristine TMDC films, the gas molecules and TMDC films interact through the physisorption process. The gas molecules have weak adsorption energy and long adsorption distance with pristine TMDC film. Moreover, there is a less charge transfer between the gas molecules and TMDC film with an almost unchanged electronic structure. Hence, gas sensors based on pristine TMDC films have fast recovery but with low sensor response. The physisorption-based gas sensing reported in SnS<sub>2</sub> [175]. The SnS<sub>2</sub> showed a highly selective nature for NO<sub>2</sub> molecules due to the physisorption process. Furthermore, the positive binding energy of O<sub>2</sub> molecules with the SnS<sub>2</sub> surface indicated high surface resistance for oxygen molecules and supported that NO<sub>2</sub> sensing response in SnS<sub>2</sub> was through the physisorption process [175].

In the case of the chemisorption process, defects induce during the synthesis of MoS<sub>2</sub>. The gas molecules interact chemically with MoS<sub>2</sub>. The chemical interactions of gas molecules enhance gas-sensing performances of sensing material. The adsorption distance between the gas molecules and the adsorption sites is minimal in case of the chemisorption process. Hence, high charge transfer, strong adsorption energy, and significant change in the electronic states have been observed. The charge transfer schematic of NO<sub>2</sub> with the MoS<sub>2</sub> film (n-type or p-type) is shown in Fig. 5a and Eq. (3).



Cho et al. experimentally verified the charge transfer mechanism between the MoS<sub>2</sub> and NO<sub>2</sub> gas molecules using PL spectroscopy [32]. The authors synthesized n-type MoS<sub>2</sub> film by the chemical vapor deposition technique. The authors exposed NO<sub>2</sub> gas to MoS<sub>2</sub> film and investigated the charge transfer mechanism using photoluminescence (PL) spectroscopy. The authors observed that with NO<sub>2</sub> exposure,

the resistance of the n-type MoS<sub>2</sub> film increased (positive sensor response). The increment in the resistance confirmed that NO<sub>2</sub> withdraws the electrons from the n-type MoS<sub>2</sub> film. NO<sub>2</sub> gas molecules exposure modulates the electron concentration in MoS<sub>2</sub>. The change in the electron concentrations dramatically affects the PL. The MoS<sub>2</sub> has two main PL exciton peaks named 'A' and 'B' [50]. The intensities of these two PL peaks can either decreased or increased with a change in the electron concentrations [243, 244]. The low energy PL peak 'A' can be expanded into a charged trions (A<sup>+/-</sup>) and in neutral exciton (A<sup>0</sup>). The MoS<sub>2</sub> flakes grown on the SiO<sub>2</sub> substrate showed dominated behavior of A<sup>+</sup> peak over A<sup>0</sup>. Hence, the authors considered the positively charge trion peak (A<sup>+</sup>) and neutral exciton peak (A<sup>0</sup>). As NO<sub>2</sub> has an electron acceptor nature, it takes the electron from the MoS<sub>2</sub> and intensity of the (A<sup>+</sup>) enhanced due to conversion of neutral exciton in (A<sup>+</sup>). Actually, the numerous number of holes generated in MoS<sub>2</sub> due to depletion of electrons by NO<sub>2</sub>. Therefore, intensity of A<sup>+</sup> trions enhanced and neutral exciton suppressed. Similar behavior is observed in the PL spectroscopy, shown in Fig. 5b. The effect of NO<sub>2</sub> exposure

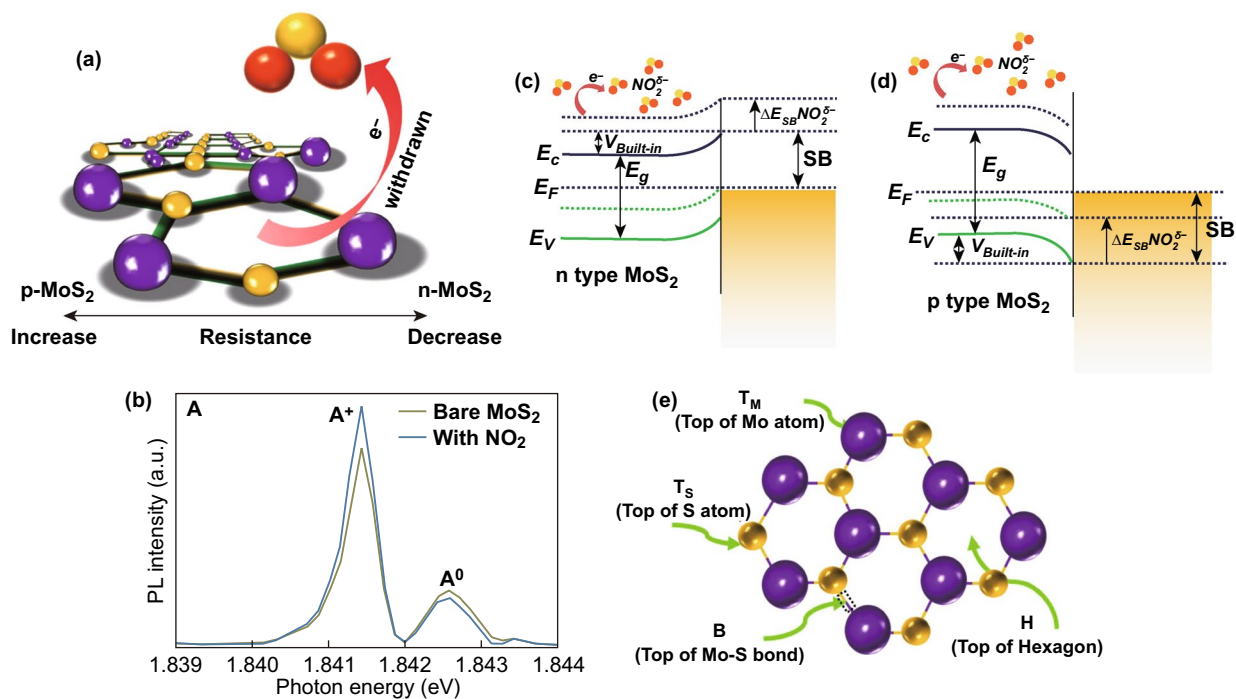


**Fig. 5** a Schematic interaction of NO<sub>2</sub> gas molecules with the n-type or p-type MoS<sub>2</sub> layer. NO<sub>2</sub> captures the electrons from MoS<sub>2</sub> layer. b Effect of NO<sub>2</sub> molecules adsorption on PL spectra. The spectral weight of positively charged trions is increased on the cost of excitons spectral weight in n-type MoS<sub>2</sub>. Reproduced with permission from Ref. [32]. Copyright (2015) American Chemical Society. Schottky barrier modulation after NO<sub>2</sub> molecules adsorption in c n-type MoS<sub>2</sub> d p-type MoS<sub>2</sub>. e Four possible NO<sub>2</sub> adsorption sites on MoS<sub>2</sub>. Reproduced with permission from Ref. [255]. Copyright (2017) AIP Publishing



on the Fermi level of n-type and p-type MoS<sub>2</sub> flakes is shown in Fig. 5c, d. MoS<sub>2</sub> can have both types of semiconducting nature. In both cases, NO<sub>2</sub> exposure depletes the electrons from the MoS<sub>2</sub> and manipulate the charge density in the conduction band. Due to electron extraction, the Fermi level in the n-type MoS<sub>2</sub> film moves downward toward the valence band and correspondingly the SBH and resistance increased. When MoS<sub>2</sub> film has the p-type nature, holes majority increased with NO<sub>2</sub> exposure. The Fermi level move toward the conduction band and SBH and resistance decreased. Thus, NO<sub>2</sub> adsorption critically affects the electronic as well as the optical properties of MoS<sub>2</sub>.

Yue et al. theoretically investigated the adsorption of several molecules using DFT on MoS<sub>2</sub> such as H<sub>2</sub>, O<sub>2</sub>, H<sub>2</sub>O, NH<sub>3</sub>, NO, NO<sub>2</sub>, and CO [117]. Theoretically, gas adsorption behavior is determined by the few terms namely: favorable adsorption sites on MoS<sub>2</sub> for particular gas molecule, distance between the gas molecule and the MoS<sub>2</sub> layer, the binding energy of gas molecule on the MoS<sub>2</sub> layer, charge transfer between the gas molecules and MoS<sub>2</sub> layer, and direction of charge transfer. For adsorption of any gas molecule on a sensing surface, there should be a strong favorable interaction between the gas molecules and MoS<sub>2</sub> flakes, and it should be adsorbed physically or chemically. This interaction is determined in terms of adsorption energy, calculated by Eq. (4):

$$E_a = E_{\text{MoS}_2+\text{molecule}} - (E_{\text{MoS}_2} + E_{\text{molecule}}) \quad (4)$$

where  $E_a$  is the adsorption energy,  $E_{\text{MoS}_2+\text{molecule}}$  is the total energy of MoS<sub>2</sub> and the adsorbed gas molecule.  $E_{\text{MoS}_2}$  and  $E_{\text{molecule}}$  are the energy of the MoS<sub>2</sub> film and single gas molecule, respectively. For a strong interaction, the adsorption energy should be negative and the interaction process should be exothermic. Another term is the charge transfer process. The charge transfer process depends on the relative position of the highest occupied molecular orbitals (HOMO) and lowest unoccupied molecular orbitals (LUMO). If the Fermi level is below the HOMO, then charge transfer from molecule to sensing surface and gas is called the electron donor, and if the Fermi level is above the LUMO, then the charge transfer from sensing surface to molecule and gas called is the electron acceptor [280].

As mentioned above, the adsorption of the gas molecule is determined in terms of favorable adsorption sites. The gas molecules adsorption are highly position dependent in the case of MoS<sub>2</sub> due to the difference in the adsorption energy and charge transfer for gas molecules at different adsorption

sites on MoS<sub>2</sub>. The monolayer of MoS<sub>2</sub> has a hexagonally packed structure where Mo atoms are sandwiched between the two layers of S atoms. There are four possible adsorption sites, the H sites (Top of the hexagon), T<sub>S</sub> (top of S atom), T<sub>M</sub> (top of Mo atom), and B (top of Mo and S bond). The possible sites configurations are shown in Fig. 5e. In the case of NO<sub>2</sub>, three different NO<sub>2</sub> molecules orientations have been considered with these four sites, starting from one N atom with N–O bonds parallel to monolayer, two with NO-bonds pointing up or down to monolayer. After the gas molecule adsorption on MoS<sub>2</sub>, MoS<sub>2</sub> structure with adsorbed gas molecules is reached to the equilibrium state with the highest adsorption energy.

The minimum distance between the adsorbed gas molecule and the relaxed MoS<sub>2</sub> surface is called as equilibrium height. The importance of distance between the NO<sub>2</sub> and top S layer of MoS<sub>2</sub> is also studied and investigated by Yue et al. The highest adsorption energy was found at an equilibrium height of 2.71 Å. It has to be noted that the highest adsorption energy is negative for adsorption of NO<sub>2</sub> on MoS<sub>2</sub>, confirming the favorable adsorption of NO<sub>2</sub> on MoS<sub>2</sub>. Among all, depending on the charge transfer and adsorption energy, the most favorable NO<sub>2</sub> orientation was estimated. The H, T<sub>S</sub>, and B sites (–276, –249, and –249 meV, respectively) found favorable for NO<sub>2</sub> adsorption while no adsorption on T<sub>M</sub> site was observed. The high adsorption energy was attributed to polarization produced in the MoS<sub>2</sub> sheet during NO<sub>2</sub> adsorption. Hence, the interaction was determined by the electrostatic force and lead to strong adsorption energy. From the adsorption energy calculations, the highest favorable NO<sub>2</sub> adsorption site is at the H site. The charge transfer from MoS<sub>2</sub> to NO<sub>2</sub> was found to vary from 0.1e to 0.119e. The positive charge transfer value implies the transfer of charge from MoS<sub>2</sub> to NO<sub>2</sub>. The difference in the charge density due to NO<sub>2</sub> exposure further confirmed the charge accumulation and depletion profile. The effect of NO<sub>2</sub> molecule on energy band structure is also studied and it has been found that the adsorbed NO<sub>2</sub> molecule introduces an unoccupied flat impurity state at 0.31 eV above the Fermi level in the conduction band of MoS<sub>2</sub>. The used method, supercell size, lattice parameters and available favorable adsorption sites for NO<sub>2</sub> molecules adsorption on MoS<sub>2</sub> by Yue et al., are tabulated in Table 1. Another important aspect of the work is the study of the applied electric field on the NO<sub>2</sub> adsorption on MoS<sub>2</sub>. The charge transfer mechanism

**Table 1** Method, supercell size (S.S), lattice parameter (L.P) and favorable adsorption sites on MoS<sub>2</sub> calculated by Yue et al. using DFT [117]

Method	S. S (L.P)	H-site			T <sub>S</sub> -site			B-site			Reference
		d	E <sub>a</sub>	ΔQ	d	E <sub>a</sub>	ΔQ	d	E <sub>a</sub>	ΔQ	
VASP (LDA)	4×4 (3.12)	2.65	-276	0.1	2.71	-249	0.119	2.62	-249	0.114	[117]

between the adsorbents and absorber is the key to the gas molecule adsorption.

The amount of charge transfer is very sensitive to the electric field. The applied electric field is considered in two perpendicular directions (i) MoS<sub>2</sub> to NO<sub>2</sub> molecule (+E) and (ii) NO<sub>2</sub> to MoS<sub>2</sub> molecule (-E). The charge transfers from MoS<sub>2</sub> to NO<sub>2</sub> increase with an increase in the positive electric field and it tends to decrease when the direction of the field is reversed. The negative electric field forces the electrons to transfer from NO<sub>2</sub> to MoS<sub>2</sub>. The external electric field and dipole moment direction are well correlated with each other. Hence the direction of the electric field is greatly affected by the charge transfer values.

#### 4 Theoretical Investigations of NO<sub>2</sub> Adsorption on MoS<sub>2</sub>

Here, we discuss the reports where the interaction of NO<sub>2</sub> on MoS<sub>2</sub>, the role of MoS<sub>2</sub> polytype and metal doping investigated theoretically.

##### 4.1 Adsorption of NO<sub>2</sub> Gas Molecules on Defective MoS<sub>2</sub>

In the present section, we will discuss some theoretical reports in which adsorption of NO<sub>2</sub> is studied on the defective MoS<sub>2</sub>. The two types of defects are considered mainly in MoS<sub>2</sub> the monosulfur vacancies and the Mo-doped S vacancy sites.

Owing to the chemical interaction of NO<sub>2</sub> with MoS<sub>2</sub>, the adsorption mechanism is governed by the chemisorption mechanism. Li et al. used DFT to study the adsorption of NO<sub>2</sub> molecule on the single S vacancy site [281]. Initially, the effect of vacancies on the electronic structures was studied. The schematic of a MoS<sub>2</sub> unit cell is shown in Fig. 6a. The bandgap with a single S vacancy in MoS<sub>2</sub> was decreased up to 1.07 eV [282, 283]. The S vacancies in 2D materials create midgap states which reduce the bandgap of MoS<sub>2</sub>.

These states arise due to the unsaturated Mo atoms near the vacant S sites [284]. When NO<sub>2</sub> molecules are adsorbed to the MoS<sub>2</sub> surface, the NO<sub>2</sub> molecule dissociates at the S vacancy sites into NO and O. The dissociated NO has a bond length equivalent to the free NO molecule. Hence, the dissociated O atom is adsorbed on the single S vacancy site and the other part NO is physisorbed on the O-doped MoS<sub>2</sub>. The activation barrier energy and transition states were also calculated. The activation energy of NO<sub>2</sub> dissociation was 0.21 eV and the reaction energy was 2.30 eV, as shown in Fig. 6b. This energetically favored the NO<sub>2</sub> dissociation process. Furthermore, adsorption energy of physisorbed NO was 0.44 eV which is minimal and facilitates desorption of NO<sub>2</sub> molecules from MoS<sub>2</sub>.

Sahoo et al. doped Mo atoms on S vacancy sites, and enhanced adsorption of NO<sub>2</sub>, as shown in Fig. 6c, d with a red circle [285]. This type of doping is termed as antisite defects (Mo<sub>S</sub>) in MoS<sub>2</sub> (A-MoS<sub>2</sub>). The insertion of Mo atoms at the S defects sites are highly probable with physical vapor deposition techniques. A-MoS<sub>2</sub> may be an innovative method to improve the sensor response, selectivity, and sensing performance of the MoS<sub>2</sub> sensor. The insertion of Mo atom at the S vacancy site generates the three midgap states, two states are at -0.02 and -0.11 eV below the Fermi level and the third state above the Fermi level at 0.28 eV. Actually, 4d orbitals of antisite Mo atom is splitted into three states; a ( $d_z^2$ ) state lies above the fermi level, twofold degenerate  $e_1(d_{xy}, d_{x^2-y^2})$ , and  $e_2(d_{yz}, d_{zx})$  due to the C<sub>3v</sub> symmetry, lies below the Fermi level. It is worth to note that  $e_1$  state splits into  $e'_1$  and  $e''_1$  levels due to the John Teller distortion while  $e_2$  lies well below the valence band. The corresponding density of states (DOS) and partial density of states (PDOS) of Mo antisite-doped MoS<sub>2</sub> without NO<sub>2</sub> and with NO<sub>2</sub> exposure are shown in Fig. 6e. Finally, when NO<sub>2</sub> gas molecules are exposed to A-MoS<sub>2</sub>, the NO<sub>2</sub> interaction process is highly exothermic and higher charge transfer takes place in A-MoS<sub>2</sub> in comparison to the pristine MoS<sub>2</sub>. The paramagnetic NO<sub>2</sub> molecules are adsorbed in the tilted configuration. The strong mixing of antisite defect Mo<sub>S</sub> and of NO<sub>2</sub> orbitals are

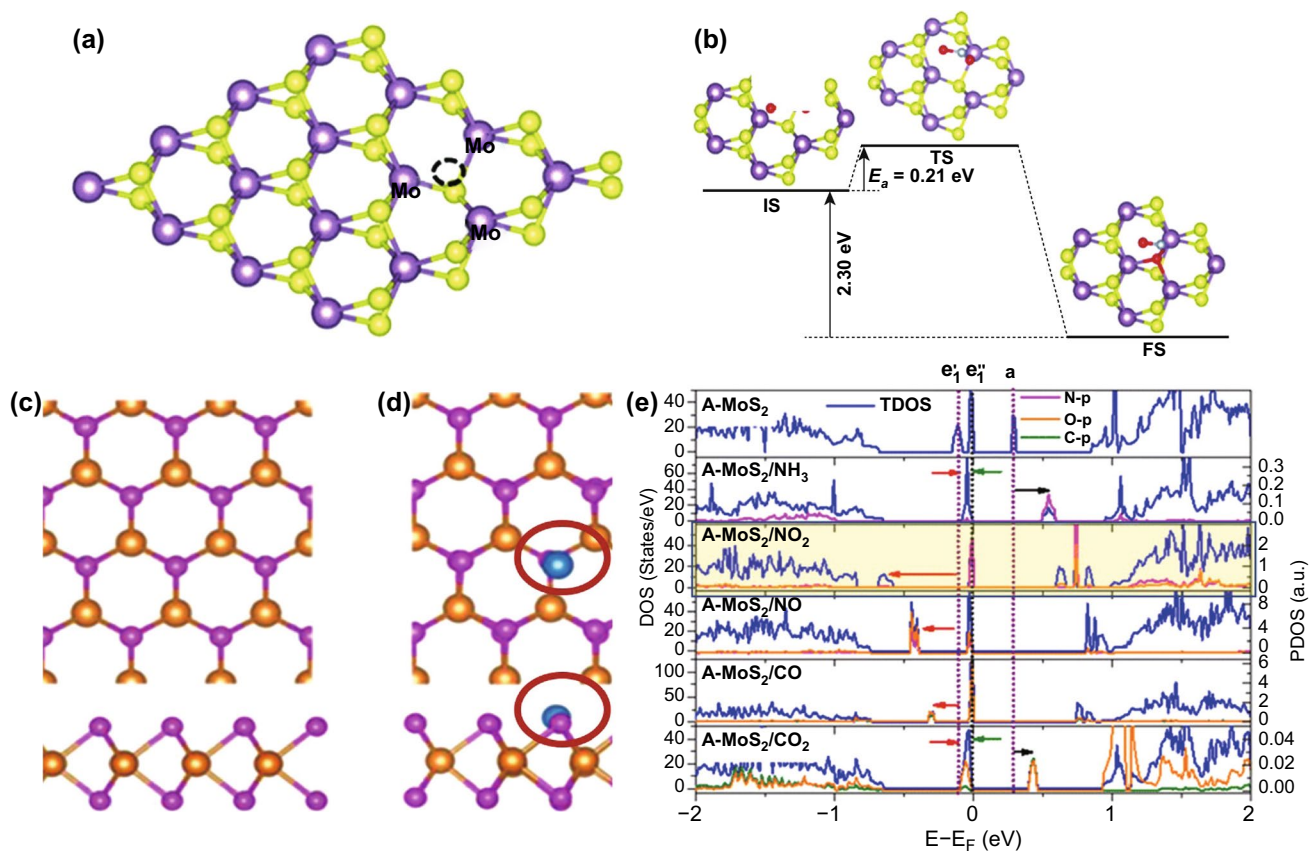


**Fig. 6** **a** Structure of defected MoS<sub>2</sub>. Black circles represent the S vacancy sites. **b** Dissociation of NO<sub>2</sub> onto the S vacant MoS<sub>2</sub>. Mo<sub>s</sub>. Reproduced with permission from Ref. [281]. Copyright (2016) The Royal society of chemistry. **c** Top view of pristine MoS<sub>2</sub> **d** Mo-doped S Antisite defects (Mo<sub>s</sub>) **e** DOS and PDOS of monolayer MoS<sub>2</sub> with Antisite defect-doped MoS<sub>2</sub> with gas molecules exposure. Reproduced with permission from Ref. [285]. Copyright (2016) American Chemical Society

responsible for high charge transfer and strong adsorption energy. The p orbitals of N and O atom of NO<sub>2</sub> molecules are strongly hybridize with the three new mid gap states generated due to the antisites Mo<sub>s</sub> defects. The DOS and PDOS states of A-MoS<sub>2</sub> confirmed this behavior. The strong hybridization occurred between the NO<sub>2</sub> molecule and with three new mid gap states which enhanced the charge transfer.

#### 4.2 Adsorption of NO<sub>2</sub> Gas Molecules on 2H-MoS<sub>2</sub> and 1T-MoS<sub>2</sub> Polytype

The two polytype of MoS<sub>2</sub>, 2H-MoS<sub>2</sub>, and 1T-MoS<sub>2</sub> have their own advantages in NO<sub>2</sub> sensing. Both polytypes have distinct electronic nature of semiconductors (2H-MoS<sub>2</sub>) and metallic (1T-MoS<sub>2</sub>). Here, in this section, we will enlighten the role of both pristine phases and defective phases MoS<sub>2</sub> in NO<sub>2</sub> sensing. Linghu et al. has compared the NO<sub>2</sub> sensing

performance of pristine 2H-MoS<sub>2</sub> and pristine 1T-MoS<sub>2</sub> [286]. The 1T-MoS<sub>2</sub> has shown promising sensing performances in comparison to the 2H-MoS<sub>2</sub>. The geometric optimization revealed that NO<sub>2</sub> has a closer and stronger interaction with the 1T-MoS<sub>2</sub> phase than the 2H-MoS<sub>2</sub>. The calculated adsorption energies for the 2H-MoS<sub>2</sub> and 1T-MoS<sub>2</sub> phases are -0.21 eV and -0.25 eV, respectively, reasonable to assume the higher NO<sub>2</sub> interaction with the 1T phase. The higher adsorption energy comparative to 2H-MoS<sub>2</sub> confirmed the higher and closer interaction in 1T MoS<sub>2</sub>.

Taking a step further, Linghu et al. studied the role of defects in both 2H and 1T polytype and found again that defective 1T-MoS<sub>2</sub> is superior in NO<sub>2</sub> adsorption [287]. The single S vacancy defects are considered in both phases due to their low formation energy requirement.

Figure 7a, b demonstrates the geometric perspective structure with S vacancy of 2H and 1T MoS<sub>2</sub>. The S

vacancies in both 2H and 1T phase affect the electronic structure of the MoS<sub>2</sub>. S vacancies introduced mid gaps states and further reduced the MoS<sub>2</sub> bandgap. Moreover, the metallic behavior of 1T-MoS<sub>2</sub> is increased due to these mid gap states. The band structure of 2H and 1T MoS<sub>2</sub> of pristine and defective MoS<sub>2</sub> are shown in Fig. 7c–f. When NO<sub>2</sub> is exposed to these polytypes, it dissociates in NO and O, as shown in Fig. 7g, h. The O atom tri-coordinated with the neighboring three Mo atom and occupied the S vacancy site and NO gets physisorbed on MoS<sub>2</sub>. The variation of adsorption energy with different molecules is shown in Fig. 7i. The red encircled values depict the NO<sub>2</sub> adsorption energies.

#### 4.3 Theoretical Adsorption of NO<sub>2</sub> Gas Molecules on Metal-Functionalized MoS<sub>2</sub>

The absence of dangling bonds makes the pristine monolayer MoS<sub>2</sub> surface defects free. However, the defects are highly probable and S vacancies are the most favorable defect due to the less energy required for their formation [102, 288–290]. There are various experimental reports in which S defects have been controlled by using the argon and electron irradiation. Filling these mono vacancy sites with substitutional atoms can be a promising way to enhance the chemical, electrical and optical properties of MoS<sub>2</sub> layers [289, 291]. These vacancy sites have been filled with various metal atoms such as Cr, Nb, V, and N, experimentally and the electronic and chemical activities of MoS<sub>2</sub> layers changed dramatically [291–293]. Yuan et al. doped graphene with Al, Si, Cr, and Mn and studied the oxygen adsorption on the metal-doped graphene using DFT. The metal doping tuned the adsorption interaction of oxygen with carbon atoms of graphene. The bonding of the metal atom with the carbon atom is a responsible factor for enhance oxygen adsorption on the doped graphene [294]. Lu et al. embedded the graphene with Au and investigated the CO oxidation using DFT [295]. Au embedding reduces the reaction barrier and increases the oxidation rate of the CO on Au embedded graphene. Similarly, the inert 2D materials surface can be changed to a highly active surface for gas interaction due to the bonding of 2D materials with metal atoms.

Therefore, metal doping has a great impact on the electronic and gas-sensing properties such as adsorption energy, charge transfer, the direction of charge transfer and interaction of gas molecules with the MoS<sub>2</sub> surface. The choice of appropriate metal for a particular gas will strongly modulate the chemical activity, selectivity and sensor response of the MoS<sub>2</sub> surface.

Fan et al. investigated the effect of transition metals (Fe, Co, Ni, Cu, Ag, Au, Rh, Pd, Pt, and Ir) doping on MoS<sub>2</sub> flakes for various gas molecules adsorption (CO, NO, O<sub>2</sub>, NO<sub>2</sub>, and NH<sub>3</sub>). The effect of transition metal doping in the absence of the gas molecules has been systematically studied. All the mentioned metals have been doped on the mono-sulfur vacancy site due to the low formation energy of S vacancies in comparison to other vacancies such as Mo vacancy, dia Mo vacancy and antisite vacancies [102, 288–290]. The equilibrium height (M-Mo) is taken from the metal atom and S atom plane. The stability of the metal embedded MoS<sub>2</sub> in terms of binding energy and charge transfer was tested to have a better grasp. The binding energy ( $E_b$ ) between the metal atom and unexposed MoS<sub>2</sub> is calculated by Eq. (5):

$$E_b = E_{\text{MoS}_2} + E_{\text{metal}} - E_{\text{MoS}_2+\text{metal}} \quad (5)$$

The highest binding energy (energy required to bind the metal atom on the S vacant MoS<sub>2</sub>) was found 5.21 eV for Pt metal atoms and the lowest for 1.98 eV for the Ag atoms. The maximum charge 0.36e was transferred from Fe metal to MoS<sub>2</sub> and the lowest –0.34e to Pt metal atom from MoS<sub>2</sub>. The negative charge value means transition metals obtain the electrons from the MoS<sub>2</sub> and vice versa for positive charge value. The binding energy and charge transfer values mentioned above are without NO<sub>2</sub> exposure. The charge depletion and accumulation between the metals and MoS<sub>2</sub> are due to the Pauling electronegativity. For the case of NO<sub>2</sub> adsorption on the metal-doped MoS<sub>2</sub> sheet, two different modes were obtained after the relaxation of the exposed MoS<sub>2</sub> system. One mode is with Fe, Co, Cu, Ag, and Au embedded MoS<sub>2</sub> system via bonding of two O atoms with transition metals forming TM–O–N–O (four membered ring). The other mode is the bonding of NO<sub>2</sub> with Ni-, Rh-, Pd-, Pt-, and Ir-doped MoS<sub>2</sub> in which N-atom bonded with the transition metal. The adsorption energies and charge transfer in case of NO<sub>2</sub> adsorbed on the metal-doped MoS<sub>2</sub> are tabulated in



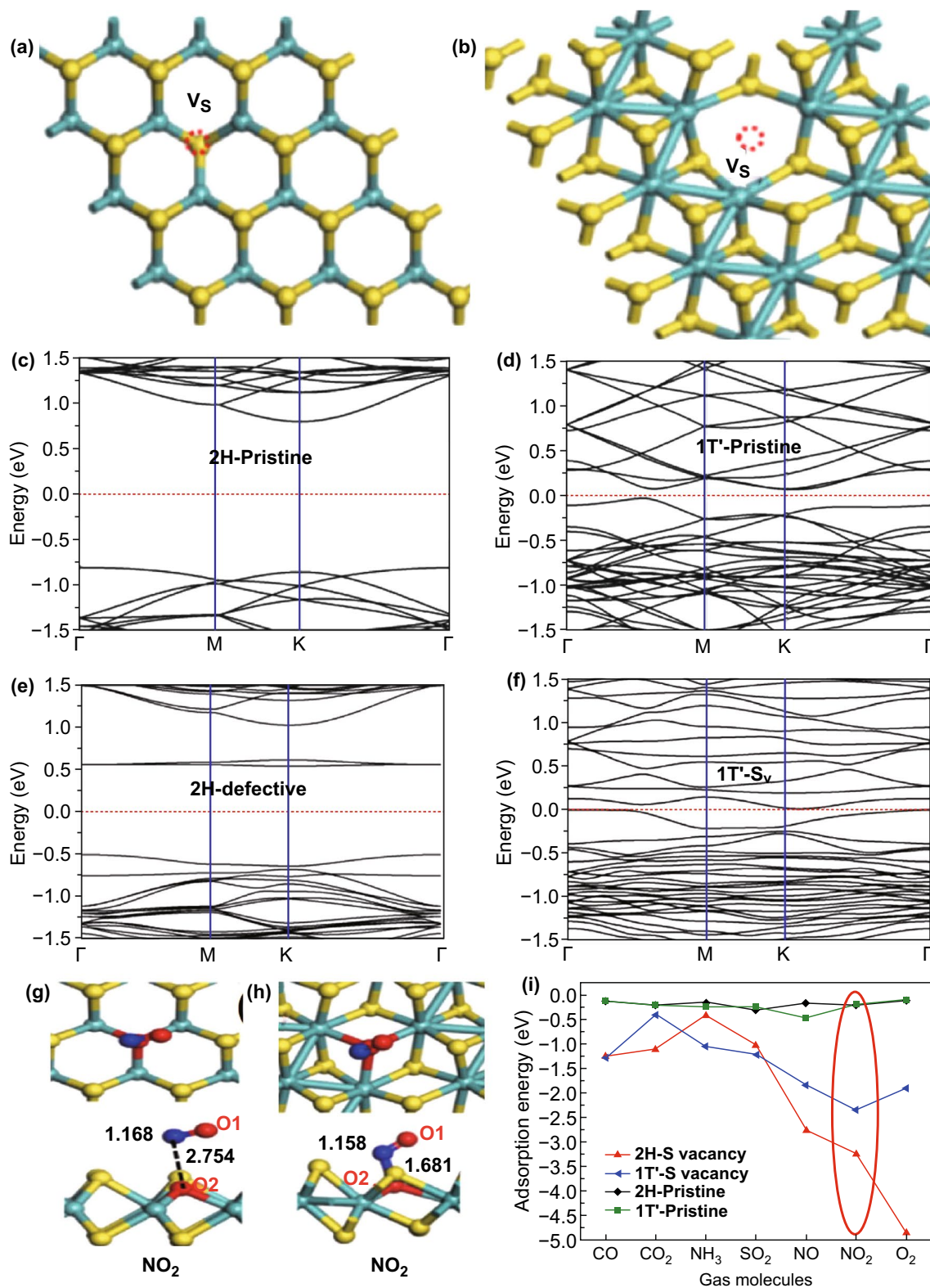


**Fig. 7** **a** S vacancy in 2H-MoS<sub>2</sub>, **b** S vacancy in 1T-MoS<sub>2</sub>, Band structure of **c** pristine 2H-MoS<sub>2</sub>, **d** pristine 1T-MoS<sub>2</sub>, **e** S vacant 2H-MoS<sub>2</sub>, **f** S vacant 1T-MoS<sub>2</sub>. Adsorption of NO<sub>2</sub> on **g** defective 2H-MoS<sub>2</sub>, **h** defective 1T-MoS<sub>2</sub>. **i** Variation of adsorption energy for different molecules. Reproduced from Ref. [286]. Copyright (2019) American Chemical Society

Table 2. Fan et al. calculated the adsorption energy of gas molecules by Eq. (6):

$$E_a = E_{\text{free molecule}} + E_{\text{free sheet}} - E_{\text{adsorbed sheet}} \quad (6)$$

The Fe metal-embedded MoS<sub>2</sub> has shown promising NO<sub>2</sub> adsorption properties with charge transfer value  $-0.66e$  and adsorption energies of 210 meV. The negative values indicate that charge transferred from metal embedded MoS<sub>2</sub> to NO<sub>2</sub> than pristine MoS<sub>2</sub>. These extra electrons are obtained from the embedded transition metals, which reflect the importance of the transition metals. The electronic structure with NO<sub>2</sub> and metal embedded MoS<sub>2</sub> was studied deeply. The higher interaction of NO<sub>2</sub> is due to the mixing of Fe 3d states and 6a1, 1a2, and 4b1 orbitals of NO<sub>2</sub> over a wide range of energy, as shown in the Fig. 8a, b. These mixing or hybridization resulted in enhanced NO<sub>2</sub> interaction with charge transfer of  $-0.66e$ . A similar behavior is observed with other metal-doped MoS<sub>2</sub>.

Luo et al. doped Al, Si, and P metal atoms at the S vacancy site [297]. These metals were chosen because of their exactness and closeness of covalent radii to the radius of the S atom. The NO<sub>2</sub> and NH<sub>3</sub> adsorption were studied at five adsorption sites on MoS<sub>2</sub>. The five adsorption sites are  $T_x$  (gas molecule on top of doped metal),  $H_x$  (gas molecule on top of hexagon near to doped metal),  $T_S$  (gas molecule on top of S atom near to doped metal),  $T_{Mo}$  (gas molecule on top Mo atom near to doped metal). Among all five sites, the most stable site for NO<sub>2</sub> adsorption was  $H_x$  after a complete structure relaxation. The doping of Al, Si, and P generates impurities in the Mo 4d state which create strong hybridization coupling between the Al-3p, Si-3p, and P-3p. Therefore a strong charge is transferred between the atoms and monolayer MoS<sub>2</sub>. Si-doped MoS<sub>2</sub> was found most suitable for NO<sub>2</sub> adsorption due to the highest charge transfer between them. PDOS calculation was performed to investigate the NO<sub>2</sub> adsorption on undoped MoS<sub>2</sub> and doped MoS<sub>2</sub>, and

**Table 2** Summary of the adsorption energy, charge transfer, and method utilized for the calculating the NO<sub>2</sub> adsorption on the various metal-doped

Metal	Supercell Size (lattice parameter in Å)	Method	$E_{\text{ads}}$ (eV)	Charge transfer (e)	References
Fe	4×4 (3.18) $E_a = E_{\text{free molecule}} + E_{\text{free sheet}} - E_{\text{adsorbed sheet}}$	PBE*	1.92	-0.66	[296]
Co			1.45	-0.61	
Ni			0.84	-0.42	
Cu			1.02	-0.64	
Ag			0.54	0.60	
Au			0.65	-0.54	
Rh			1.13	-0.31	
Pd			0.29	-0.34	
Pt			0.37	-0.34	
Ir			1.49	-0.39	
MoS <sub>2</sub>	4×4 (3.17) $E_a = E_{\text{MoS}_2+\text{molecule}} - (E_{\text{MoS}_2} + E_{\text{molecule}})$	PBE	-0.07	-0.02	[297]
Al			-3.02	-0.50	
Si			-2.58	-0.52	
P			-2.134	-0.48	
V	4×4 (3.17) $E_a = E_{\text{free molecule}} + E_{\text{free sheet}} - E_{\text{adsorbed sheet}}$	PBE	2.59	-0.66	[298]
Nb			3.88	-0.69	
Ta			3.64	-0.72	
Ag	4×4 (3.18) $E_a = E_{\text{MoS}_2+\text{molecule}} - (E_{\text{MoS}_2} + E_{\text{molecule}})$	PBE	-2.83	-0.61	[299]
Cu	5×5 (3.18) $E_a = E_{\text{free molecule}} + E_{\text{free sheet}} - E_{\text{adsorbed sheet}}$	PBE	1.66	0.64	[25]

\*Perdew–Bruke–Ernzerh (PBE); The negative value means charge transfers from MoS<sub>2</sub> to gas molecules; the doping site is at S vacancies for all the reports

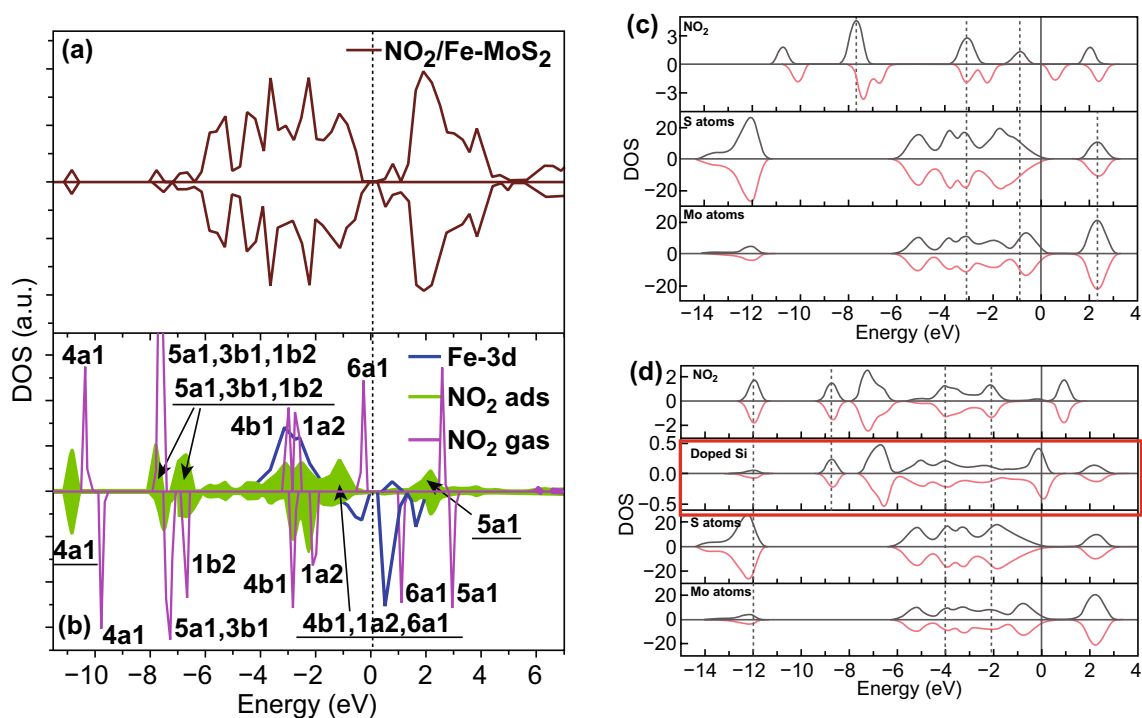


**Fig. 8** **a, b** Total density of states and density of states for Fe-embedded NO<sub>2</sub> molecule. Reproduced with permission from Ref. [296]. Copyright (2017) Elsevier; Calculated projected density of states **c** with NO<sub>2</sub> adsorbed on monolayer MoS<sub>2</sub>, **d** Si-doped MoS<sub>2</sub>. Reproduced with permission from Ref. [297]. Copyright (2016) Elsevier

shown in Fig. 8c, d. In the case of undoped MoS<sub>2</sub>, the NO<sub>2</sub> peaks were situated at  $-7.7$  and  $-3.09$  eV while the PDOS peak of bare MoS<sub>2</sub> was situated at  $2.33$ ,  $-12.04$  and between  $-1.5$  and  $-5$  eV. Hence the weak interaction occurs between NO<sub>2</sub> and MoS<sub>2</sub>. However, when Al was doped in MoS<sub>2</sub>, there is more orbital coupling at  $-1.35$  and  $-3.31$  eV not only with Al orbitals but also with S and Mo orbitals. Hence, the interaction and charge transfer increased with Al doping. NO<sub>2</sub> molecules partially obtained electrons from the doped Al. With Si atom, the hybridization of orbitals is further increased and a higher number of electrons, i.e.,  $0.52e$  transfer to MoS<sub>2</sub>. Similar behavior was observed with the P atom.

Zhu et al. studied the doping of V, Tb, and Ta on the S vacancy site [298]. It is important to note that the size of these metal atoms is large in comparison to the S atom. These atoms are thus situated outside the S plane. Among all, the high binding energy suggested that Ta atoms bound firmly with MoS<sub>2</sub>. The NO<sub>2</sub> gas molecules prefer to make bond on metal atoms. The two oxygen atoms form bond with the metal atom and N atom, and form a four-membered ring like structure M–O–N–O, shown in Fig. 9a–c.

The calculated adsorption energies were  $2.59$ ,  $3.88$ , and  $3.64$  eV for V, Nb, and Ta atoms, respectively. The Bader charge analysis revealed that charge transferred from MoS<sub>2</sub> to NO<sub>2</sub> and with V, Nb, and Ta atoms metals doping. NO<sub>2</sub> has shown strong oxidizing behavior. The charge density differences are shown in Fig. 9d–f. The NO<sub>2</sub> adsorption with monolayer MoS<sub>2</sub> were further calculated with NO<sub>2</sub> exposure.

However, the charge transfer and adsorption energies are comparatively smaller than metal-doped V, Nb, and Ta. Moreover, NO<sub>2</sub> as a paramagnetic molecule is critically affected by the bond length [300]. The bond length was  $1.21$  Å in the case of pristine MoS<sub>2</sub> while NO<sub>2</sub> bond length was elongated from  $0.07$  to  $-0.11$  Å with metal-doped MoS<sub>2</sub>. Thus, the NO<sub>2</sub> activation on metal-doped MoS<sub>2</sub> is enhanced. Further electronic properties of MoS<sub>2</sub> after NO<sub>2</sub> doping was analyzed in terms of DOS, shown in Fig. 9g–i. The metal orbitals and NO<sub>2</sub> orbitals have a strong hybridization between their orbitals. The d orbitals of metals especially for Nb atoms get mixed with NO<sub>2</sub> orbitals over a wide range of energy. Hence, doping of MoS<sub>2</sub> with V, Nb, and Ta improves the electronic and chemical performance of the NO<sub>2</sub> molecule. The supercell

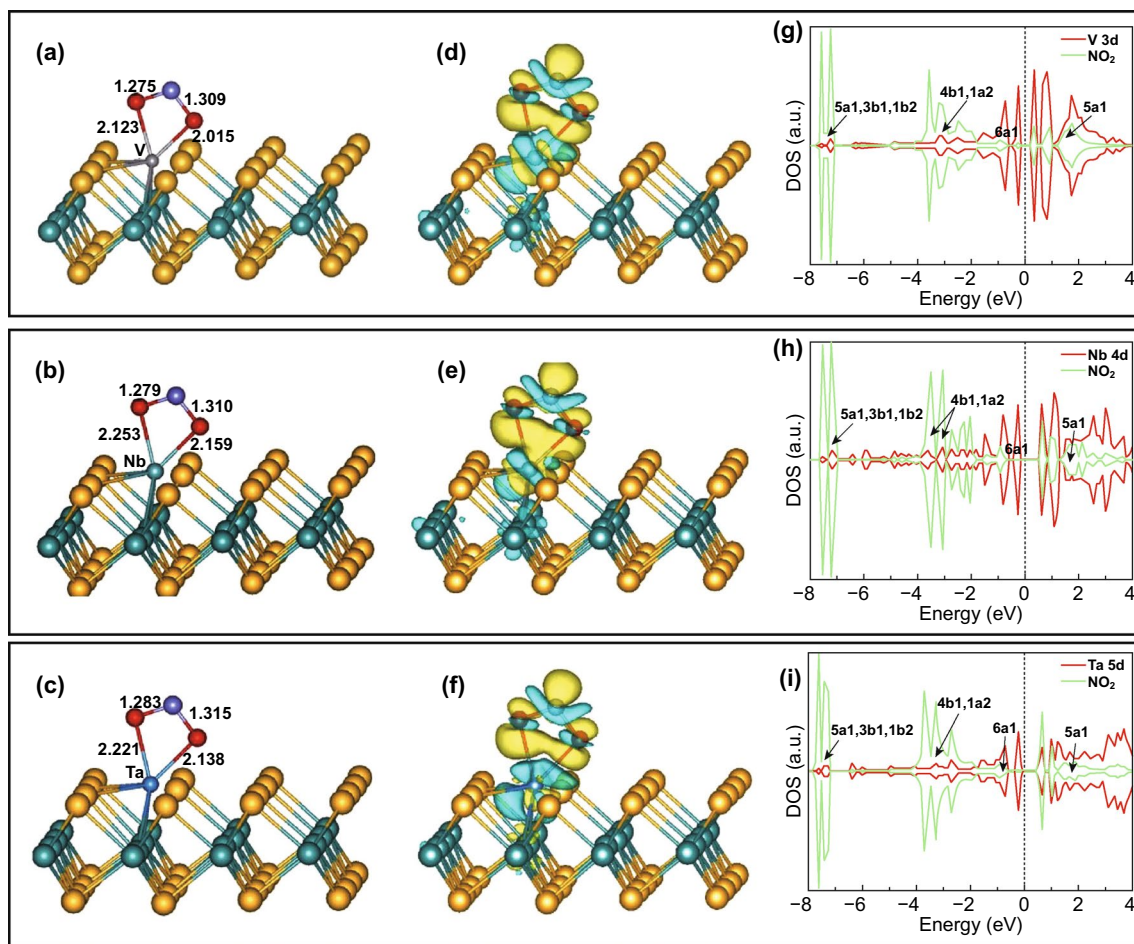


**Fig. 9** **a, d, g**  $\text{NO}_2$  molecule adsorbed on V metal: optimized geometry after  $\text{NO}_2$  adsorption (**a**), charge density difference (**d**), spin-polarized density of state with V 3d and  $\text{NO}_2$  (**g**). **b, e, h**  $\text{NO}_2$  molecule adsorbed on Nb metal: optimized geometry after  $\text{NO}_2$  adsorption (**b**), charge density difference (**e**), spin-polarized density of state with Nb 4d and  $\text{NO}_2$  (**h**). **c, f, i**  $\text{NO}_2$  molecule adsorbed on Ta metal: optimized geometry after  $\text{NO}_2$  adsorption (**c**), charge density difference (**f**), spin-polarized density of state with Ta 5d and  $\text{NO}_2$  (**i**). Reproduced with permission from Ref. [298]. Copyright (2017) Elsevier

size, lattice parameter, occupied method, adsorption energy, and charge transfer are summarized in Table 2.

## 5 Experimental Investigations of $\text{NO}_2$ Adsorption on $\text{MoS}_2$

In this section, we discuss various experimental approaches employed to develop the  $\text{NO}_2$  sensors. This section has been divided into five sub-section in which we summarize the various experimental approaches adopted in terms of bare  $\text{MoS}_2$ , morphology-driven  $\text{MoS}_2$ , metal-doped  $\text{MoS}_2$ , vacancy-driven  $\text{MoS}_2$ , and finally light-assisted  $\text{MoS}_2$ -based  $\text{NO}_2$  sensors.

### 5.1 Bare $\text{MoS}_2$ $\text{NO}_2$ Sensor

Here, we addressed several efforts and experimental reports where  $\text{NO}_2$  sensors were fabricated with single and multilayered  $\text{MoS}_2$  flakes. The reports include the impact of  $\text{NO}_2$  adsorption on the single and multilayer  $\text{MoS}_2$  and as well as the on the SBH. Li et al. developed the first  $\text{NO}_x$  gas sensor using an n-type  $\text{MoS}_2$  flakes-based FET device [34]. The schematic of fabricated device is shown in Fig. 10a. The monolayer (1L) to quadrilayer (4L)  $\text{MoS}_2$  flakes were synthesized by the mechanical exfoliation technique and had the detection limit of 0.8 ppm. The thickness of the  $\text{MoS}_2$  layers was confirmed by the atomic force microscopy (AFM) technique. The current versus voltage



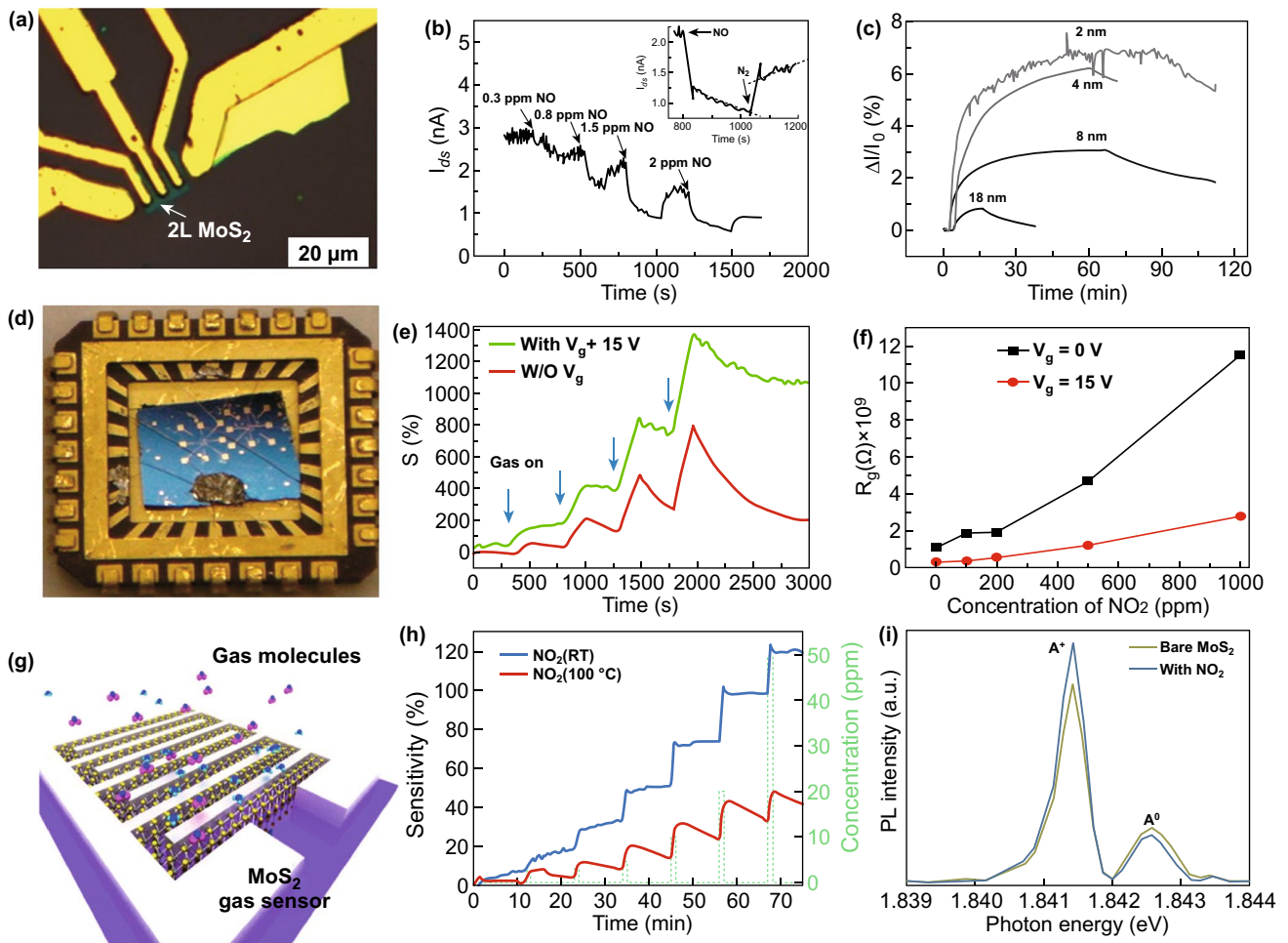


**Fig. 10** **a** Optical image of bilayer MoS<sub>2</sub>-based FET NO sensor. **b** MoS<sub>2</sub> FET response to different concentrations NO. The inset showed the typical response and recovery of the MoS<sub>2</sub> FET device. Reproduced with permission from Ref. [34]. Copyright (2012) Wiley-VCH. **c** MoS<sub>2</sub> TFT NO<sub>2</sub> sensor with different thickness MoS<sub>2</sub> flakes. Reproduced with permission from Ref. [42]. Copyright (2012) Wiley-VCH; **d** optical image of MoS<sub>2</sub> device mounted on a chip. **e** NO<sub>2</sub> response for the bi and five-layer MoS<sub>2</sub> devices at different gate voltages. **f** Theoretically calculated resistance variation with different gate voltages. Reproduced with permission from Ref. [17]. Copyright (2013) American Chemical Society. **g** Device schematic of atomic layer MoS<sub>2</sub>-based sensing device. **h** Response of NO<sub>2</sub> at RT and at moderate temperature of 100 °C. **i** Change in the low energy PL peak due to NO<sub>2</sub> adsorption. Reproduced with permission from Ref. [32]. Copyright (2015) Springer Nature

characteristics measurements of the device with varied layers were performed. The single layer device showed unstable behavior while bi- to quadrilayer film-based devices demonstrated better sensing performance. The NO gas exposure to bilayer MoS<sub>2</sub> film showed a decrease in the current, which confirm the p-type doping due to the electron acceptor nature of the NO gas [57, 301]. Figure 10b displays the gas-sensing performance of the MoS<sub>2</sub> device with different NO concentrations. The adsorption and desorption rate of NO was a two-step process: fast rate and slower rate. The fast reduction in current confirmed the presence of a large number of NO adsorption sites and

slow reduction confirmed saturation of MoS<sub>2</sub> film in NO exposure. Another significant aspect of the different thickness of MoS<sub>2</sub> film was the quick response to NO exposure. The single layer MoS<sub>2</sub> film showed a 50% response within 5 s while multilayer MoS<sub>2</sub> showed a 50% response in 30 s. However, the disadvantage with single-layer MoS<sub>2</sub> film was its instability.

He et al. developed a flexible MoS<sub>2</sub> thin film transistor (TFT) arrays for the NO<sub>2</sub> sensing [42]. The single layer MoS<sub>2</sub> film suspension was drop cast over patterned rGO electrodes covered with Ag pads. The Ag pads had only been used to improve the robustness of the rGO electrodes.

The MoS<sub>2</sub> area and thickness for NO<sub>2</sub> sensing were 1.5 mm<sup>2</sup> and 2, 4, 8, and 18 nm, respectively. It is worth to note that the deposited MoS<sub>2</sub> film showed p-type behavior attributing to the structural changes caused by the lithium intercalation process. The structural changes in the MoS<sub>2</sub> lead to a change in the band structures. During distortion from the octahedral system to zigzag chain, the system was filled up to  $d^{2+n}$  states. Hence, residual negative charges semi filled the bands and contributed to p-type conductivity [302]. The NO<sub>2</sub> gas exposed to the various thickness of MoS<sub>2</sub> film and the highest change in the sensor response was occurred for the thinnest MoS<sub>2</sub> film. The NO<sub>2</sub> exposure increased the conductance of the film due to its electron acceptor nature. The high NO<sub>2</sub> detection ability of thin MoS<sub>2</sub> film was attributed to the increased surface area available in 2 nm film. The sensor response of different thickness of MoS<sub>2</sub> film is shown in Fig. 10c. Late et al. studied the NO<sub>2</sub> sensing behavior of single and multiple layer MoS<sub>2</sub> film synthesized by the mechanical exfoliation method [17]. A detailed gas-sensing performance with and without applying the bias voltage was presented. A detailed AFM, Raman, and TEM characterization were performed to understand the thickness, expansion, crystallographic orientation, and structure of MoS<sub>2</sub>. The device schematic with Ti/Au contact is shown in Fig. 10d. The  $I$ - $V$  characteristic of single layer MoS<sub>2</sub> device was unstable while multilayer MoS<sub>2</sub> showed stable  $I$ - $V$  characteristics. Few layers (single and five layers) MoS<sub>2</sub> device demonstrated good behavior. The three and four-layer MoS<sub>2</sub> flakes device showed identical behavior to two layer and five-layer devices. The NO<sub>2</sub> sensing for five-layer MoS<sub>2</sub> device is shown in Fig. 10e. However, this higher performance was due to the redox potential that greatly influences the sensing behavior of MoS<sub>2</sub> flakes. Once again, the NO<sub>2</sub> interaction with MoS<sub>2</sub> revealed that the NO<sub>2</sub> has an electron acceptor nature. The influence of the external electric field in terms of bias voltage on the NO<sub>2</sub> sensing was further studied. When a positive back gate biasing voltage + 15 V was applied to two and five layers of MoS<sub>2</sub> flakes, the sensor response was improved in comparison to zero bias voltage. A larger number of electrons were collected at the MoS<sub>2</sub> and SiO<sub>2</sub> interface under positive back gate voltage. Therefore, NO<sub>2</sub> has a higher number of electrons to detach from the MoS<sub>2</sub>. With positive gate biasing voltage, the NO<sub>2</sub> sensor response was thus increased. In addition, Ti/Au electrode played a vital role under positive gate voltage. Under positive gate voltage, electrons get accumulated in MoS<sub>2</sub>

film and the barrier between the electrode and MoS<sub>2</sub> film is reduced. Thus, the charge transfer in MoS<sub>2</sub> film facilitated further. The device resistance in the presence of NO<sub>2</sub> gas is shown in Fig. 10f at different biasing voltages.

Cho et al. synthesized the atomic layered MoS<sub>2</sub> flakes by the CVD technique and performed the NO<sub>2</sub> gas sensing [32]. The resistance of the n-type MoS<sub>2</sub> film increased due to the electron-accepting nature of NO<sub>2</sub>. The interdigitated electrodes of Ag metal were fabricated on the MoS<sub>2</sub> film. The NO<sub>2</sub> sensing performance was studied at RT and at a moderate temperature of 100 °C.

The device schematic and NO<sub>2</sub> sensor response versus time profile at each temperature are shown in Fig. 10g, h. It can be seen clearly that the RT sensor response was quite high in comparison to 100 °C, while the sensor showed rapid recovery at 100 °C and no recovery was obtained at RT. The NO<sub>2</sub> gas strongly adsorbed on MoS<sub>2</sub> and hence at RT the desorption rate is quite low. However, thermal energy greatly impacts the adsorption of NO<sub>2</sub> at a higher temperature. The thermal energy accelerates the NO<sub>2</sub> desorption rate than the adsorption rate. As a result, the NO<sub>2</sub> gas interaction decreases at a higher temperature at the sensor response cost. The NO<sub>2</sub> sensing mechanism based on the charge transfer process, confirmed by the change in the peaks of PL spectra is shown by Fig. 10i, as we discussed in Fig. 5b of Sect. 3.

These all layer-dependent studies show that the single layer MoS<sub>2</sub>-based gas sensors suffered from unstable current, but they have a quick response with NO<sub>2</sub> exposure. The few layer MoS<sub>2</sub> flakes-based gas sensors show a good response with the stable current. Moreover, the MoS<sub>2</sub> FET gas sensors are very sensitive to the applied bias voltage. However, the MoS<sub>2</sub> gas sensors have an incomplete recovery at RT. So, operating sensors at a higher temperature may be a good option to achieve full recovery but it will reduce the sensor response. The summary of the results for bare MoS<sub>2</sub>-based NO<sub>2</sub> gas sensors by various groups are tabulated in Table 3.

Liu et al. studied the NO<sub>2</sub> sensing efficiency of monolayer MoS<sub>2</sub> flakes grown by CVD [36, 303]. The effect of gas molecules adsorption on the Schottky barrier height (SBH) between the MoS<sub>2</sub> and metal electrodes was studied. The sensing device area was 1 μm<sup>2</sup> and film showed the 3 cm<sup>2</sup> V<sup>-1</sup> s<sup>-1</sup> mobility with Ti/Au electrodes, shown in Fig. 11a. The Ti was used for improving the electrode adhesion with MoS<sub>2</sub> film. The device showed highly rectifying behavior with a positive and negative drain to source voltage

**Table 3** Summary of the reported NO<sub>2</sub> sensor based on the MoS<sub>2</sub>

Sensing film	Type	Method	Def.	Electrodes	Device	Conc. (ppm)	Tem. (°C)	S (%)	Res time	Rec time	References
1L MoS <sub>2</sub>	n	M.E.	$\left(\frac{I_{\text{gas}} - I_{\text{air}}}{I_{\text{air}}}\right)$	Ti/Au	FET	2	RT	80	-	-	[34]
MoS <sub>2</sub> sheets	p	E.L.	$\left(\frac{R_{\text{gas}} - R_{\text{air}}}{R_{\text{air}}}\right)$	rGO	TFT	1.2	RT	7	-	-	[42]
5L MoS <sub>2</sub>	n	M.E.	$\left(\frac{R_{\text{gas}} - R_{\text{air}}}{R_{\text{air}}}\right)$	Ti/Au	FET	1000	RT	1372	300	600	[17]
1L MoS <sub>2</sub>	n	CVD	$\left(\frac{G_{\text{gas}} - G_{\text{air}}}{G_{\text{air}}}\right)$	Ti/Au	FET	.02	RT	>20	300	-	[36]
3L MoS <sub>2</sub>	p	CVD	$\left(\frac{I_{\text{gas}} - I_{\text{air}}}{I_{\text{air}}}\right)$	Al	Resistor	10	RT	80	-	-	[303]
2L MoS <sub>2</sub>	p	CVD	$\left(\frac{I_{\text{gas}} - I_{\text{air}}}{I_{\text{air}}}\right)$	Ag	Resistor	10	RT	98	-	-	[303]
4L MoS <sub>2</sub>	p	CVD	$\left(\frac{I_{\text{gas}} - I_{\text{air}}}{I_{\text{air}}}\right)$	Au	Resistor	10	RT	60	-	-	[303]
Atomic layered MoS <sub>2</sub>	n	CVD	$\left(\frac{R_{\text{gas}} - R_{\text{air}}}{R_{\text{air}}}\right)$	Ag	Resistor	50	RT	~120	-	-	[32]
Atomic layered MoS <sub>2</sub>	n	CVD	$\left(\frac{R_{\text{gas}} - R_{\text{air}}}{R_{\text{air}}}\right)$	Ag	Resistor	50	100	>40	-	-	[32]
Few layer MoS <sub>2</sub>	p	L.E.	$\frac{R_{\text{gas}}}{R_{\text{air}}}$	Pt	Resistor	1	200	1.15	660	720	[31]
Few layer MoS <sub>2</sub>	n	L.E.	$\frac{R_{\text{gas}}}{R_{\text{air}}}$	Pt	Resistor	1	200	5.80	2460	2340	[31]
Vertical MoS <sub>2</sub>	p	CVD	$\left(\frac{R_{\text{gas}} - R_{\text{air}}}{R_{\text{air}}}\right)$	Ti/Au	Resistor	100	RT	>10	-	-	[35]
Vertical MoS <sub>2</sub>	n	CVD	$\left(\frac{R_{\text{gas}} - R_{\text{air}}}{R_{\text{air}}}\right)$	Au/Cr	Resistor	50	RT	48.32	98	-	[304]
Vertical MoS <sub>2</sub>	n	CVD	$\left(\frac{R_{\text{gas}} - R_{\text{air}}}{R_{\text{air}}}\right)$	Au/Cr	Resistor	50	RT	24.26	34	132	[304]
2L MoS <sub>2</sub>	p	CVD	$\left(\frac{R_{\text{gas}} - R_{\text{air}}}{R_{\text{air}}}\right)$	Au	Resistor	1	RT	2.6	678	318	[305]
Mixed MoS <sub>2</sub>	p	CVD	$\left(\frac{R_{\text{gas}} - R_{\text{air}}}{R_{\text{air}}}\right)$	Au/Cr	Resistor	10	RT	10.36	8.51	-	[120]
Mixed MoS <sub>2</sub>	p	CVD	$\left(\frac{R_{\text{gas}} - R_{\text{air}}}{R_{\text{air}}}\right)$	Au/Cr	Resistor	10	125	7.79	4.44	19.6	[120]
MoS <sub>2</sub> NWs	n	CVD	$\left(\frac{R_{\text{air}} - R_{\text{gas}}}{R_{\text{air}}}\right)$	Au	Resistor	5	60	18.1	16	172	[214]
MoS <sub>2</sub> nanoflower	p	Hyd.	$\frac{R_{\text{gas}}}{R_{\text{air}}}$	Au	Resistor	50	150	78	-	-	[33]
MoS <sub>2</sub> nanosphere/CTAB	n	Hyd.	$\left(\frac{R_{\text{air}} - R_{\text{gas}}}{R_{\text{air}}}\right)$	Ag/Pd	Resistor	50	150	60	15	12	[306]



**Table 3** (continued)

Sensing film	Type	Method	Def.	Electrodes	Device	Conc. (ppm)	Tem. (°C)	S (%)	Res time	Rec time	References
MoS <sub>2</sub> hollow microsphere	p	Hyd.	$\left(\frac{R_{\text{air}}-R_{\text{gas}}}{R_{\text{air}}}\right)$	Au/Cr	Resistor	100	150	40.3	79	225	[307]
MoS <sub>2</sub> Nanoflowers	p	Hyd.	$\left(\frac{R_{\text{air}}-R_{\text{gas}}}{R_{\text{air}}}\right)$	Pt	Resistor	5	RT	67.4	125	485	[308]
MoS <sub>2</sub> Nanoflowers	p	Hyd.	$\left(\frac{R_{\text{air}}-R_{\text{gas}}}{R_{\text{air}}}\right)$	Pt	Resistor	5	150	22	95	320	[308]
MoS <sub>2</sub> Aerogel	p	T.D.	$\left(\frac{R_{\text{gas}}-R_{\text{air}}}{R_{\text{air}}}\right)$	Pt/Ti	Resistor	0.5	200	11	33	107	[24]
MoS <sub>2</sub> Nanosheets	p	M.E.	$\frac{R_{\text{gas}}}{R_{\text{air}}}$	Ag/Pd	Resistor	100	RT	29	42	2	[309]
MoS <sub>2</sub> -W	n	Hyd.	$\left(\frac{R_{\text{air}}-R_{\text{gas}}}{R_{\text{air}}}\right)$	Ag/Pd	Resistor	20	RT	171	41	39	[121]
MoS <sub>2</sub> -Au	p	S.P.	$\left(\frac{R_{\text{gas}}-R_{\text{air}}}{R_{\text{air}}}\right)$	Au	Resistor	2.5	RT	30	240	840	[121]
rGO/Sv-MoS <sub>2</sub>	p	CVD	$\left(\frac{R_{\text{gas}}-R_{\text{air}}}{R_{\text{air}}}\right)$	Au	Resistor	50	50	72	56	328	[310]
MoS <sub>2</sub>	n	CVD	$\left(\frac{R_{\text{gas}}-R_{\text{air}}}{R_{\text{air}}}\right)$	Au	Resistor	50	50	27	142	-	[310]
Multi MoS <sub>2</sub>	n	CVD	$\left(\frac{R_{\text{gas}}-R_{\text{air}}}{R_{\text{air}}}\right)$	Au/Cr	Resistor	100	RT	27.92	249	-	[119]
Multi MoS <sub>2</sub>	n	CVD	$\left(\frac{R_{\text{gas}}-R_{\text{air}}}{R_{\text{air}}}\right)$	Au/Cr	Resistor	100	100	21.56	71	310	[119]
MoS <sub>2</sub> -Au NPs	p	Redox	$\left(\frac{R_{\text{gas}}-R_{\text{air}}}{R_{\text{air}}}\right)$	Au	Resistor	2.5	RT	30	240	840	[121]

Mechanical exfoliation (M.E.); liquid exfoliation (L.E.); electrochemical lithiation (E.L.); hydrothermal (Hyd.); thermal decomposition (T.D.); solution processed (S.P.)



( $V_{DS}$ ) with 400 ppb  $\text{NO}_2$  exposure, as shown in Fig. 11b. The device showed an excellent sensor response of 174% with back gate voltage 30 V. The response time was 300 to 540 s with the full recovery in 12 h. To confirm the  $\text{NO}_2$  gas-sensing mechanism via the charge transfer process, the back gate voltage was fixed at 5 V and gas concentration was varied from 20 to 400 ppb. The threshold voltage for the  $\text{NO}_2$  sensing received a monotonic shift in the positive  $V_{DS}$  direction. The resistance modulation in the device due to gas exposure is the sum of channel resistance ( $R_{\text{channel}}$ ) and  $R_{\text{contact}}$  determined by Eq. (7):

$$R = \left( R_{\text{channel}} \propto \frac{1}{n} \right) + \left( R_{\text{contact}} \propto \frac{1}{n} e^{\frac{\varphi_{\text{SB}}}{kT}} \right) \quad (7)$$

where  $n$  is the electron concentration,  $\varphi_{\text{SB}}$  is the Schottky barrier height between the  $\text{MoS}_2$  and metal electrodes. The SBH is greatly influenced by the above equation when the electron concentration in the device is changed. Figure 11c, d indicates the transfer characteristics at a fixed back gate voltage of 5 V. An increment in the threshold voltage with higher gas concentration is observed.  $\text{NO}_2$  is strong oxidizing gas and has an electron acceptor nature. More number of electrons withdraw from  $\text{MoS}_2$  film as the gas concentration is increased. Thus, a monotonic shift in the positive  $V_{DS}$  direction was observed. Considering the effect of the  $\text{NO}_2$  adsorption on SBH, the proposed band alignment before and after exposure to  $\text{NO}_2$  is shown in Fig. 11e, f.  $\text{NO}_2$  gas captured the electrons from the conduction band and the electron concentration in  $\text{MoS}_2$  film was decreased. The decrease in electron concentration shifts the Fermi level towards the valence band which increases the SBH. Hence, the conductance is decreased.

Kim et al. recently fabricated the  $\text{MoS}_2$  gas sensor with different metal contacts of different work functions [303]. The sensor response of the  $\text{MoS}_2$  sensor was different with different metals. First, the effect of the layer thickness from single to four layers with Au electrodes was studied. The  $I$ - $V$  characteristic is shown in Fig. 11h revealed a linear behavior and a decrease in resistance with an increase in layer observed. The work-function was increased with the number of layers, shown in Fig. 11g. Hence, for a higher number of layers, the SBH is decreased and according to Eq. 11, the resistance is also decreased. Further,  $\text{NO}_2$  exposure on different thickness layer devices is also displayed in Fig. 11i. The device showed p-type behavior to  $\text{NO}_2$  exposure. Further, the bilayer  $\text{MoS}_2$  device showed the highest sensor response for 10 ppm  $\text{NO}_2$  concentration

up to 60%. Finally, for bilayer and trilayer  $\text{MoS}_2$ , the Au ( $\varphi_M = 5.1$  eV), Al ( $\varphi_M = 4.06$  eV), and Ag ( $\varphi_M = 4.26$  eV) electrodes were used. Among all, aluminum electrode-based sensing device showed promising sensor response, 80% for bilayer and 98% for trilayer  $\text{MoS}_2$ -based device. Conclusively, the device with lower work function metal electrodes showed better performance. The band alignment between the aluminum (lower work function metal) and  $\text{MoS}_2$  is responsible for high performance as shown in Fig. 11l-o. The SBH is higher for Al electrodes than the Au electrodes. Under positive biasing, a higher number of holes are transferred from Au electrode due to the low SBH. When  $\text{NO}_2$  gas is exposed, the SBH decreases with a decrease in electron depletion due to the p-type nature. Relatively, the ratio of charge transferred in Al/ $\text{MoS}_2$  device is higher than the Au/ $\text{MoS}_2$ . Hence, better performance is observed.

These reports confirmed that sensing response is critically affected by the SBH. In chemiresistance gas sensors, the SBH is modulated with gas molecules adsorption due to charge transfer between the molecules and sensing film. Thus, Schottky contacted devices are a good candidate for fabricating gas sensors. Hence, the choice of metal contacts played an important role in gas sensing.

## 5.2 Morphology-Driven $\text{NO}_2$ Sensors

In the 2D materials, especially in  $\text{MoS}_2$ , morphology plays a vital role in determining the optical, electrical, and catalytic properties. The  $\text{NO}_2$  molecule adsorption in  $\text{MoS}_2$  is position-dependent and there are specific  $\text{NO}_2$  favourable sites for molecules adsorption in  $\text{MoS}_2$ . These favourable  $\text{NO}_2$  adsorption sites can be controlled by synthesizing various  $\text{MoS}_2$  film surface morphology. In this section, we will discuss various reports where morphology-dependent  $\text{NO}_2$  sensors based on  $\text{MoS}_2$  developed.

Cho et al. studied the role of  $\text{MoS}_2$  edges in  $\text{NO}_2$  gas molecules adsorption [35]. The orientation of the  $\text{MoS}_2$  film greatly affects the adsorption of  $\text{NO}_2$  molecules. Authors varied the orientation of the  $\text{MoS}_2$  film from horizontal to vertical align by depositing different thickness Mo films. The surface topography is shown in Fig. 12a. The inset of the Fig. 12a showed the schematic of the sensing device with an active area of  $100\mu\text{m}^2$ . The  $\text{NO}_2$  gas molecule adsorption enhanced up to fivefold in vertical aligned  $\text{MoS}_2$  flakes

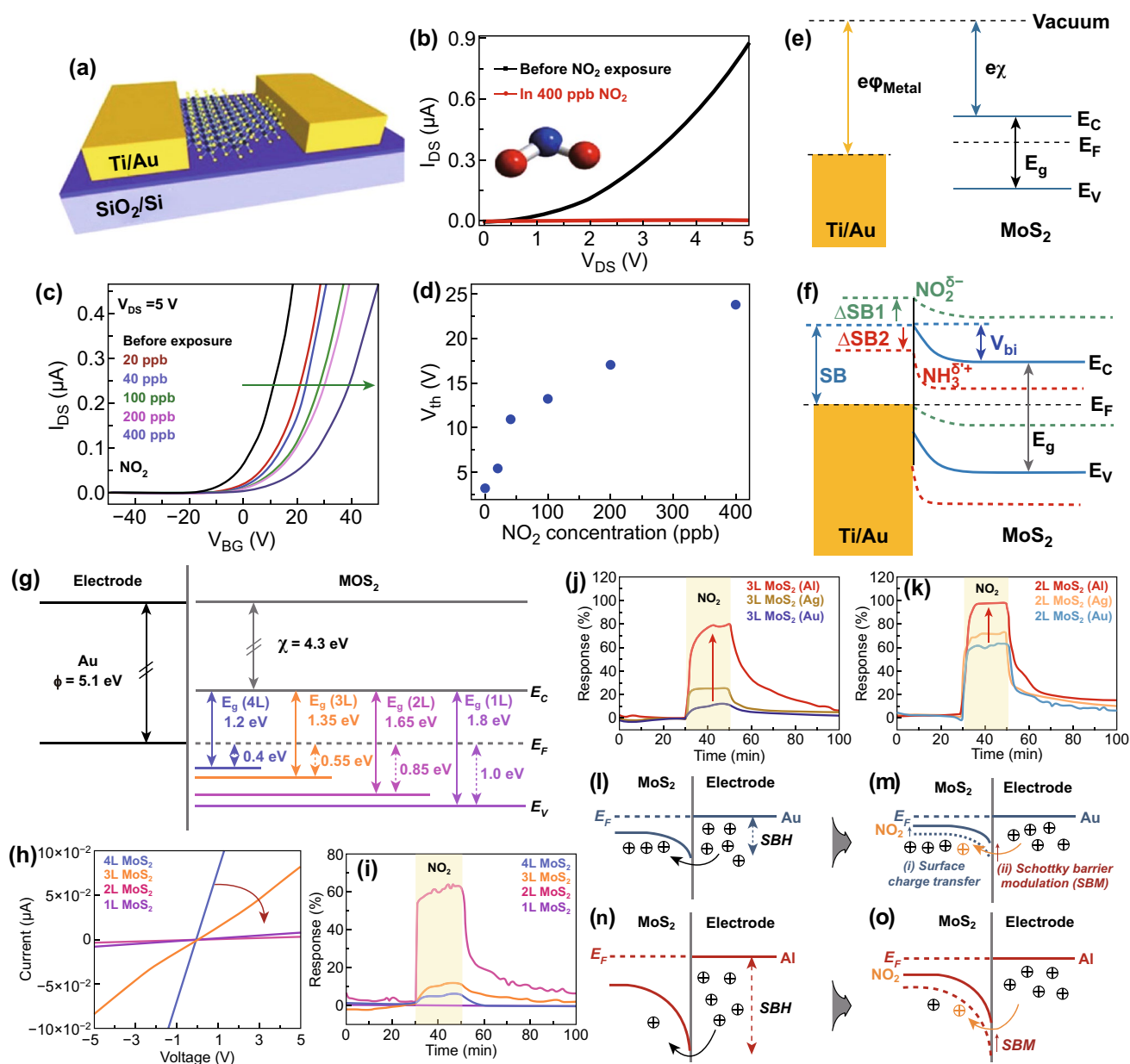


**Fig. 11** **a** Schematic of the monolayer MoS<sub>2</sub> device. **b** Change in current after 400 ppb NO<sub>2</sub> exposure. **c** *I*-*V* characteristics after the NO<sub>2</sub> exposure of different concentration. **d** A monotonic shift in threshold voltage towards the positive side of applied voltage. **e**, **f** Energy band alignment before and after NO<sub>2</sub> exposure. The blue solid lines are corresponding to the band alignment of MoS<sub>2</sub> and Ti/Au contact in the absence of NO<sub>2</sub> while the green dotted lines are corresponding to NO<sub>2</sub> exposure. Reproduced with permission from Ref. [36]. Copyright (2014) American Chemical Society. **g** Band alignment of MoS<sub>2</sub> with Au metal contact. **h** Current versus voltage characteristics with gold contact. **i** NO<sub>2</sub> response with MoS<sub>2</sub>-Au device. Sensor response for NO<sub>2</sub> with different metal contacts Al, Ag, and Au electrodes: **j** 3L MoS<sub>2</sub> film, **k** 2L MoS<sub>2</sub> film. Proposed band alignment of MoS<sub>2</sub>-Au device: **l** before, **m** after NO<sub>2</sub> exposure. Proposed band alignment of MoS<sub>2</sub>-Al device: **n** before, **o** after NO<sub>2</sub> exposure. Reproduced with permission from Ref. [303]. Copyright (2019) American Chemical Society. (Color figure online)

compared to the horizontal MoS<sub>2</sub> film, as shown in Fig. 12b. The Mo film was deposited through an electron beam evaporator and was sulfurized in the CVD. The orientation of the MoS<sub>2</sub> film was determined through the FESEM, XRD, TEM, and Raman spectra. The MoS<sub>2</sub> films (horizontal, mixed, and

vertical MoS<sub>2</sub>) showed a p-type nature. The p-type behavior was verified through the positive increase in the resistance due to the exposure of oxidizing NO<sub>2</sub> gas. Interestingly, vertical aligned MoS<sub>2</sub> flakes faced the highest change in the sensor response to the NO<sub>2</sub> gas, which means that

the morphology of MoS<sub>2</sub> flakes crucially regulates the gas-sensing behavior. The reason is the presence of numerous active sites at the edges.

As we discussed in Sect. 3, the horizontal (basal plane) and vertical aligned MoS<sub>2</sub> flakes have different adsorption sites (H site, T<sub>S</sub> site, and T<sub>M</sub> site) for NO<sub>2</sub> molecules with different adsorption energy and charge transfer. Moreover, the edges of vertical aligned MoS<sub>2</sub> flakes have high catalytic properties in comparison with the basal plane, which enhanced the NO<sub>2</sub> reactivity of the edges. The vertical aligned MoS<sub>2</sub> flakes thus displayed the great potential to communicate with NO<sub>2</sub>. The adsorption of NO<sub>2</sub> on the basal plane MoS<sub>2</sub> and at the edges is shown in Fig. 12c.

Kumar et al. synthesized the horizontally aligned MoS<sub>2</sub> (HA-MoS<sub>2</sub>) and vertically aligned (VA-MoS<sub>2</sub>) by the CVD method [304]. The NO<sub>2</sub> sensing behavior for each structure was determined in the operating temperature range from RT to 150 °C. The VA-MoS<sub>2</sub> flakes showed better NO<sub>2</sub> sensing performance in all temperature range. Moreover, the VA MoS<sub>2</sub> film quickly detected 1 ppm NO<sub>2</sub> concentration. However, the sensor response for 1 ppm NO<sub>2</sub> concentration with HA MoS<sub>2</sub> flakes could not be achieved. These results revealed the high NO<sub>2</sub> detection ability of VA MoS<sub>2</sub> flakes even for the low concentration also. Another fascinating aspect of VA-MoS<sub>2</sub> is the sensor recovery after NO<sub>2</sub> exposure which didn't occur with the HA-MoS<sub>2</sub> flakes. The recovery of the VA and HA-MoS<sub>2</sub> flakes was substantially improved by operating devices at high temperatures but again at the expense of sensor response. Notably, the NO<sub>2</sub> selectivity of the VA-MoS<sub>2</sub> device was also high. The high sensor response of VA-MoS<sub>2</sub> flakes is due to the high adsorption sites and the higher number of charge transfer at the edges of the VA-MoS<sub>2</sub> flakes in comparison with HA-MoS<sub>2</sub> flakes.

Agrawal et al. synthesized a combination of vertical aligned MoS<sub>2</sub> flakes and in-plane MoS<sub>2</sub> flakes (mixed MoS<sub>2</sub> flakes) by a modified CVD technique. The surface morphology is shown in Fig. 12d. The black region is the in-plane MoS<sub>2</sub> flakes while the white region is the vertical MoS<sub>2</sub> flakes. The fabricated sensing system suggested the existence of the p-type nature of MoS<sub>2</sub> film. The resistance of the device was decreased with the exposure of oxidizing NO<sub>2</sub> gas which means there is a decrease in the electron concentration and simultaneously an increase in the hole concentrations. The transient response curve with NO<sub>2</sub> exposure at 125 °C is shown in Fig. 12e. The NO<sub>2</sub> detection at RT was also studied. However, full recovery could not be achieved.

The sensing mechanism of NO<sub>2</sub> interaction is based on the favorable adsorption sites available on the MoS<sub>2</sub> flakes, shown in Fig. 12f. MoS<sub>2</sub> has four adsorption sites as we discussed in Sect. 3, H site, B site, T<sub>M</sub>, and T<sub>S</sub> site. Yue et al. theoretically showed that the H site, T<sub>M</sub> site, and B site are the most favorable sites for the NO<sub>2</sub> adsorption. The maximum combination of these sites was synthesized to obtain the selective, highly responsive and recoverable NO<sub>2</sub> sensor.

Kumar et al. synthesized the MoS<sub>2</sub> nanowire through the controlled turbulent vapor flow, shown in Fig. 12g. The NO<sub>2</sub> sensing behavior of the n-type MoS<sub>2</sub> NWs was investigated at the RT, 60 °C, and 120 °C for NO<sub>2</sub> concentrations of 1, 2, 3, and 5 ppm, shown in Fig. 12h. The MoS<sub>2</sub> NWs showed a high sensor response with an incomplete recovery due to the strong bonding of NO<sub>2</sub> molecules with NWs. A moderate temperature of 60 °C helped the MoS<sub>2</sub> NWs to obtain a recovery. The MoS<sub>2</sub> NWs showed good response time (16 s) and recovery time (172 s) for the 5 ppm NO<sub>2</sub> concentration with sensor response 18% at 60 °C. The NO<sub>2</sub> sensing mechanism proposed in MoS<sub>2</sub> NWs is based on the physisorption and chemisorption of gas molecules, as shown in Fig. 12i. The humidity and environmental oxygen get adsorbed on the surface of the NWs and reduced the detection of the NO<sub>2</sub> gas molecule at the RT. However, at 60 °C, the humidity and adsorbed oxygen were removed and generated new active sites for the NO<sub>2</sub> adsorption. Hence, NO<sub>2</sub> detection was high at a moderate temperature. Moreover, the high temperature generates thermal energy which also helps in the recovery.

Yu et al. adopted the facile hydrothermal method and fabricated the edge-enriched flower-like MoS<sub>2</sub> spheres [33]. The diameter of the structure estimated through the SEM was 1–2 μm displayed in Fig. 13a. These nanospheres exhibited a large surface area with edge-enriched MoS<sub>2</sub> flakes. Also, the flakes were interconnected with each other and provided a quick path for the diffusion of gas molecules and charge transfer. The inset of Fig. 13a showed the high magnification FESEM image. These unique structures showed excellent sensor response, cyclability, and selectivity. The 50 ppm NO<sub>2</sub> concentration is discussed here. The device was operated at different operating temperatures from 100 to 250 °C, displayed in Fig. 13b. The highest sensor response for the 50 ppm NO<sub>2</sub> concentration was 78% at 150 °C. The resistance versus time profile is shown in the inset of Fig. 13c, confirming the p-type nature of MoS<sub>2</sub> due to a decrease in the resistance of the sensor device.



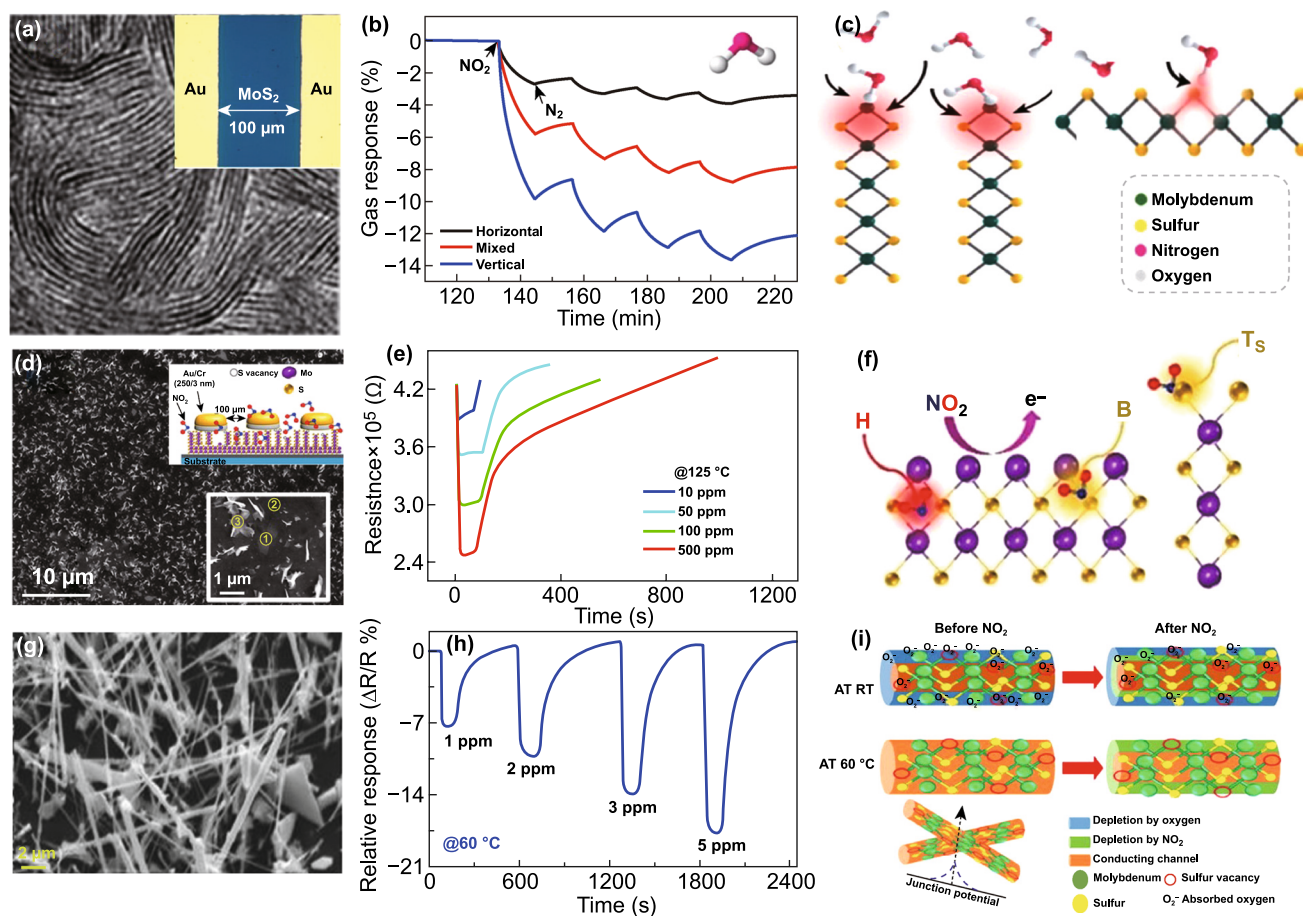


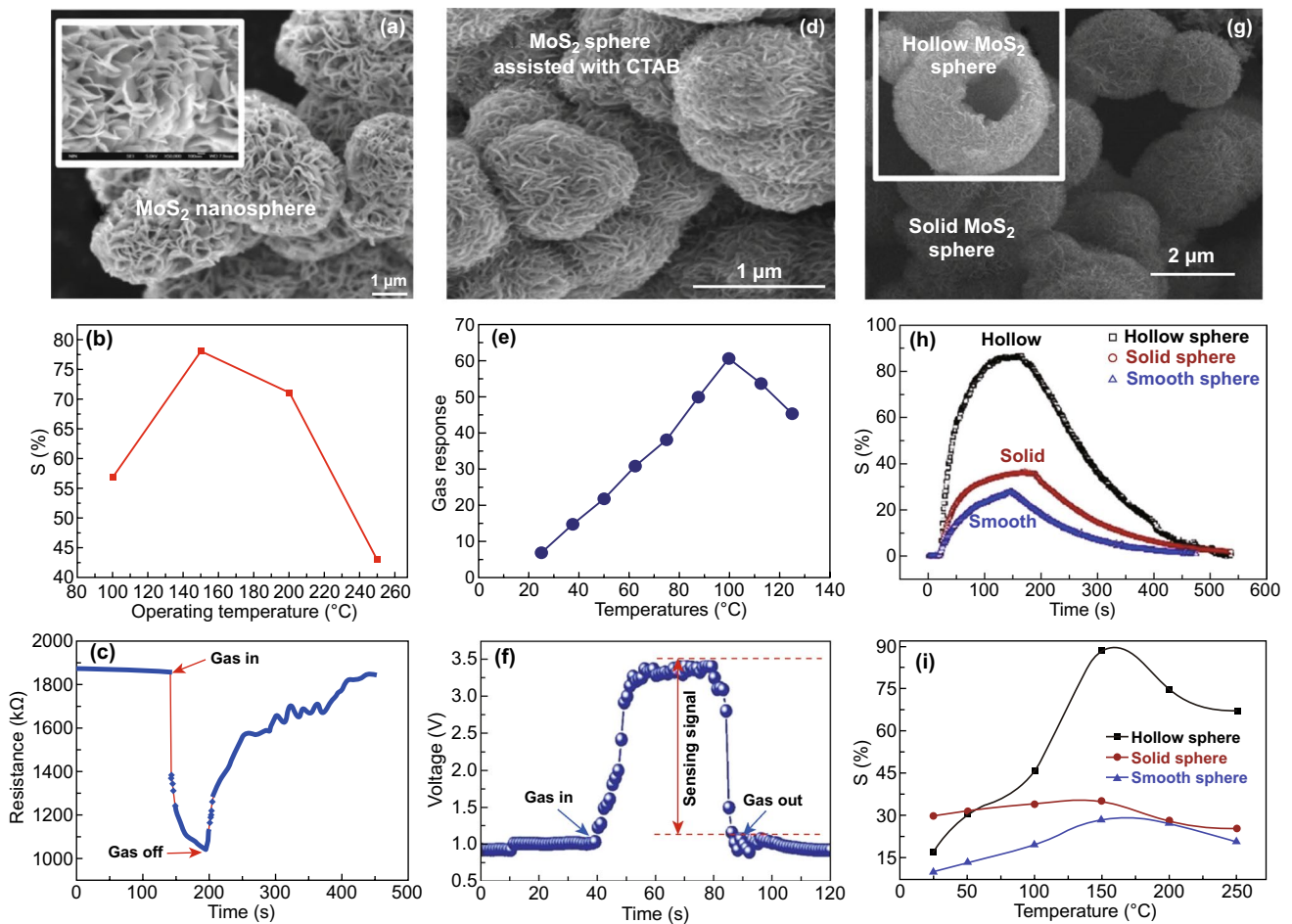
**Fig. 12** **a** TEM image of the vertically grown MoS<sub>2</sub>. **b** Response of various morphology MoS<sub>2</sub> flakes with NO<sub>2</sub> gas. **c** DFT calculated NO<sub>2</sub> adsorption profile on the edges and basal plane MoS<sub>2</sub>. Edges have high adsorption of MoS<sub>2</sub> flakes. Reproduced with permission from Ref. [35]. Copyright (2015) American Chemical Society. **d** FESEM image of mixed MoS<sub>2</sub> flakes and the device schematic. Inset showed the high-resolution image of MoS<sub>2</sub> flakes and the device schematic. **e** The response of mixed MoS<sub>2</sub> flakes with NO<sub>2</sub> gas at 125 °C. **f** Schematic of favorable adsorption sites on the MoS<sub>2</sub> flakes. Reproduced with permission from Ref. [120]. Copyright (2018) American Chemical Society. **g** FESEM image of the grown MoS<sub>2</sub> NWs. **h** Response of MoS<sub>2</sub> NWs with NO<sub>2</sub> exposure. **i** Proposed a mechanism of NO<sub>2</sub> adsorption on the MoS<sub>2</sub> NWs. Reproduced with permission from Ref. [214]. Copyright (2018) AIP Publishing

Zhang et al. proposed the controlled growth of 3D flower-like MoS<sub>2</sub> nanospheres assisted with cetyltrimethyl ammonium bromide (CTAB) [306]. CTAB played a crucial role in determining the morphology of the MoS<sub>2</sub> spheres. The average size of the synthesized nanospheres was 300 nm, displayed in Fig. 13d. This SEM revealed that these MoS<sub>2</sub> nanospheres were formed due to the bending of the randomly assembled MoS<sub>2</sub> sheets. These structures provide the path for the diffusion of the gas. The NO<sub>2</sub> sensing performance was studied in the operating temperature range from RT to 130 °C as shown in Fig. 13e. The highest reported sensor response was 60% observed for the 100 °C temperature. The MoS<sub>2</sub> nanospheres behaved as the n-type semiconductor.

The response and recovery time profile was 15 and 12 s for 50 ppm NO<sub>2</sub> at 100 °C shown in Fig. 13f.

Li et al. followed a new step and prepared the hollow, solid and smooth MoS<sub>2</sub> nanospheres by the hydrothermal methods [307]. The hydrothermal process reaction time was maintained at 2-h, 5-h, 18-h in the presence of polyvinyl pyrrolidone (PVP) to synthesize the various morphology MoS<sub>2</sub> flakes. The polystyrene template (PS) spheres are the platform for the nucleation of MoS<sub>2</sub> nanosheets. The SEM images of a fully prepared solid sphere and hollow spheres (inset) are shown in Fig. 13g. The 500 ppm NO<sub>2</sub> concentration is tested in the temperature range from 25 to 250 °C. Hollow spheres have shown the remarkably high sensor response with p-type nature, as shown in Fig. 13h,

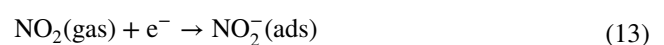


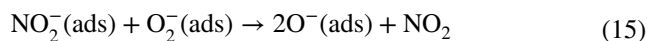
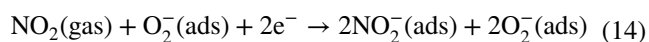


**Fig. 13** **a** FESEM image of the MoS<sub>2</sub> nanosphere. **b** Sensor response profile. **c** Transient resistance profile. Reproduced with permission from Ref. [33]. Copyright (2016) from Elsevier. **d** FESEM image of the CTAB-assisted MoS<sub>2</sub> sphere. **e** Gas response obtained at different temperature range. **f** Time response profile of NO<sub>2</sub> sensing. Reproduced with permission from Ref. [306]. Copyright (2018) from Elsevier. **g** FESEM image of solid MoS<sub>2</sub> sphere and hollow sphere. **h** Obtained sensor response for hollow, solid and smooth spheres. **i** Sensor response at different temperatures. The highest sensor response obtained for the hollow spheres. Reproduced with permission from Ref. [307]. Copyright (2019) from Elsevier

i. About 2.5-fold enhancement is observed in the hollow spheres compared to solid spheres observed.

Nanospheres improved NO<sub>2</sub> sensing due to the large surface area of the spheres. The sensing mechanism between the MoS<sub>2</sub> and NO<sub>2</sub> is based on the transfer of charge carrier concentration between them. The oxygen gas is adsorbed on the MoS<sub>2</sub> and introduced p-type doping in MoS<sub>2</sub>. When NO<sub>2</sub> gas exposed to MoS<sub>2</sub> spheres, the NO<sub>2</sub> accepts the electrons from MoS<sub>2</sub> and gets adsorbed as NO<sub>2</sub><sup>-</sup> on MoS<sub>2</sub>. Moreover, NO<sub>2</sub> also reacts with adsorbed O<sub>2</sub><sup>-</sup> and gets adsorbed as NO<sub>2</sub><sup>-</sup>. The possible reactions of adsorbed oxygen and with NO<sub>2</sub> are as follows [311]:





The above discussion clearly shows that different MoS<sub>2</sub> morphologies could boost the efficiency of gas sensors such as high sensor response, speed (response and recovery time), and selectivity. By choosing the different synthesis modes such as mechanical exfoliation, chemical exfoliation and CVD techniques, various MoS<sub>2</sub> morphologies can be synthesized ranging from in-plane MoS<sub>2</sub>, flower like MoS<sub>2</sub>, MoS<sub>2</sub> NWs, vertical MoS<sub>2</sub> flakes. Different MoS<sub>2</sub> morphologies like vertical aligned, nanowires, solid and hollow spheres provide the path for the diffusion of gas molecules into the nanostructures so that gas molecules interacts more efficiently. Each morphologies have its own advantage and contributes in improving gas sensing. The MoS<sub>2</sub> flowers have a high surface area and provide higher adsorption sites for gas molecule adsorption. The hollow microspheres offer a larger surface area (inner and outer surface for molecule adsorption) than the solid spheres. The one-dimensional MoS<sub>2</sub> NWs provides a combination of high surface area and active sites which will be further increased at moderate temperature.

### 5.3 Experimental Investigation of Metal Nanoparticle Doping of MoS<sub>2</sub>

In Sect. 4.4, we already discussed various theoretical reports where MoS<sub>2</sub> was doped with different metal atoms and the advantage of metal doping in MoS<sub>2</sub> predicted for NO<sub>2</sub> sensing. Here, we addressed the experimental picture of metal doping in MoS<sub>2</sub> for NO<sub>2</sub> sensing. MoS<sub>2</sub> has a large surface to volume ratio which provides unique opportunities to surface functionalization with metal nanoparticles (NPs) such as Ag, Au, Pt, Pd, and Rh and many more. The incorporation of MoS<sub>2</sub> surface with metal NPs could be an efficient way to improve the electronic, optical, energy storage and catalytic properties [312–316]. Undoubtedly, functionalizing the MoS<sub>2</sub> film with metal NPs could open up a new era in the gas-sensing applications.

He et al. used metal nanoparticles to fabricate NO<sub>2</sub> gas sensor based on MoS<sub>2</sub> flakes. The 4-nm-thick MoS<sub>2</sub> film was functionalized with Pt NPs [42]. The FESEM image of Pt-doped MoS<sub>2</sub> film is shown in Fig. 14a. The comparative

sensing performance of Pt NP-doped MoS<sub>2</sub>, rGO-MoS<sub>2</sub>, bare rGO, and bare MoS<sub>2</sub> is shown in Fig. 14b. The highest sensor response was achieved with Pt-doped MoS<sub>2</sub>. The modulated Schottky barrier height and spillover effect was responsible for enhanced NO<sub>2</sub> sensing of Pt-doped MoS<sub>2</sub> [317–319]. The Pt NPs formed nano-Schottky barriers at different places with MoS<sub>2</sub>. Pt extracted the electrons from the MoS<sub>2</sub> film and introduced p-type doping in MoS<sub>2</sub>. Moreover, due to the spillover effect, the catalytic reactivity of NO<sub>2</sub> molecules was also increased. Hence, the high sensor response with Pt-doped MoS<sub>2</sub> was achieved. The selectivity of the Pt-doped MoS<sub>2</sub> is shown in Fig. 14c.

Zhou et al. decorated Au nanoparticles on MoS<sub>2</sub> film and performed the NO<sub>2</sub> detection stability of the MoS<sub>2</sub>-Au composite [121]. The gold NPs of 50 nm diameter formed a strong bond with defects present on the edges. The Au NPs adsorbed at the edges can be seen in Fig. 14d. The NO<sub>2</sub> sensing ability in the dark and with the UV light exposure was also performed. The MoS<sub>2</sub> and MoS<sub>2</sub>-Au composites exhibited p-type nature. The full recovery with bare MoS<sub>2</sub> and Au decorated MoS<sub>2</sub> in the dark did not be achieve. However, when sensors were illuminated with UV light, fast response with a complete recovery and a three-time greater sensor response was achieved. Figure 14e shows all sensor responses. The band diagram between MoS<sub>2</sub> and gold NPs are shown in Fig. 14f. It revealed that electrons were transferred from gold NPs to MoS<sub>2</sub> due to the difference in work function. Au NPs increased MoS<sub>2</sub> activity and catalytic reactivity [321]. Under UV illumination, charge transfer between the MoS<sub>2</sub> and Au NPs rapidly increased and led to a fast recovery. The physisorbed O<sub>2</sub> and chemically adsorbed O<sub>2</sub> also produce a hole accumulation (HAL) layer in the MoS<sub>2</sub> surface similar to the metal oxides. Under NO<sub>2</sub> exposure, the width of the HAL layer increases and the resistance of MoS<sub>2</sub>-Au decreases.

Liu et al. doped MoS<sub>2</sub> with different ratios of W metal [320]. The W metal atoms were doped in the following ratio Mo: W: 1:0, 1:1, 1:2, and 1:3 and nominated as W<sub>0</sub>, W<sub>1</sub>, W<sub>2</sub>, and W<sub>3</sub>. The FESEM images of all the four samples are shown in Fig. 14g. The average crystallite size of the W metals was 52, 45, 29, and 32 nm. When NO<sub>2</sub> gas exposed to W-doped MoS<sub>2</sub> film, sample W<sub>2</sub> showed the highest sensor response among all with the fastest response and recovery time.

The undoped MoS<sub>2</sub> has the numerous number of defects. NO<sub>2</sub> gas molecules adsorbed on these defective sites through the chemisorption process which leads to strong adsorption

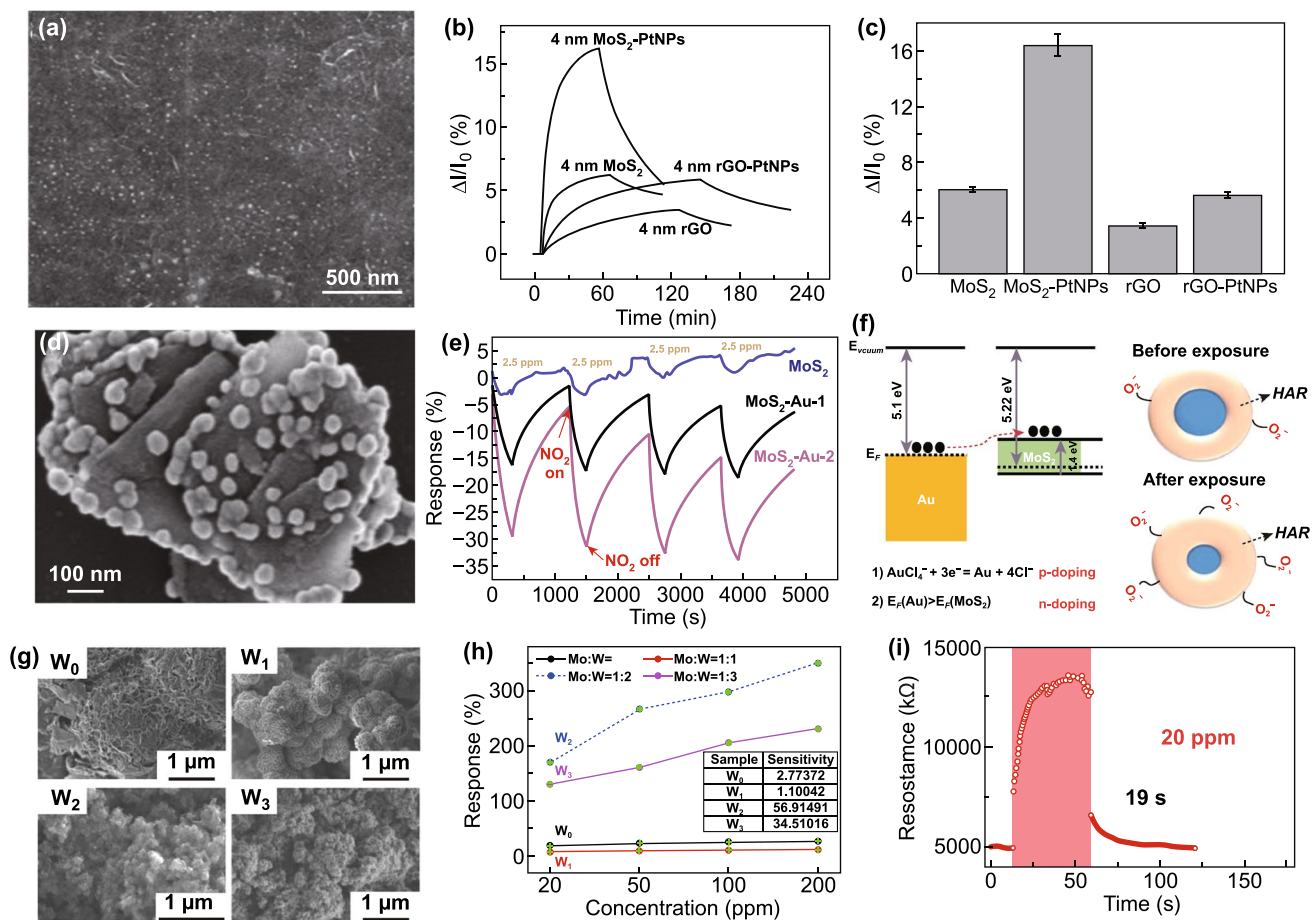


**Fig. 14** **a** Pt-doped 4-nm-thick MoS<sub>2</sub>. **b** Response of the Pt NP-doped MoS<sub>2</sub>, MoS<sub>2</sub>-rGo and of bare rGo. Pt NP-doped MoS<sub>2</sub> showed the highest response for the NO<sub>2</sub> adsorption. **c** Selectivity profile. Reproduced with permission from Ref. [42]. Copyright (2012) Wiley-VCH. **d** Au NP-doped MoS<sub>2</sub>. **e** Response profile with different concentrations of Au decorated MoS<sub>2</sub> and with UV light exposure. **f** Band alignment of MoS<sub>2</sub> and Au NPs and mechanism of NO<sub>2</sub> adsorption. Reproduced with permission from Ref. [121]. Copyright (2018) AIP Publishing. **g** Different concentration W metal loaded MoS<sub>2</sub>. **h** Sensor response profiles of W loaded MoS<sub>2</sub>. **i** Response and recovery profile for 20 ppm NO<sub>2</sub> exposure. Reproduced with permission from Ref. [320]. Copyright (2020) Elsevier

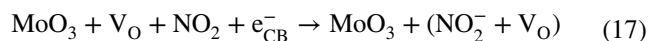
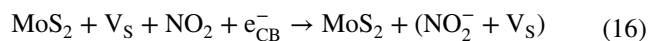
between the MoS<sub>2</sub> and NO<sub>2</sub> molecules. Hence, NO<sub>2</sub> desorption is difficult from MoS<sub>2</sub>, which leads to the sluggish recovery. Metal doping is an efficient way to improve the sensing performance. Here, authors doped MoS<sub>2</sub> with atoms of W metal which have close radii to Mo atoms. There are no additional defects produced in MoS<sub>2</sub> due to comparable radii of the Mo and W atoms. Thus the defects in MoS<sub>2</sub> are significantly suppressed with W metals, and NO<sub>2</sub> sensing performance is enhanced. The highest sensor response achieved was 56.91% in W<sub>2</sub> sample, can be seen from Fig. 14h. Interestingly, the response and recovery were the fastest for the sample W<sub>2</sub>. The observed response and recovery time were 24 and 19 s, shown in Fig. 14i.

It is clear from the proposed discussion that metal NPs doping is an efficient way to enhance the gas-sensing performances of MoS<sub>2</sub> gas sensors. Metal (NPs) doping not only improved the chemical and catalytic reactivity in MoS<sub>2</sub> but also affected the electronic properties. Metal NPs formed nano-Schottky barriers in different regions of the MoS<sub>2</sub>, which greatly increases the transfer of charges in MoS<sub>2</sub>. Thus, metal (NPs) doping also helps in full recovery of the MoS<sub>2</sub>-based NO<sub>2</sub> sensors with improved sensor response, selectivity and long term stability. In addition, illuminating the metal (NPs)-doped MoS<sub>2</sub> sensors could improve the sensing characteristics. However, some more rigorous efforts are still needed to completely explore the effect of light illumination on metal-doped MoS<sub>2</sub>.

#### 5.4 Vacancy-Driven NO<sub>2</sub> Sensors

Vacancies in MoS<sub>2</sub> played a key role and contributed to increased efficiency in gas sensing. Long et al. synthesized 3D MoS<sub>2</sub> aerogel by the thermal decomposition technique [24]. A two-step sulfur treatment method was employed to fabricate the NO<sub>2</sub> gas sensor. Figure 15a and its inset shows surface morphology without treatment and with treatment. The MoS<sub>2</sub> aerogel became more porous after the sulfur treatment. The MoS<sub>2</sub> aerogel showed a high sensor response to NO<sub>2</sub> gas at RT, and a rapid response and full recovery with the sulfur treatment device. The as prepared MoS<sub>2</sub> aerogels showed a good sensor response. However, due to the strong bonding of NO<sub>2</sub> with MoS<sub>2</sub>, it suffered from slow response and recovery. The sulfur treatment in the H<sub>2</sub> ambient produces new sulfur vacancies. The elevated temperature generally removes the S atoms from MoS<sub>2</sub> and increases the vacancies in sensing film. Figure 15b, c displays the resistance versus time profile for 50 ppb NO<sub>2</sub> concentration at 200 °C. Furthermore, the response and recovery time were further improved with the temperature attributed to the fast desorption of NO<sub>2</sub> molecule at high temperature. Donarelli et al. reported the formation of n and p-type MoS<sub>2</sub> flakes annealed at 250 and 150 °C [31]. The SEM image of MoS<sub>2</sub> flakes deposited onto the Si<sub>3</sub>N<sub>4</sub> with Pt electrodes is shown in Fig. 15d. Figure 15e, f shows the relative response of MoS<sub>2</sub> flakes to 150 and 250 °C. With the electron acceptor nature of NO<sub>2</sub>, the resistance of the MoS<sub>2</sub> device annealed at 150 °C was decreased while resistance was increased at 250 °C. The device annealed at 150 °C did not respond at RT but a high sensor response was obtained at RT when the device was annealed at 250 °C. Moreover, the sensor showed better sensing performances with 250 °C annealed devices. The n-type and p-type behavior of different devices can be understood in terms of used synthesis method. The NMP was used for the synthesis of MoS<sub>2</sub>. The NMP intercalate in between the MoS<sub>2</sub> layers at 150 °C. The NMP degraded and introduced the N atom at the S vacancy sites. N atom is an electron acceptor and responsible for p-type behavior [322]. In addition, MoS<sub>2</sub> surface was partially reduced to MoO<sub>3</sub> layers and more S and O vacancies were created when MoS<sub>2</sub> flakes are annealed at 250 °C [323]. The interaction between NO<sub>2</sub> sensing and n-type MoS<sub>2</sub> is crucially dependent on the

S and O vacancies [324]. Equations 16 and 17 demonstrate the possible reaction mechanism between p-type MoS<sub>2</sub> and NO<sub>2</sub>.



where (NO<sub>2</sub><sup>-</sup> + V<sub>O</sub>) and (NO<sub>2</sub> + e<sup>-</sup>) are the adsorbed NO<sub>2</sub> on the oxygen and S vacancies. e<sub>CB</sub><sup>-</sup> is the electron in the conduction band. Hence, NO<sub>2</sub> interacts with e<sub>CB</sub><sup>-</sup> and leads to a decrease in the conduction band electrons with an increase in the resistance of the electrons.

Kumar et al. annealed the vertical aligned MoS<sub>2</sub> flakes at 600 °C to obtain vacancy-enriched MoS<sub>2</sub> flakes. The S atom has low binding energy of (2.12 eV). Hence annealing the MoS<sub>2</sub> flakes at higher temperatures could be useful to create the S vacancies. Further, the MoS<sub>2</sub> flakes were decorated with the crumpled rGO. The FESEM image of vertical aligned MoS<sub>2</sub> flakes is shown in Fig. 15g and rGO decorated flakes showed in the inset of Fig. 15g. The dynamic sensing response of pristine MoS<sub>2</sub>, Sv-MoS<sub>2</sub>, rGO-MoS<sub>2</sub>, and rGO/Sv-MoS<sub>2</sub> investigated at 50 °C with 50 ppm NO<sub>2</sub> concentration and showed in Fig. 15h.

The NO<sub>2</sub> sensor response was 27%, 34%, and 39% for pristine MoS<sub>2</sub>, Sv-MoS<sub>2</sub>, and rGO-MoS<sub>2</sub>, respectively. However, the full recovery and high sensor response of 72% was achieved with rGO/Sv-MoS<sub>2</sub>. The oxygen present in rGO formed strong bonds with S vacancies of MoS<sub>2</sub> and attracted 0.997 electrons from MoS<sub>2</sub>/rGO. Therefore, there was sufficient transfer of charge between the MoS<sub>2</sub> and rGO which modified the nature of MoS<sub>2</sub> from n-type to p-type. S vacancies specifically play a major role in the charge transfer between MoS<sub>2</sub> and rGO. When NO<sub>2</sub> molecules were exposed to rGO/Sv-MoS<sub>2</sub>, electrons were depleted from rGO to MoS<sub>2</sub> and the Fermi level of rGO shifted towards the valence band. Hence, a large number of electrons transferred from the MoS<sub>2</sub> to rGO. Also, further NO<sub>2</sub> exposure enhances the holes in MoS<sub>2</sub> and therefore MoS<sub>2</sub> behaves as a p-type. The schematic of the proposed mechanism is shown in Fig. 15i.

The role of vacancies in gas sensing has been cleared from the above discussion. The vacancies can change the electronic, optical, and chemical activity of the MoS<sub>2</sub>. The gas molecules interaction at these vacancies sites



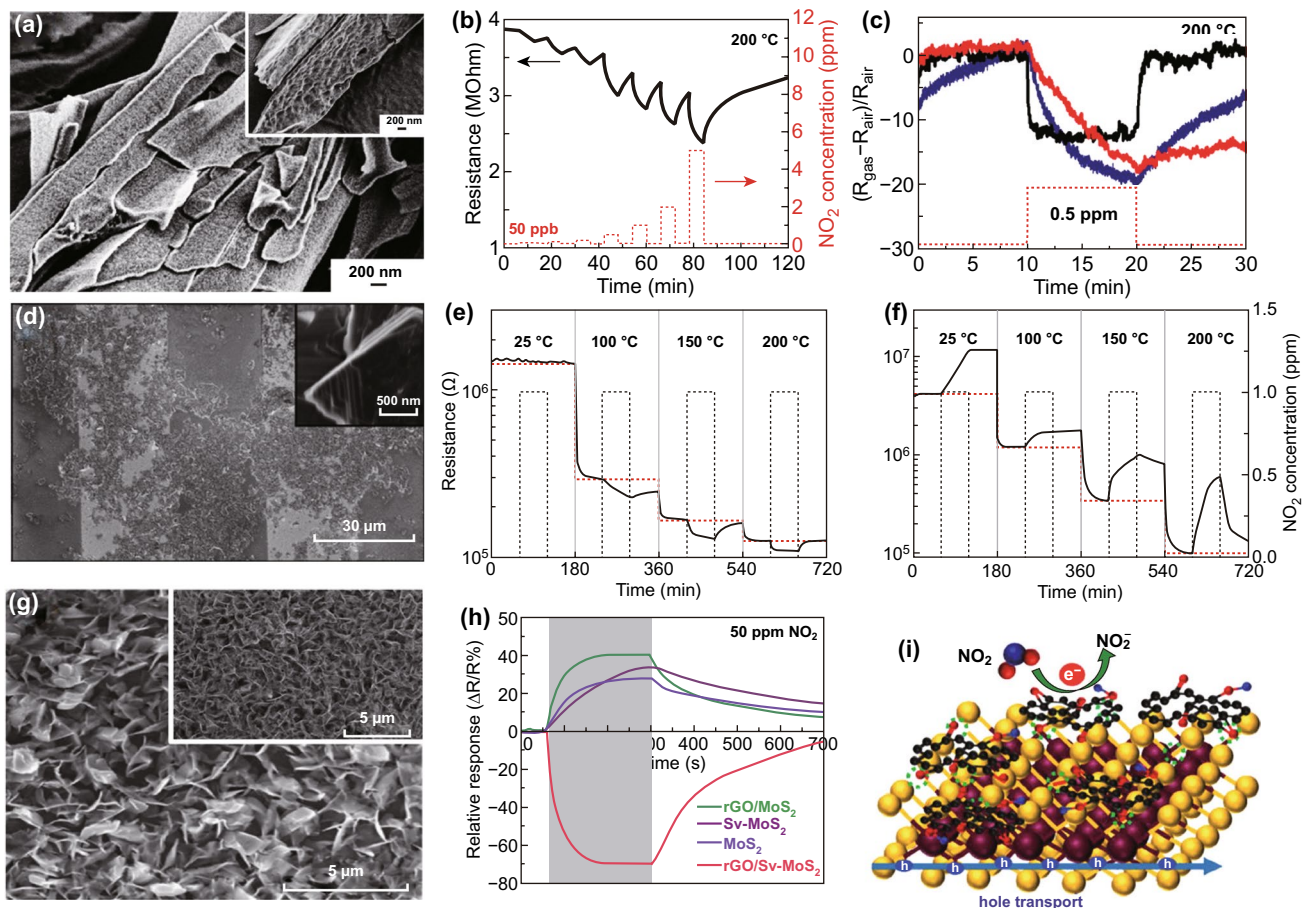


**Fig. 15** **a** FESEM image of 3D MoS<sub>2</sub> aerogels. **b** Response of MoS<sub>2</sub> aerogel with NO<sub>2</sub> at 200 °C. **c** Device response to NO<sub>2</sub> at different temperatures. Reproduced with permission from Ref. [24]. Copyright (2017) Wiley-VCH. **d** FESEM image of MoS<sub>2</sub> flakes distributed on the Pt electrodes. NO<sub>2</sub> response of the MoS<sub>2</sub> flakes: **e** annealed at 150 °C showed p-type behavior; **f** annealed at 250 °C showed n-type behavior. Reproduced with permission from Ref. [31]. Copyright (2015) Elsevier. **g** FESEM image of sulfur vacancy-enriched MoS<sub>2</sub> flakes. **h** Response of 50 ppm NO<sub>2</sub> with MoS<sub>2</sub>, rGO/MoS<sub>2</sub>, Sv-MoS<sub>2</sub>, rGO/Sv-MoS<sub>2</sub>. rGO deposited Sv-MoS<sub>2</sub> shown p-type behavior. **i** Mechanism of NO<sub>2</sub> interaction with rGO deposited Sv-MoS<sub>2</sub>. Reproduced with permission from Ref. [310]. Copyright (2019) IEEE

is governed by the chemisorption process. Thus, the vacancy-enriched MoS<sub>2</sub> has enhanced NO<sub>2</sub> sensing performance in terms of sensor response and speed. The vacancies can be tailored through morphology and these vacancies work as the active sites to enhance the gas molecules adsorption. Moreover, the functionalization of vacancies with substitutional atoms can change their electronic nature from n-type to p-type such as N, B, O, and Ni. Another important aspect on the vacancies is the effect of the high temperature annealing of the MoS<sub>2</sub> film. The high temperature ~ 500–600 °C annealing can generate the more vacancies in MoS<sub>2</sub> which will be helpful in designing the high-performance NO<sub>2</sub> sensors based on MoS<sub>2</sub>.

### 5.5 Light-Assisted NO<sub>2</sub> Sensors

The MoS<sub>2</sub> has shown high adsorption energy for NO<sub>2</sub> molecules at RT. NO<sub>2</sub> is adsorbed through the chemisorption and physisorption process on the MoS<sub>2</sub> surface. This high adsorption energy causes difficulty in the full recovery of MoS<sub>2</sub>. MoS<sub>2</sub> requires additional efforts to remove adsorbed NO<sub>2</sub> molecules for complete recovery at RT. The one possible solution is to isolate the device temporarily from the toxic environment for complete recovery at high temperatures. However, to develop real time NO<sub>2</sub> sensor, this method is not feasible. Moreover, it demands necessary engineering efforts which will raise

the cost of the sensor and time consuming process. In order to accelerate the desorption rate of  $\text{NO}_2$  molecules from the  $\text{MoS}_2$  surface, researchers used thermal energy to achieve the fast and full recovery of  $\text{MoS}_2$ -based  $\text{NO}_2$  sensors. However, there are certain disadvantages of running sensors at elevated temperatures. The speedy recovery is achieved at the cost of the lower sensor response. In addition, it also deteriorates the sensor's long term stability, which raises the complexity and cost of manufacturing sensing devices. Thus, it is not an effective way to run the  $\text{NO}_2$  sensor at high temperatures. The light illumination could be an effective way to enhance the sensing performance of  $\text{MoS}_2$ -based sensors while keeping the sensor at RT. The light illumination greatly influences the adsorption, desorption and the adsorption energy. Here, we will focus on the impact of light illumination on the  $\text{NO}_2$  sensing in this section. We have divided the light illumination into three parts UV light illumination, visible light illumination and finally in the NIR illumination.

### 5.5.1 Ultraviolet-Activated $\text{NO}_2$ Sensor

Kumar et al. studied the role of the UV light in developing the RT  $\text{NO}_2$  sensor [119]. The CVD grown in-plane  $\text{MoS}_2$  flakes was utilized for  $\text{NO}_2$  gas sensing. The device schematic is shown in Fig. 16a. The  $\text{NO}_2$  sensing was carried out at RT, 100 °C, and with UV illumination at RT (Fig. 16b, c). Among them, the highest sensor response with full recovery was found with the UV light illumination at RT (Fig. 16c). The sensor did not recover fully at RT without UV lighting. The sensor response under tunable UV light intensities from 0.3 to 2  $\text{mW cm}^{-2}$  was tested. The sensor response was lowest at 2  $\text{mW cm}^{-2}$  and the highest sensor response was recorded at 1.2  $\text{mW cm}^{-2}$ . The high light intensity allows  $\text{NO}_2$  molecules to desorb easily than their adsorption. Thus,  $\text{NO}_2$  sensor response was lowest at a high light intensity.

Agrawal et al. utilized mixed  $\text{MoS}_2$  flakes for  $\text{NO}_2$  sensing [120]. The  $\text{NO}_2$  sensing at RT, 125 °C, and with UV light illumination at RT was explored. The highest sensor response, fast and full recovery were obtained with UV light illumination at RT. The schematic of the mixed  $\text{MoS}_2$  flakes with possible  $\text{NO}_2$  adsorption sites, the response of mixed  $\text{MoS}_2$  flakes and comparative sensor response under UV light is shown in Fig. 16e–g. The gas-sensing mechanism for

both the studies is discussed as follows. The sensing behavior of  $\text{MoS}_2$  flakes is highly dependent on the surface morphology, the number of active sites and notably on the defects in the form of vacancies. The environmental impurities such as oxygen and humidity get adsorbed on these defects. The adsorbed oxygen takes the electrons from the  $\text{MoS}_2$  flakes and introduces p-type doping. At RT without UV light illumination, a high amount of oxygen is adsorbed on the  $\text{MoS}_2$  flakes and a large number of electrons are extracted from  $\text{MoS}_2$  flakes. Owing to the electron acceptor,  $\text{NO}_2$  withdrawn electrons from the  $\text{MoS}_2$ . However, the desorption rate is not fast due to the strong bonding of  $\text{NO}_2$  and led to incomplete recovery. Moreover, when thermal energy is added in  $\text{MoS}_2$  from external sources, some oxygen in the  $\text{MoS}_2$  flake is desorbed and more fresh active sites in the form of defects are formed. In addition, thermal energy speeds up the desorption process that causes the sensor response to decrease. The desorption rate of oxygen molecules was highest under UV illumination. UV light illumination generates new electron and hole pairs. The photogenerated holes react with adsorbed oxygen and adsorbed oxygen gets released from the  $\text{MoS}_2$  surface. The UV light illumination creates more fresh active sites. On these fresh active sites, the  $\text{NO}_2$  molecules get adsorbed and increase sensor response. Moreover, when  $\text{NO}_2$  gas turned off, the adsorbed oxygen reacted with the photogenerated electrons and desorbed easily from the  $\text{MoS}_2$  surface. The recovery rate therefore improves under UV lighting. The proposed sensing mechanism for both the reports is shown in Fig. 16d, h.

Zhou et al. fabricated an ultrasensitive, fast UV assisted, RT  $\text{NO}_2$  sensor [325]. The detection limit of the fabricated  $\text{MoS}_2/\text{ZnO}$   $\text{NO}_2$  was very low (50 ppb). The n-type  $\text{ZnO}$  NWs were synthesized using the hydrothermal process, while the ultrasonic method was used to synthesize the p-type  $\text{MoS}_2$ . Two types of sensors were fabricated with different composites amount of  $\text{MoS}_2$  and  $\text{ZnO}$  such as  $\text{MoS}_2/\text{ZnO}$  (0.5:0.25) and  $\text{MoS}_2/\text{ZnO}$  (0.25:0.25). The device schematic is shown in Fig. 16i. The bare  $\text{MoS}_2$  device did not show any  $\text{NO}_2$  sensing capability which may be due to the low conductivity of the flakes. However, both devices exhibited significant sensor response under UV exposure. Moreover, devices with equal  $\text{MoS}_2$  and  $\text{ZnO}$  composites showed better  $\text{NO}_2$  sensing performance under UV light illumination, can be seen from Fig. 16j. The gas-sensing mechanism was proposed based on the band alignment as shown in Fig. 16k, l.  $\text{MoS}_2$  has p-type nature and electrons transferred from the  $\text{MoS}_2$  conduction

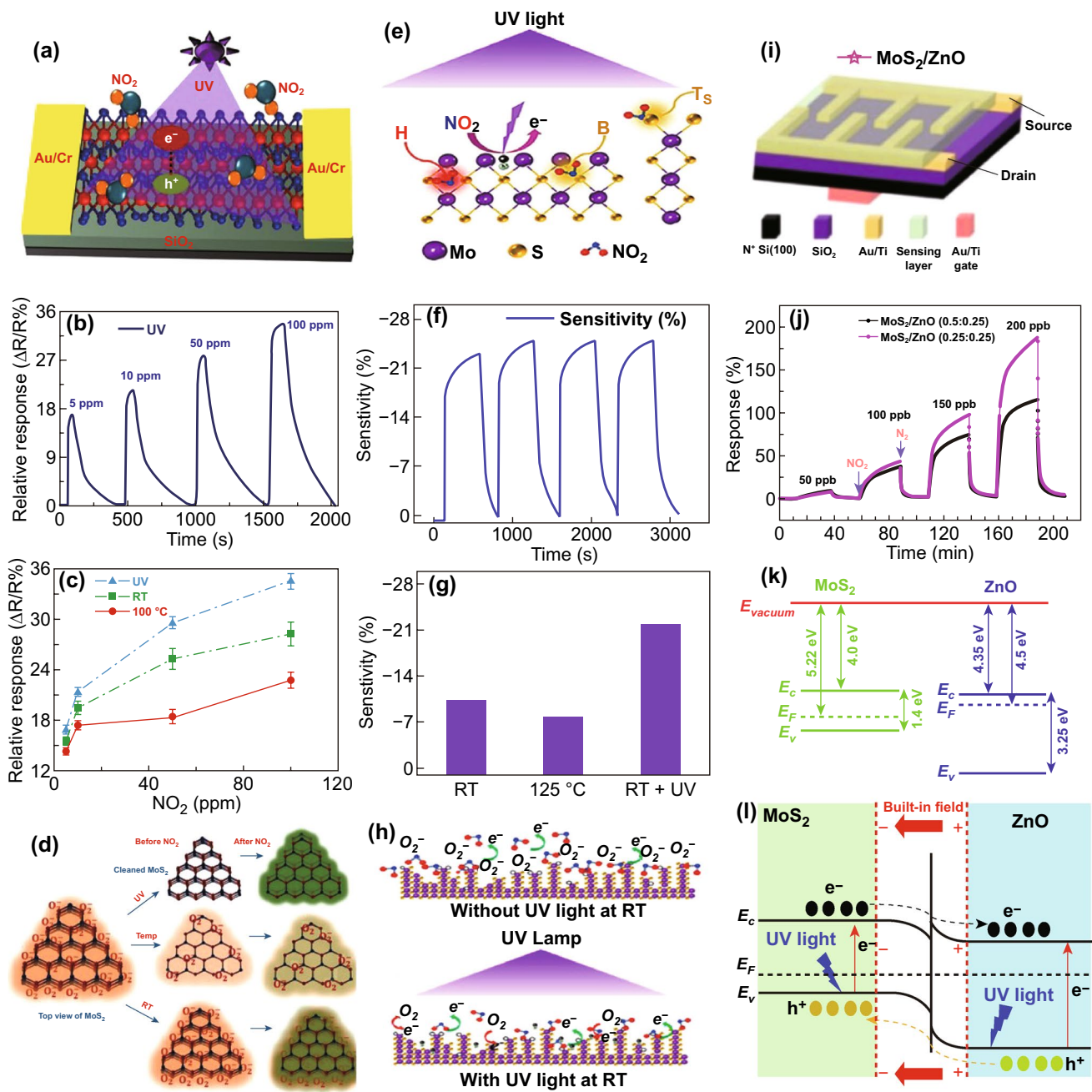


**Fig. 16** **a** Schematic view of the proposed device under UV illumination. **b**  $\text{NO}_2$  response under UV light, **c** comparative performance under UV at RT, RT, and at higher temperature. **d** Working mechanism. Reproduced with permission from Ref. [119]. Copyright (2017) American Chemical Society. **e** Proposed working mechanism under UV light. **f** Sensor response profile under UV light. **g** Comparative  $\text{NO}_2$  sensing bar profile. **h** Working mechanism under UV illumination. Reproduced with permission from Ref. [120]. Copyright (2018) American Chemical Society. **i** Device schematic for  $\text{NO}_2$  sensing. **j**  $\text{NO}_2$  response with different concentration  $\text{MoS}_2/\text{ZnO}$  composite device. **k, l** Band alignment before the junction and after the formation of contact with  $\text{NO}_2$  exposure. Reproduced with permission from Ref. [325]. Copyright (2018) The Royal Society of Chemistry

band to the ZnO conduction band under UV illumination. Thus, the photogenerated charge carriers were segregated efficiently and prevent further recombination.

### 5.5.2 Visible Light-assisted $\text{NO}_2$ Sensors

The UV light illumination has evidently proved its significance and its critical role in achieving the fast recoverable  $\text{NO}_2$  sensors for the RT. However, the UV illumination has certain disadvantages as well. Practically, the use of UV light is still a vivid challenge. UV radiation is harmful to human wellbeing. World cancer research agency identified that the continuous use of UV radiation is harmful to humans. Continuous exposure of UV light can cause premature aging of the skin in terms of wrinkles, leathery skin and solar elastosis. UV radiation is therefore particularly harmful to human vision. UV radiation can easily damage the corona of the eyes. The UV rays can significantly affect the immune system. Furthermore, the cost of UV lamps is

very high. Therefore, it is essential to study the role of visible light on the gas sensing.

Late et al. studied the role of light exposure in  $\text{NO}_2$  gas sensing. Traditionally, the UV light is the most adopted light source for sensing measurements. However, continuous UV light exposure may degrade the sensing performance of the device and harmful to humans [327]. Thus, the authors used safe green light of 532 nm to perform the  $\text{NO}_2$  gas-sensing measurements.

The irradiated green light has tunable power densities from 4 to 50  $\text{mW cm}^{-2}$ . The highest resistance change has been observed with higher incident power, which is attributed to the higher number of photogenerated electrons and holes with higher incident light power. The change in the resistance with incident light power density is shown in Fig. 17a. With light illumination, the desorption rate of  $\text{NO}_2$  gas molecule is relatively high in comparison with the adsorption rate. Moreover, a small fraction of electrons reacts with  $\text{NO}_2$  gas due to the high power density of incident light. Therefore, the  $\text{NO}_2$  sensor response is reduced

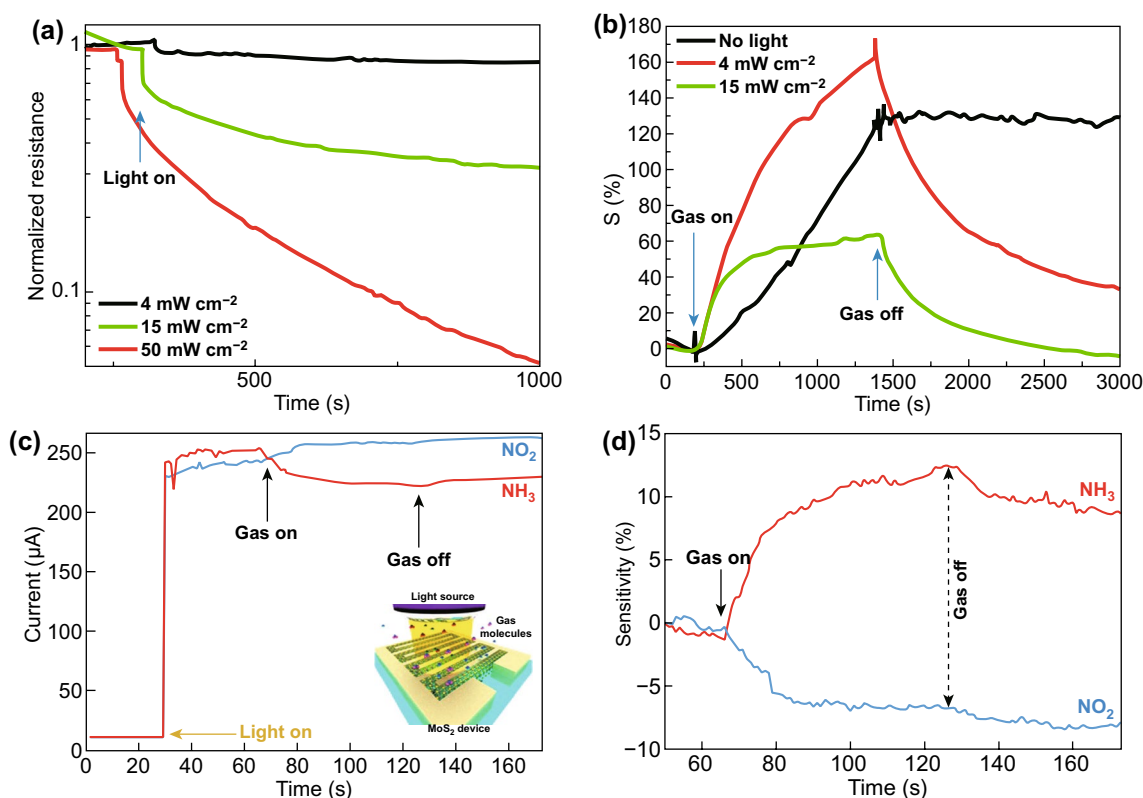


**Fig. 17** a Effect of power density on the resistance. b Effect of power density on the  $\text{NO}_2$  response. Reproduced with permission from Ref. [17]. Copyright (2013) American Chemical Society. c Detection of the  $\text{NO}_2$  and  $\text{NH}_3$  exposure with 650 nm wavelength exposure. d Change in the sensor response under light illumination. Reproduced with permission from Ref. [326]. Copyright (2015) American Chemical Society



with a high incident power density as shown in Fig. 17b. The full recovery is obtained with green light illumination. Similarly, Cho et al. synthesized atomic layered MoS<sub>2</sub> and illuminated device with 650 nm red light [326]. The schematic of the device is shown in the inset of Fig. 17c. The photogenerated current increased rapidly when the red light was turned on after 30 s. NO<sub>2</sub> gas was turned on after 60 s. The current increased further implying the p-type characteristic of the MoS<sub>2</sub> flakes. The calculated sensor response with red light illumination is shown in Fig. 17d.

### 5.5.3 Near-Infrared (NIR)-Assisted NO<sub>2</sub> Sensor

Xia et al. recently used NIR light to develop sensitive fast NO<sub>2</sub> sensor with sulfur vacancy-enriched MoS<sub>2</sub> flakes [123]. The conventional MoS<sub>2</sub> (C-MoS<sub>2</sub>) and sulfur vacancy-enriched MoS<sub>2</sub> (S-MoS<sub>2</sub>) flakes were synthesized by the traditional microwave-hydrothermal method. The sulfur vacancies were investigated by the electron paramagnetic resonance (EPR), XPS, and XRD. The schematic structure

of C-MoS<sub>2</sub> and Sv-MoS<sub>2</sub> is shown in Fig. 18a. Further, the absorption spectroscopy has been performed for both the C-MoS<sub>2</sub> and Sv-MoS<sub>2</sub> which revealed the high absorption of NIR light by Sv-MoS<sub>2</sub>. The NO<sub>2</sub> sensing ability of the C-MoS<sub>2</sub> and Sv-MoS<sub>2</sub> is shown in Fig. 18b, c. Interestingly, the observed sensor response with Sv-MoS<sub>2</sub> was high in the presence and in the absence of NIR light. The presence of S vacancies modulated the band structure of MoS<sub>2</sub> flakes and generated three additional localized states in MoS<sub>2</sub> bandgap, i.e., two unoccupied states at 0.63 eV below the conduction band and one shallow state near the valence band (Fig. 18d, e). Both additional states narrow down the MoS<sub>2</sub> bandgap in contrast with the pure MoS<sub>2</sub> bandgap. Hence, Sv-MoS<sub>2</sub> showed a high NIR photoresponse.

The S vacancies quickly reduced the Gibbs free energy of adsorbed gas molecules and increased the electron transfer rate from MoS<sub>2</sub> to NO<sub>2</sub>. The Sv-MoS<sub>2</sub>, therefore provides enhanced sensing efficiency not only in the dark but also with NIR lighting. The gas sensing performances of light driven MoS<sub>2</sub>-based NO<sub>2</sub> sensors summarized in Table 4.

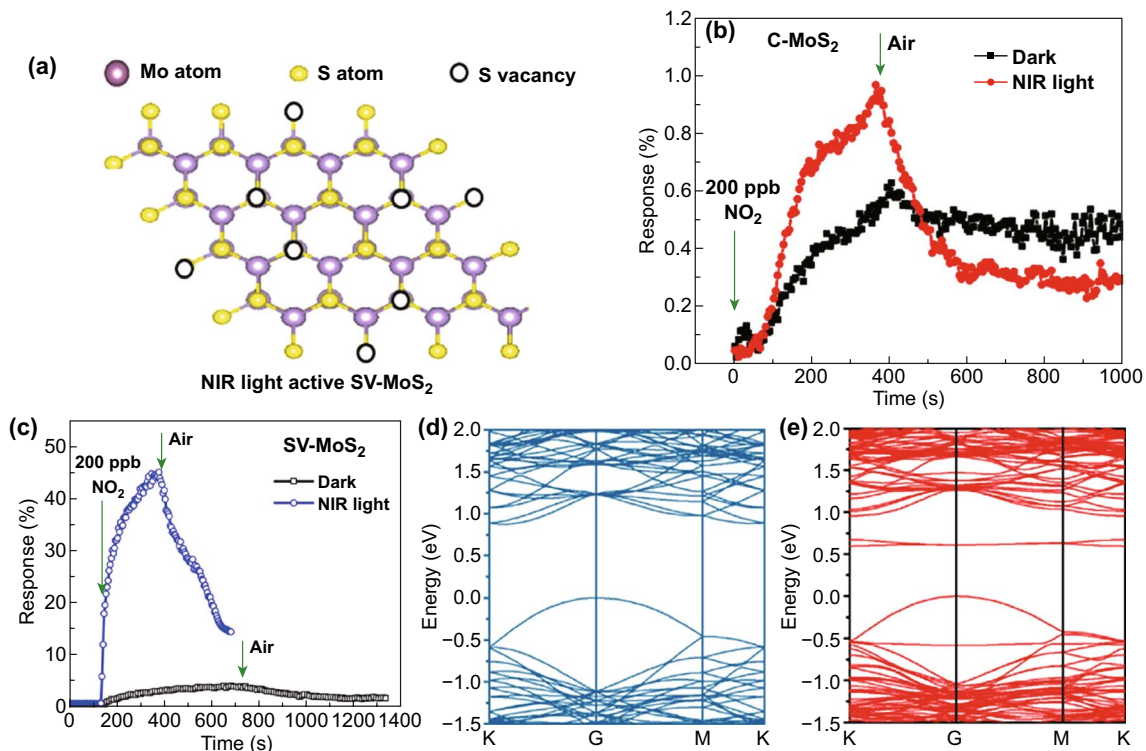


**Fig. 18** a Schematic of NIR light-activated sulfur vacancy-enriched MoS<sub>2</sub> (Sv-MoS<sub>2</sub>). b Response of C-MoS<sub>2</sub> in dark and NIR with NO<sub>2</sub> exposure. c Response of Sv-MoS<sub>2</sub> in dark and NIR with NO<sub>2</sub> exposure. Band structure of d C-MoS<sub>2</sub> (blue) and e Sv-MoS<sub>2</sub> (red). Reproduced with permission from Ref. [123]. Copyright (2019) American Chemical Society. (Color figure online)

**Table 4** Summary of the light-driven NO<sub>2</sub> sensor of MoS<sub>2</sub>

Sensing film	Method	Electrodes	Def.	Device	Conc. (ppm)	$P/\lambda$ (mW/cm <sup>2</sup> /nm)	T (°C)	S (%)	Res time	Rec. time	References
Multi MoS <sub>2</sub>	CVD	Au/Cr	$\frac{(R_{gas}-R_{air})}{R_{air}}$	Resistor	100	1.2/365	RT+UV	35.16	29	350	[119]
Mix MoS <sub>2</sub>	CVD	Au/Cr	$\frac{(R_{gas}-R_{air})}{R_{air}}$	Resistor	10	3/365	RT+UV	21.78	6.1	146.5	[120]
MoS <sub>2</sub> /ZnO	Hydrothermal	Au/Ti	$\frac{(R_{gas}-R_{air})}{R_{air}}$	FET	50	1/365	RT+UV	188	60	60	[325]
MoS <sub>2</sub>	CVD	Pt	$\frac{R_{gas}}{R_{air}}$	Resistor	10	0.29/365	RT+UV	25.3	-	63.9	[328]
ZnO/MoS <sub>2</sub>	Ultrasonication	ITO	$\frac{(R_{gas}-R_{air})}{R_{air}}$	Resistor	10	360	RT+UV	293	258	72	[329]
1L MoS <sub>2</sub>	CVD	Cr/Pd/Au	$\frac{(R_{gas}-R_{air})}{R_{air}}$	Resistor	0.4	4/625	RT+625	670	16	65	[122]

These studies revealed that under light illumination gas-sensing performance of MoS<sub>2</sub> is critically affected. Light illumination is a promising approach to enhance the sensor response of MoS<sub>2</sub> in comparison with providing thermal activation. The electrons and holes pairs generated due to light illumination provide a sufficient number of charge carriers to increase the gas-sensing response of the MoS<sub>2</sub> sensors. Traditionally, UV light is the most verified technique to enhance the sensor response of gas sensors and also with MoS<sub>2</sub>. UV illumination provides better treatment of adsorbed ambient oxygen than thermal energy. UV illumination significantly cleans environmental oxygen from the MoS<sub>2</sub> surface without any structural loss than the thermal energy. But, long term exposure of UV is not good for living cells.

Furthermore, the integration of MoS<sub>2</sub> with NO<sub>2</sub> sensitive materials could be helpful in developing ultrasensitive NO<sub>2</sub> sensors at RT with light. MoS<sub>2</sub>-Heterojunctions rapidly separate the generated electron and holes pairs due to light and NO<sub>2</sub> exposure, which will improve the gas-sensing performance.

MoS<sub>2</sub> has a high absorption coefficient in the visible region of spectrum of spectrum. Thus, a large number of electrons generate in MoS<sub>2</sub> in visible region and NO<sub>2</sub> has high number of electron available to withdraw from MoS<sub>2</sub> surface. However, with UV light, the number of generated electrons holes pairs are not so high. So, utilizing the visible spectra in gas sensing could be a better and safe approach to fabricate the high-performance gas sensors. To further utilize the NIR spectra, some engineering efforts may be needed to enhance the absorption of MoS<sub>2</sub> in NIR. Use of NIR light sources will reduce the high cost of the sensors in comparison with UV and visible light sources.

## 6 MoS<sub>2</sub>-Heterostructure NO<sub>2</sub> Sensor

Advancement in MoS<sub>2</sub> gas sensors can be achieved by forming the heterostructures. The production of single or few layer MoS<sub>2</sub> is considered not an easy approach and limits the high throughput of gas sensor. Ambiguity in the gas-sensing mechanism of MoS<sub>2</sub> with NO<sub>2</sub> gas has also been a topic of debate. Integration of MoS<sub>2</sub> with other materials such as graphene derivative, metal oxides and carbon materials create heterostructure at the junction. The formation of heterostructure affects the gas-sensing properties in both positive and

negative aspects. Forming a heterojunction can improve the intrinsic electronic properties of MoS<sub>2</sub> that tends to improve the sensor response and recovery time. However, the integration of heterostructure also puts a bit of complexity in the gas-sensing mechanism. Here, in this section, we tend to summarize the advancement in the material of different dimensions with MoS<sub>2</sub> equipped gas sensor over time.

Despite showing high sensor response by few layer MoS<sub>2</sub>-based TFT sensor, their low conductivity limits the performance of device [34, 218]. The high surface to volume ratio of graphene and its derivatives opened up possibilities of hybrid gas sensors, where graphene and its derivative provided better electrical conductivity to the device. Theoretical calculations done using DFT have expounded that pollutant gases, like NO<sub>2</sub>, NO, and SO<sub>2</sub>, firmly interact with MoS<sub>2</sub> surfaces. Numerous experimental confirmations of these theoretical results have been reported. A three-layer-grown MoS<sub>2</sub>-based resistive sensor showed a NO<sub>2</sub> detection limit of 120 ppb in dark conditions [326].

In order to improve the sensing behavior, the blending of MoS<sub>2</sub> with graphene nanosheet was adopted [42, 330, 331]. To enhance the sensor response and selectivity to NO<sub>2</sub> more, a composite of reduced graphene oxide (rGO) and MoS<sub>2</sub> was prepared [332]. The p-type nature of rGO, due to oxygen and water doping and n-type nature of MoS<sub>2</sub> make p–n junction. MoS<sub>2</sub> provided selectivity and sensibility, while rGO had provided betterment in electronic properties. Zhou et al. also fabricated rGO/MoS<sub>2</sub> gas sensor for NO<sub>2</sub> detection [333]. The fabricated composite structure showed 200% enhanced performance than the bare rGO sensor. The device showed sensing response of 59.8% towards 2 ppm NO<sub>2</sub> at 60 °C.

On the contrary, Long et al., fabricated gas sensor using MoS<sub>2</sub>/graphene hybrid aerogel for NO<sub>2</sub> detection [118]. The MoS<sub>2</sub>/graphene-based sensor showed ultralow detection limit of 50 ppb NO<sub>2</sub>. The hybrid was integrated over low power micro heater for temperature-dependent gas detection measurement and on heating at 200 °C sensor show improved recovery and response time of less than 1 min compared to RT measurements. The schematic and optical image of the device with microheater is shown in Fig. 19.

Many other works have been reported where the sensing performance was improvised by using graphene over MoS<sub>2</sub> [334, 335]. Despite the good selectivity of the MoS<sub>2</sub>/rGO sensor, the MoS<sub>2</sub> has serious issues like agglomeration on the substrate. Therefore, the fabrication of MoS<sub>2</sub> gas sensor with enhanced sensing activity was a challenge. CdS was used as sensing material and assumed to provide good electron transfers between heterostructure [336].

Tabata et al., fabricated gate tunable MoS<sub>2</sub>/graphene NO<sub>2</sub> sensor [29]. To understand the role of only heterojunction, the other gas-sensing parts were passivated by the gas barrier layer. Poly methyl methacrylate (PMMA) was used as gas barrier layer. The device showed the strong dependencies on the type of bias (forward or reverse) and back gate voltage. With an increase in reverse bias and negative gate voltage device showed better performance. Jung et al. also fabricated the flexible gas sensor by transferring the MoS<sub>2</sub>/rGO on the PET substrate that showed optical transmittance ~93% [337]. The flexible MoS<sub>2</sub>/rGO showed good performance at a bending radius of 14 mm and detection as low as 0.15 ppm of NO<sub>2</sub>.

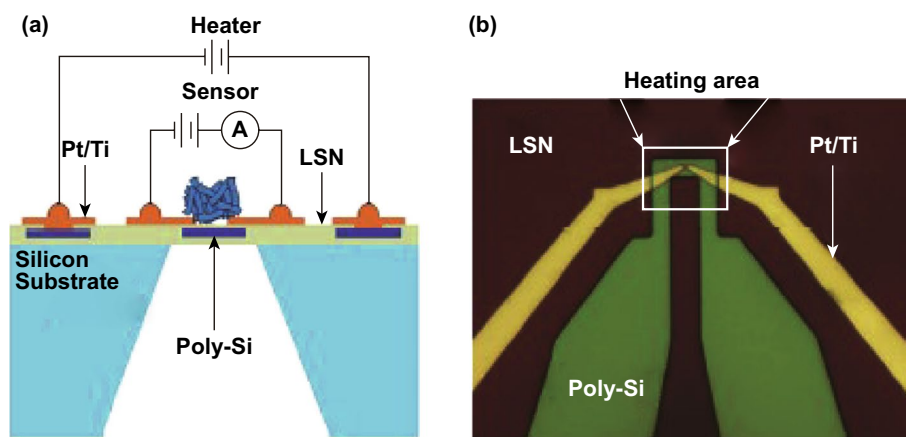


**Fig. 19** **a** Schematic diagram of NO<sub>2</sub> gas sensor with microheater sensor. **b** Optical image of poly-silicon microheater with Pt/Ti electrodes. Reproduced with permission from Ref. [118]. Copyright (2016) Wiley-VCH

On the contrary, Ikram et al. used a thin layer of  $\text{In}(\text{OH})_3$  on the  $\text{MoS}_2$  nanosheets to improve the performance of  $\text{NO}_2$  gas sensor [338]. The presence of point and line defects in  $\text{MoS}_2/\text{In}(\text{OH})_3$  improves the electrical conductivity and provides the accessibility of active sites for target gas. The ease of fabrication of  $\text{MoS}_2/\text{MoO}_3$  composites in one step has also grabbed attention and the sensor showed a remarkable sensor response of  $\sim 33.6\%$  with complete recovery to 10 ppm  $\text{NO}_2$  at RT [339]. The sensor response of 2D materials to the surrounding critically affect the long-term reliability of the sensing device. Therefore, Shi et al. fabricated a layered device using black phosphorus (BP) as the top gate, Boron nitride as a dielectric layer and  $\text{MoS}_2$  as conduction channel [340]. The gas adsorption ability of BP makes it a gas-sensing material and BN isolates the conduction channel of  $\text{MoS}_2$  from ambient. The multilayered gas sensor showed a detection limit of 3.3 ppb to  $\text{NO}_2$ . The  $\text{SnS}_2$  nanosheets were also used to fabricate the sensor due to their

high adsorption sites availability and showed response 22.3 times higher than pristine  $\text{SnS}_2$  sensor [341].

Apart from the integration of 2D nanostructure with  $\text{MoS}_2$ , integration of 1D also offers enhancement in gas-sensing properties. Deokar et al. fabricated CNT/ $\text{MoS}_2$ -based hybrid  $\text{NO}_2$  gas sensor [342]. Hexagonal shaped  $\text{MoS}_2$  nanoplates were grown on vertical aligned CNTs. Few tens (25, 50, 100) of ppm to hundreds (25, 100) of ppb of  $\text{NO}_2$  at RT was monitored. An illustration of the gas-sensing mechanism of 2D/1D heterostructure is depicted in Fig. 20.

Zhao et al. fabricated a hybrid of  $\text{MoS}_2$ /porous Si nanowire [343]. The  $\text{MoS}_2$  nanosheets were grown by sulfurization of Mo thin film deposited using DC magnetic sputtering. The hybrid device showed better performance than bare  $\text{MoS}_2$  and porous Si NW with low detection concentration of 1 ppm. Keeping the success of  $\text{MoS}_2$  and porous Si NW in attention, ZnO nanowires were also used in forming the heterostructure [344].  $\text{MoS}_2$  was grown by the same sulfurization of Mo thin films deposited by DC magnetic sputtering. The  $\text{MoS}_2$  on ZnO NW showed an excellent sensor response, recovery, repeatability and selectivity up to low detection of 200 ppb.  $\text{MoS}_2$ , that naturally act as n-type semiconductor forms heterostructure with n-type ZnO NW and charge interfacial charge separation takes place. The electron in the CB of  $\text{MoS}_2$  flows to the CB of ZnO NWs till their Fermi level gets aligned. The type of heterostructure (type I and type II) can be decided by the band gap and the work function of the two materials. Similarly, other reports were also reported where ZnO nanowires were used with p-type  $\text{MoS}_2$  nanosheets to improve the sensors performance [345].

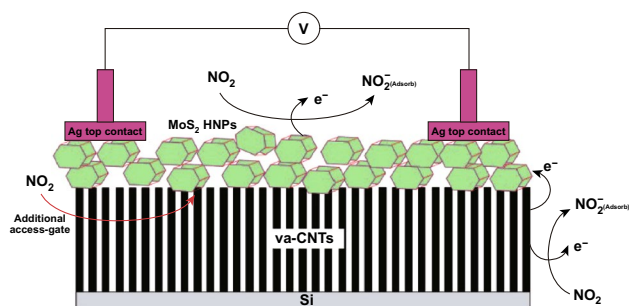


**Fig. 20** Schematic of  $\text{MoS}_2$  deposited over CNT-based device. Reproduced with permission from Ref. [342]. Copyright (2017) Wiley-VCH

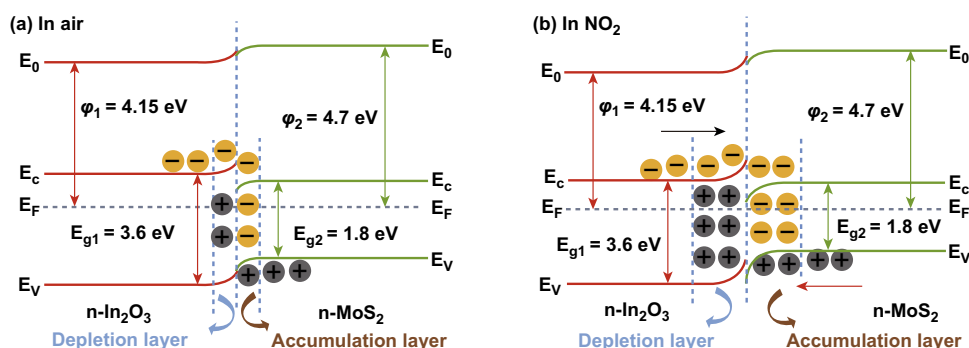


**Fig. 21** Energy band diagram of  $\text{In}_2\text{O}_3/\text{MoS}_2$  heterojunction in **a** air and **b**  $\text{NO}_2$  ambient. Reproduced with permission from Ref. [346]. Copyright (2019) Elsevier



On the contrary to NW and CNTs, hollow tubes have also been considered and effective 1D nanostructure for enhancing the gas-sensing properties. Yang et al. fabricated  $\text{NO}_2$  gas-sensing device using  $\text{In}_2\text{O}_3$  hollow tube and  $\text{MoS}_2$  nanoparticles [346]. The  $\text{In}_2\text{O}_3/\text{MoS}_2$  composite synthesized by layer by layer technology. Both n-type metal oxides nanostructure and n-type  $\text{MoS}_2$  form a heterostructure. Depending upon the band gap and work function, the majority carrier flows from CB of  $\text{MoS}_2$  to CB of metal oxide (MO) nanostructure and vice versa till their Fermi level gets aligned. When the sensor is exposed in the air ambient, the oxygen molecules capture electrons from  $\text{MoS}_2$  and MO nanostructure and forms  $\text{O}_2^-$  ions. An energy band diagram that explains the sensing mechanism in the air and in  $\text{NO}_2$  ambient is shown in Fig. 21. Once the sensor is exposed into  $\text{NO}_2$  ambient, the  $\text{NO}_2$  molecules capture electrons from the sensing layer and adsorbed  $\text{O}_2^-$ , hence increase the device resistance.

When the sensor is again released in the air ambient, the electron trapped by  $\text{NO}_2$  is again released to CB sensing materials leading to the restoration of device resistance. In band diagram terminology, when the sensor is exposed to the  $\text{NO}_2$ , the electrophilic nature of  $\text{NO}_2$  reduces the carrier concentration in the depletion region resulting an increase in the resistance.

Therefore, the quality of the interface between the  $\text{MoS}_2$  and MO nanostructure greatly affects the sensing properties.

Among different heterojunctions, 2D/0D offers improved gas-sensing properties (sensor response, recovery time, and improved time) due to the enhanced penetration and diffusion of gas molecules. The first 2D/0D hybrid heterostructure was fabricated and demonstrated by Han et al. for gas  $\text{NO}_2$  gas sensing. Han and co-workers fabricated 2D/0D heterojunction using  $\text{MoS}_2$  nano-sheets and ZnO NP that exhibited sensor response of 3050% for 5 ppm  $\text{NO}_2$  and long term stability of 10 weeks at RT [347].

The gas-sensing mechanism of 2D/0D heterostructure is explained with the help of Fig. 22. The defects on the surface of as deposited p-type  $\text{MoS}_2$  act as active sites for gas sensing.  $\text{NO}_2$  molecules accept electrons from  $\text{MoS}_2$  and change the electronic properties of the sensor. The integration of metal oxide 0D structure (n-type) over p-type forms a p-n junction followed by the formation of the depletion layer. The electron and hole diffusion keep happening from n-type to p-type and p-type to n-type, respectively, till their fermi levels get aligned. A built-in electric field balances the flow of majority carrier. Therefore, in the air, the  $\text{MoS}_2/\text{ZnO}$  junction shows poor conductivity due to the formation of potential barrier. When the sensor is brought in the

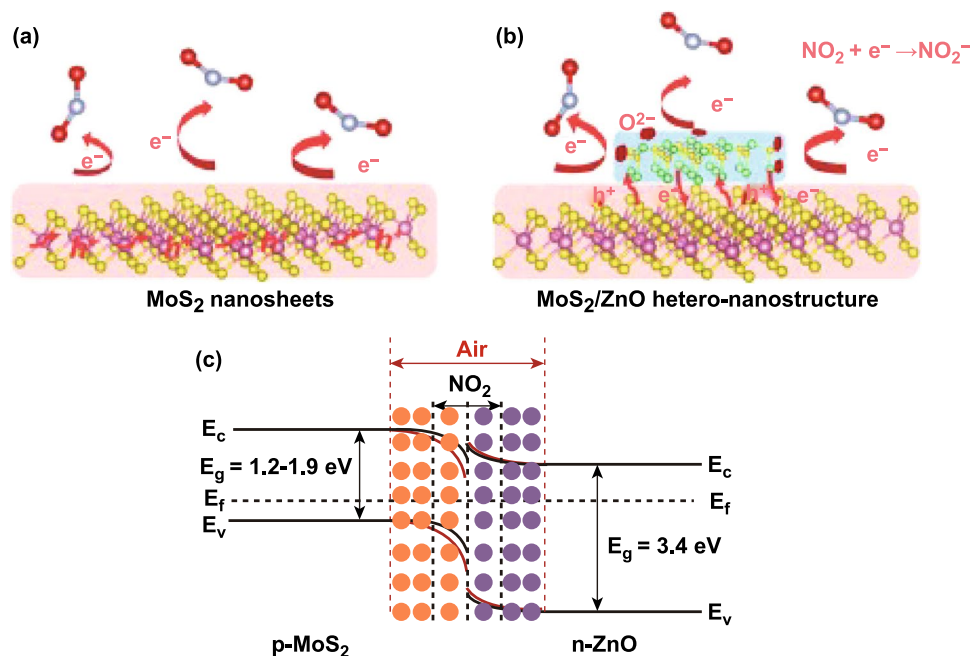


**Fig. 22** Schematic of sensing mechanism of **a** pure  $\text{MoS}_2$  nanosheets and **b** hybrid mechanism. **c** Band diagram of hybrid 2D/0D heterojunction gas sensor in air ambient and in the  $\text{NO}_2$  ambient. Reproduced with permission from Ref. [347]. Copyright (2015) American Chemical Society

ambience of  $\text{NO}_2$ , the  $\text{NO}_2$  molecules take electrons from metal oxide nanoparticle and the equilibrium of electron and hole is broken. The extra holes that were counter balanced by the electrons taken up by the  $\text{NO}_2$  molecule migrate to the  $\text{MoS}_2$ . Therefore, during adsorption of  $\text{NO}_2$ , holes are accumulated on the  $\text{MoS}_2$  surface and the width of depletion layer decreases that leads to the increase in conductivity of  $\text{MoS}_2/\text{ZnO}$  heterostructure. The increase in the conductivity of heterostructure enhances gas-sensing properties.

Another metal oxide nanoparticle that was used for the hybrid  $\text{MoS}_2$  sensor was  $\text{SnO}_2$  NPs. The  $\text{MoS}_2/\text{SnO}_2$   $\text{NO}_2$ -based sensor showed a response from 18.7 to 5 ppm  $\text{NO}_2$

[348]. Similarly, Xin et al. fabricated device using PbS quantum dots [349].

The  $\text{MoS}_2/\text{PbS}$  QDs showed sensing performance better than bare  $\text{MoS}_2$ . The response showed by the hybrid device was 50 times higher than pure  $\text{MoS}_2$  at 100 ppm with recovery ratio of around 99%. In another report, Ag nanoparticle was used for surface modification of the  $\text{Fe}_2\text{O}_3/\text{MoS}_2$  heterojunction. The modified sensor showed response to 5 ppm  $\text{NO}_2$  as high as 202.2% which was 11Times higher than the bare  $\text{MoS}_2$  device [27]. On the contrary, n-type  $\text{MoS}_2$  was also used for device fabrication. The n-type-CdTe quantum dots also used on n-type  $\text{MoS}_2$  nanoworms to enhance the

**Table 5** Summary of various  $\text{MoS}_2$  heterostructures  $\text{NO}_2$  sensors

Sensing film	Electrodes	Conc. (ppm)	Def	T (°C)	S (%)	Res time (s)	Rec time (S)	References
Graphene/ $\text{MoS}_2$	Au	50	$\frac{(R_{\text{gas}}-R_{\text{air}})}{R_{\text{air}}}$	RT	83	–	–	[332]
rGO/ $\text{MoS}_2$	Au	2	$\frac{(R_{\text{gas}}-R_{\text{air}})}{R_{\text{air}}}$	60	59.8	–	–	[333]
rGO/ $\text{MoS}_2$	Au	3	$\frac{R_{\text{gas}}}{R_{\text{air}}}$	160	1.23	8	20	[351]
Graphene/ $\text{MoS}_2$	Pt/Ti	0.5	$\frac{(R_{\text{gas}}-R_{\text{air}})}{R_{\text{air}}}$	200	10	21.6	29.4	[118]
$\text{MoS}_2$ /graphene	Au	10	$\frac{(I_{\text{air}}-I_{\text{gas}})}{I_{\text{air}}}$	200	69	0.7	0.9	[334]
Graphene/ $\text{MoS}_2$	–	500	$\frac{(R_{\text{gas}}-R_{\text{air}})}{R_{\text{air}}}$	RT	61	22	35	[335]
rGO/ $\text{MoS}_2/\text{CdS}$	NA	0.2	$\frac{(R_{\text{gas}}-R_{\text{air}})}{R_{\text{air}}}$	75	27.4	25	34	[336]
$\text{MoS}_2/\text{In}(\text{OH})_3$	NA	100	$\frac{R_{\text{air}}}{R_{\text{gas}}}$	RT	15.4	1.6	NA	[338]
$\text{MoS}_2/\text{MoO}_3$	Au	10	$\frac{(R_{\text{gas}}-R_{\text{air}})}{R_{\text{air}}}$	RT	33.5	19	182	[339]
$\text{SnS}_2/\text{MoS}_2$	Au	100	$\frac{R_{\text{air}}}{R_{\text{gas}}}$	RT	25.9	2	28.2	[341]
$\text{MoS}_2/\text{CNT}$	Ag	50	$\frac{R_{\text{gas}}}{R_{\text{air}}}$	RT	12.6	–	–	[342]
$\text{MoS}_2/\text{p-Si}$ NWs	Ag	50	$\frac{(R_{\text{gas}}-R_{\text{air}})}{R_{\text{air}}}$	RT	28.4	–	–	[343]
$\text{MoS}_2/\text{ZnO}$ NW	Silver	50	$\frac{(R_{\text{gas}}-R_{\text{air}})}{R_{\text{air}}}$	200	29.4	300	–	[344]
ZnO NW/ $\text{MoS}_2$	Au/Ti	50 ppb	$\frac{(R_{\text{gas}}-R_{\text{air}})}{R_{\text{air}}}$	60	63	–	–	[345]
$\text{MoS}_2/\text{In}_2\text{O}_3$ NT	–	50	$\frac{R_{\text{air}}}{R_{\text{gas}}}$	RT	209	–	–	[346]
$\text{MoS}_2/\text{ZnO}$	Au	5	$\frac{(I_{\text{gas}}-I_{\text{air}})}{I_{\text{air}}}$	RT	3050	40	1000	[347]
$\text{MoS}_2/\text{SnO}_2$ NPs	Au/Ti	5	$\frac{R_{\text{gas}}}{R_{\text{air}}}$	RT	18.7	74	NA	[348]
Ag- $\text{Fe}_2\text{O}_3/\text{MoS}_2$	Ag-Pd	5	$\frac{(R_{\text{gas}}-R_{\text{air}})}{R_{\text{air}}}$	120	202.2	81	355	[27]
CdTe/ $\text{MoS}_2$	Ag	10	$\frac{(R_{\text{gas}}-R_{\text{air}})}{R_{\text{air}}}$	RT	40	16	114	[350]
$\text{MoS}_2/\text{SnO}_2$	Au	10	$\frac{(R_{\text{gas}}-R_{\text{air}})}{R_{\text{air}}}$	RT	28	408	162	[352]

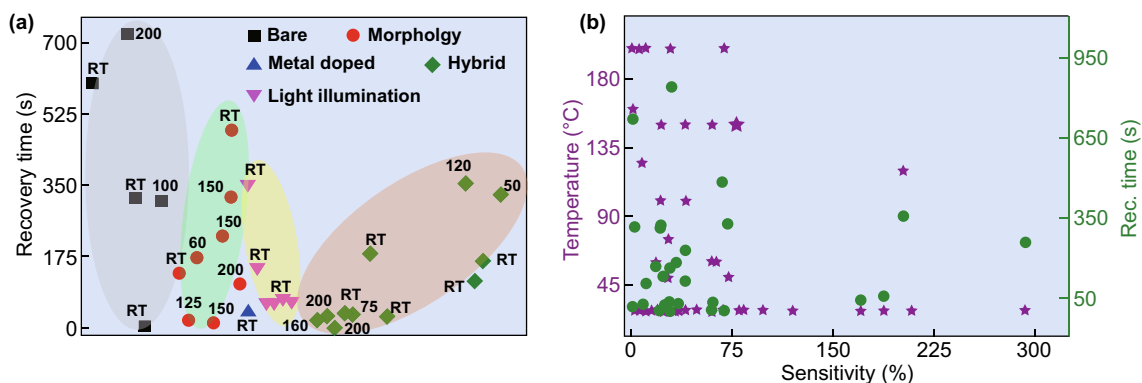


**Fig. 23** **a** Summary of the recovery time obtained through various strategies in MoS<sub>2</sub>. Bare MoS<sub>2</sub>-based NO<sub>2</sub> sensors have highest recovery time followed by the morphology-driven MoS<sub>2</sub>. The light-assisted NO<sub>2</sub> sensors have the lowest recovery time and can operate easily at RT. MoS<sub>2</sub> heterostructure-based sensors have mixed recovery time with different operating temperatures. **b** MoS<sub>2</sub>-based sensors can operate easily at low temperatures and have low recovery time. Data presented was taken from Refs. [17, 24, 27, 31–36, 118–122, 214, 303–310, 320, 325, 328, 329, 333–336, 338–352]

sensing performance [350]. The device showed an excellent response of 40% over pristine MoS<sub>2</sub>. The band bending of n-type MoS<sub>2</sub> and n-type 0D is shown in Fig. 22c. We summarized the gas-sensing performances of various MoS<sub>2</sub> heterostructures in Table 5.

## 7 Challenges and Future Perspectives

MoS<sub>2</sub> has shown immense gas-sensing capacity without any doubt and also shown great performance in the detection of various gas molecules like NO<sub>2</sub>, NH<sub>3</sub>, H<sub>2</sub>, H<sub>2</sub>S etc. However, some major issues still have to be overcome in order to boost the efficiency of MoS<sub>2</sub> gas sensors. There are several crucial challenges to be overcome to build high-performance MoS<sub>2</sub>-based NO<sub>2</sub> sensors. Gas-sensing performance depends on certain important parameters including sensor response, recovery time, selectivity, and stability. MoS<sub>2</sub> is extremely susceptible to different gases, and its conductivity varies dramatically under exposure to these gases. A small exposure of any gas to MoS<sub>2</sub> will notably change sensor response. Thus, the detection of target gas molecules is critical by MoS<sub>2</sub>.

Theoretically, NO<sub>2</sub> and NH<sub>3</sub> both have almost identical adsorption energy with similar adsorption sites. However, NO<sub>2</sub> has an electron acceptor nature, while NH<sub>3</sub> has an electron donor nature. The synthesis of such morphology which is highly selective for NO<sub>2</sub> molecules is therefore advantageous and can increase NO<sub>2</sub> selectivity. MoS<sub>2</sub> has a high surface to volume ratio, so it is useful to functionalize MoS<sub>2</sub>

flakes with NO<sub>2</sub> capturing agents to improve NO<sub>2</sub> adsorption on MoS<sub>2</sub> flakes.

Another benefit of MoS<sub>2</sub> is the effective control on morphology. Morphology influences the gas diffusion in the sensing film. The role of different morphologies in detecting NO<sub>2</sub> has been already studied in detail with various conventional metal oxides, including ZnO, SnO<sub>2</sub> and in TiO<sub>2</sub> etc. So, there is plenty of space for NO<sub>2</sub> gas detection by morphology-driven sensor. In addition, NO<sub>2</sub> molecule adsorption on MoS<sub>2</sub> depends greatly on the position, so any effort to increase the NO<sub>2</sub> adsorption sites can not only enhance the sensor response but also boost the selectivity ability. The RT recovery is yet another big challenge for MoS<sub>2</sub>-based NO<sub>2</sub> gas sensors. MoS<sub>2</sub> has strong adsorption energy with NO<sub>2</sub> gas molecules. Currently, bare MoS<sub>2</sub>-based NO<sub>2</sub> sensors have experienced incomplete recovery at RT. RT thermal energy is not capable to desorb the adsorbed NO<sub>2</sub> gas. This demands the operation of sensors at elevated temperature from RT. However, this will happen at the cost of reduce sensor response performance of the sensor. So thermal treatment for achieving full recovery is not feasible. Recently the light-assisted recovery of the gas sensors is open a new promising way to develop RT gas sensors. Light illumination not only helps in the recovery of the sensors but it also enhances the 3S performance (low response and recovery time and sensor response). Bare MoS<sub>2</sub>-based sensors have improved RT recovery under UV light illumination so far.

Very few attempts have been made in recent years to use residual spectrum (visible, NIR, and higher region). Thus,

an intensive approach is still required to explore the wavelength-dependent NO<sub>2</sub> gas-sensing response and to explore light induced carrier generation and adsorption of NO<sub>2</sub> molecules.

Apart from the sensor response and recovery time, fast response of the gas sensor is also an essential parameter. Each sensor's response time depends on how rapidly the gas molecules reacted to sensing film and change their respective parameter. Till now, the reported response time of NO<sub>2</sub> molecules detection by MoS<sub>2</sub> is in few seconds. So, developing NO<sub>2</sub> sensors which can respond in few milliseconds or microseconds is still challenging. The strategy to improve the ultrafast sensors relies primarily on the interaction between gas molecules and MoS<sub>2</sub> and the charge transfer in MoS<sub>2</sub>. The fast separation of the charge carriers can be improved by forming MoS<sub>2</sub> heterostructures sensing devices.

In addition, a proper attention is needed to pay on metal electrodes, which collect generated charges. The metal contacts has played a vital role with MoS<sub>2</sub> in gas sensing. Identification of high-performance metal contacts is the prerequisite to utilizing the full performance of the MoS<sub>2</sub>-based NO<sub>2</sub> sensors. An improved theoretical and experimental efforts with profound insight and understanding is also needed, which will contribute to the development of high-performance NO<sub>2</sub> sensors. Several routes to develop high-performance electrical contact should identify.

The standard air quality guidelines, according to WHO for NO<sub>2</sub> exposure are 82 ppb for an hour and 410 ppb for a year. Exposure to NO<sub>2</sub> for a long time above that level causes health problems. The recorded lower detection limit for MoS<sub>2</sub>-based NO<sub>2</sub> sensor has been in the ppb. Thus, a lot of effort is needed to develop ultrasensitive NO<sub>2</sub> sensors, which is a crucial task. It is important to find NO<sub>2</sub> sensitive materials that can be easily integrated with MoS<sub>2</sub>, and can identify the lower concentration of NO<sub>2</sub> easily. Furthermore, such materials should also fasten the transfer of charges for rapid sensor response. Recently, the use of spectroscopic techniques such as laser sources and electrical shields have attracted the attention of the scientific community due to their NO<sub>2</sub> trace detection ability. NO<sub>2</sub> molecules have the absorption spectrum in visible region so it offers a great chance to electronic exciton in the visible region of NO<sub>2</sub> molecules. The use of spectroscopic techniques for trace detection of NO<sub>2</sub> with MoS<sub>2</sub> sensors could be a new approach.

Light-assisted NO<sub>2</sub> sensing has attracted the scientific community over the last two years. Metal NP-doped MoS<sub>2</sub> sensors have already proved their importance in gas sensing. Surface plasma resonance (SPR) characteristics of MoS<sub>2</sub> may be a new approach to developing gas sensor-based on MoS<sub>2</sub>. New experimental efforts should devote to harnessing the potential of plasmonic in gas sensing. SPR can stimulate the interface of MoS<sub>2</sub> and metal and alter the index refractive. A good choice of metal NPs and appropriate wavelengths will be helpful in designing the high-performance NO<sub>2</sub> sensors.

The MoS<sub>2</sub>-based NO<sub>2</sub> sensors are basically chemiresistance sensors in which the change in conductance of MoS<sub>2</sub> film is the parameter. The conductivity of film is significantly influenced by the presence of the environment such as traces of various chemicals, moisture, humidity, corrosion due to toxic vapors, residual charges. These all drastically reduce the reliability, stability and repeatability of gas sensors. Efforts are required to increase the stability of the sensing devices.

## 8 Conclusions

In this review, we summarized the various theoretical and experimental strategies employed to fabricate MoS<sub>2</sub>-based NO<sub>2</sub> gas sensors. We critically discussed the advantages of utilizing the 2D MoS<sub>2</sub> in developing NO<sub>2</sub> sensors. We briefly discussed the noble properties of MoS<sub>2</sub> and established MoS<sub>2</sub> as a potential candidate for the gas sensing. The inherent nonzero bandgap, high carrier mobility, fast charge transport, high reactivity, presence of favorable adsorption sites, large surface to volume ratio, and optical properties make MoS<sub>2</sub> amenable for gas molecule adsorption. Both theoretical and experimental studies have confirmed that NO<sub>2</sub> adsorption in MoS<sub>2</sub> is controlled by the charge transfer process. NO<sub>2</sub> behaves as a strong oxidizing agent and depletes the electrons from MoS<sub>2</sub>. Theoretical studies revealed NO<sub>2</sub> adsorption in MoS<sub>2</sub> is position dependent. The 2H and 1T MoS<sub>2</sub> have their importance in NO<sub>2</sub> gas sensing. Although most of the work to fabricate MoS<sub>2</sub>-based NO<sub>2</sub> sensor have been carried out with 2H-MoS<sub>2</sub> phase, but the 1T MoS<sub>2</sub> phase is emerged as the potential candidate for NO<sub>2</sub> detection. The aforementioned hypothesis has been verified theoretically and must be taken into account in experiments as well. Theoretical and experimental studies confirmed that



the defective MoS<sub>2</sub> have higher interaction and have high NO<sub>2</sub> detection ability than the pristine MoS<sub>2</sub>. Furthermore, metal doping at the vacancy sites is an alternative way to develop highly sensitive, fast response and RT-recoverable NO<sub>2</sub> sensors. Different MoS<sub>2</sub> morphologies have different number of NO<sub>2</sub> adsorption sites. Thus, NO<sub>2</sub> sensing performance of MoS<sub>2</sub> could be further improved and determined by morphology.

The formation of MoS<sub>2</sub> heterostructures can significantly affect the NO<sub>2</sub> sensing performances. MoS<sub>2</sub> heterostructures rapidly separate the charges and could be helpful in developing fast response and recover gas sensors. Among all, light-assisted NO<sub>2</sub> sensors have paved a new path to achieve fast RT-recoverable NO<sub>2</sub> sensors. Finally, we graphically presented the gas-sensing characteristics such as recovery time, temperature, and sensitivity obtained from various reports in Fig. 23 to have an easy catch over the progress. In Fig. 23a, we have summarized the recovery time obtained through various strategies. Many bare MoS<sub>2</sub> NO<sub>2</sub> sensors either have incomplete recovery, or need to operate at high temperature for full recovery. Hence, we have few data points. The data revealed that NO<sub>2</sub> has high adsorption energy with MoS<sub>2</sub> at RT. Due to high adsorption energy, bare MoS<sub>2</sub> NO<sub>2</sub> sensors are suffered from incomplete or long recovery time at RT. The morphology controlled MoS<sub>2</sub> sensors have a good recovery but in a moderate temperature range. External thermal energy is needed to recover the MoS<sub>2</sub> sensors. MoS<sub>2</sub> heterostructures-based sensors have the mixed recovery time with different operating temperature depending on their partner materials and charge transfer mechanism. It is also observed that MoS<sub>2</sub> heterostructures NO<sub>2</sub> sensors have the comparatively less recovery time than the bare MoS<sub>2</sub> and morphology-driven NO<sub>2</sub> sensors due to faster separation of charges at RT and moderate temperature. Interestingly, light-assisted NO<sub>2</sub> sensors have the lowest recovery time with RT operation. Thus, light illumination has played a significant role in improving NO<sub>2</sub> sensors at RT. Photogenerated electrons and holes pairs crucially help in the desorption of the adsorbed NO<sub>2</sub> molecules. In Fig. 23b, we have concluded the various reports and summarize the gas-sensing factors. Graphical representation revealed MoS<sub>2</sub>-based NO<sub>2</sub> sensors have a clear advantage over the traditional sensors in terms of temperature, cost and power. The statistics presented in the Fig. 23b has confirmed that NO<sub>2</sub> sensors based on MoS<sub>2</sub> can fill the performance gap shown in the Fig. 3. With traditional metal oxide sensors, we need high operating

temperature up to 500 °C while MoS<sub>2</sub> sensors can easily operate at low temperature range with high sensor response and selectivity with low recovery time.

**Acknowledgements** The authors acknowledge the Department of Atomic Energy (DAE) under Project No. 34/20/09/2015/BRNS and also the Department of Physics, IIT Ropar for providing financial support and the research facility.

**Open Access** This article is licensed under a Creative Commons Attribution 4.0 International License, which permits use, sharing, adaptation, distribution and reproduction in any medium or format, as long as you give appropriate credit to the original author(s) and the source, provide a link to the Creative Commons licence, and indicate if changes were made. The images or other third party material in this article are included in the article's Creative Commons licence, unless indicated otherwise in a credit line to the material. If material is not included in the article's Creative Commons licence and your intended use is not permitted by statutory regulation or exceeds the permitted use, you will need to obtain permission directly from the copyright holder. To view a copy of this licence, visit <http://creativecommons.org/licenses/by/4.0/>.

## References

1. T.W. Ashenden, T.A. Mansfield, Extreme pollution sensitivity of grasses when SO<sub>2</sub> and NO<sub>2</sub> are present in the atmosphere together. *Nature* **273**(5658), 142–143 (1978). <https://doi.org/10.1038/273142a0>
2. L. Calderón-Garcidueñas, B. Azzarelli, H. Acuna, R. Garcia, T.M. Gambling et al., Air pollution and brain damage. *Toxicol. Pathol.* **30**(3), 373–389 (2002). <https://doi.org/10.1080/01926230252929954>
3. R.J. van der A, H.J. Eskes, K.F. Boersma, T.P.C. van Noije, M. Van Roozendaal et al., Trends, seasonal variability and dominant NO<sub>x</sub> source derived from a ten-year record of NO<sub>2</sub> measured from space. *J. Geophys. Res. Atmos.* **113**(D4), 302 (2008). <https://doi.org/10.1029/2007JD009021>
4. J.G. Speight, Chapter one—inorganic chemicals in the environment, in ed. by J. Speight *Environmental Inorganic Chemistry for Engineers* (Butterworth-Heinemann, 2017), pp. 1–49. <https://doi.org/10.1016/B978-0-12-849891-0.00001-1>
5. D. Fowler, J.N. Cape, I.D. Leith, I.S. Paterson, J.W. Kinnaird et al., Rainfall acidity in northern Britain. *Nature* **297**(5865), 383–385 (1982). <https://doi.org/10.1038/297383a0>
6. N.M. Elsayed, Toxicity of nitrogen dioxide: an introduction. *Toxicology* **89**(3), 161–174 (1994). [https://doi.org/10.1016/0300-483X\(94\)90096-5](https://doi.org/10.1016/0300-483X(94)90096-5)
7. J.A. Burney, The downstream air pollution impacts of the transition from coal to natural gas in the United States. *Nat. Sustain.* **3**(2), 152–160 (2020). <https://doi.org/10.1038/s41893-019-0453-5>
8. L. Meier, P. Tanskanen, L. Heng, G.H. Lee, F. Fraundorfer et al., PIXHAWK: a micro aerial vehicle design for

- autonomous flight using onboard computer vision. *Auton. Robots* **33**(1), 21–39 (2012). <https://doi.org/10.1007/s10514-012-9281-4>
9. C. Li, L. Yu, W. He, Y. Cheng, G. Song, Development of local emissions rate model for light-duty gasoline vehicles: Beijing field data and patterns of emissions rates in EPA simulator. *Transp. Res. Record.* **2627**(1), 67–76 (2017). <https://doi.org/10.3141/2627-08>
  10. A. Richter, J.P. Burrows, H. Nüß, C. Granier, U. Niemeier, Increase in tropospheric nitrogen dioxide over China observed from space. *Nature* **437**(7055), 129–132 (2005). <https://doi.org/10.1038/nature04092>
  11. R.J. van der A, D.H.M.U. Peters, H. Eskes, K.F. Boersma, M. Van Roozendaal et al., Detection of the trend and seasonal variation in tropospheric NO<sub>2</sub> over China. *J. Geophys. Res. Atmos.* **111**(D12), D12317 (2006). <https://doi.org/10.1029/2005jd006594>
  12. P. Castellanos, K.F. Boersma, Reductions in nitrogen oxides over Europe driven by environmental policy and economic recession. *Sci. Rep.* **2**(1), 265 (2012). <https://doi.org/10.1038/srep00265>
  13. P.K. Hopke, Contemporary threats and air pollution. *Atmos. Environ.* **43**(1), 87–93 (2009). <https://doi.org/10.1016/j.atmosenv.2008.09.053>
  14. C. Zhang, C. Liu, Q. Hu, Z. Cai, W. Su et al., Satellite UV–Vis spectroscopy: implications for air quality trends and their driving forces in China during 2005–2017. *Light Sci. Appl.* **8**(1), 100 (2019). <https://doi.org/10.1038/s41377-019-0210-6>
  15. R.G. Derwent, K. Nodopt, Long-range transport and deposition of acidic nitrogen species in north-west Europe. *Nature* **324**(6095), 356–358 (1986). <https://doi.org/10.1038/324356a0>
  16. J.A. Bernstein, N. Alexis, C. Barnes, I.L. Bernstein, A. Nel et al., Health effects of air pollution. *J. Allergy Clin. Immunol.* **114**(5), 1116–1123 (2004). <https://doi.org/10.1016/j.jaci.2004.08.030>
  17. D.J. Late, Y.-K. Huang, B. Liu, J. Acharya, S.N. Shirodkar et al., Sensing behavior of atomically thin-layered MoS<sub>2</sub> transistors. *ACS Nano* **7**(6), 4879–4891 (2013). <https://doi.org/10.1021/nn400026u>
  18. K. Luo, R. Li, W. Li, Z. Wang, X. Ma et al., Acute effects of nitrogen dioxide on cardiovascular mortality in Beijing: an exploration of spatial heterogeneity and the district-specific predictors. *Sci. Rep.* **6**(1), 38328 (2016). <https://doi.org/10.1038/srep38328>
  19. W.H. Organization, World health statistics 2016: monitoring health for the SDGs sustainable development goals (World Health Organization; 2016)
  20. W.H. Organization, Guidelines for drinking-water quality (World Health Organization; 1993)
  21. A. Hulanicki, S. Glab, F. Ingman, Chemical sensors: definitions and classification. *Pure Appl. Chem.* **63**(9), 1247–1250 (1991). <https://doi.org/10.1351/pac199163091247>
  22. G.W. Hunter, L.-Y. Chen, P.G. Neudeck, D. Knight, C.-C. Liu et al., *Chemical Gas Sensors for Aeronautic and Space Applications 2* (1998)
  23. J. Guerrero-Ibáñez, S. Zeadally, J. Contreras-Castillo, Sensor technologies for intelligent transportation systems. *Sensors* **18**(4), 1212 (2018). <https://doi.org/10.3390/s18041212>
  24. H. Long, L. Chan, A. Harley-Trochimczyk, L.E. Luna, Z. Tang et al., 3D MoS<sub>2</sub> aerogel for ultrasensitive NO<sub>2</sub> detection and its tunable sensing behavior. *Adv. Mater. Interface* **4**(16), 1700217 (2017). <https://doi.org/10.1002/admi.20170217>
  25. B. Zhao, C.Y. Li, L.L. Liu, B. Zhou, Q.K. Zhang et al., Adsorption of gas molecules on Cu impurities embedded monolayer MoS<sub>2</sub>: A first-principles study. *Appl. Surf. Sci.* **382**, 280–287 (2016). <https://doi.org/10.1016/j.apsusc.2016.04.158>
  26. X. Chen, Y. Shen, P. Zhou, X. Zhong, G. Li et al., Bimetallic Au/Pd nanoparticles decorated ZnO nanowires for NO<sub>2</sub> detection. *Sens. Actuators B Chem.* **289**, 160–168 (2019). <https://doi.org/10.1016/j.snb.2019.03.095>
  27. M. Yin, Y. Wang, L. Yu, H. Wang, Y. Zhu et al., Ag nanoparticles-modified Fe<sub>2</sub>O<sub>3</sub>@MoS<sub>2</sub> core-shell micro/nanocomposites for high-performance NO<sub>2</sub> gas detection at low temperature. *J. Alloys Compd.* **829**, 154471 (2020). <https://doi.org/10.1016/j.jallcom.2020.154471>
  28. Y. Xia, J. Wang, J.-L. Xu, X. Li, D. Xie et al., Confined formation of ultrathin ZnO nanorods/reduced graphene oxide mesoporous nanocomposites for high-performance room-temperature NO<sub>2</sub> sensors. *ACS Appl. Mater. Interfaces* **8**(51), 35454–35463 (2016). <https://doi.org/10.1021/acsami.6b12501>
  29. H. Tabata, Y. Sato, K. Oi, O. Kubo, M. Katayama, Bias- and gate-tunable gas sensor response originating from modulation in the Schottky barrier height of a graphene/MoS<sub>2</sub> van der Waals heterojunction. *ACS Appl. Mater. Interfaces* **10**(44), 38387–38393 (2018). <https://doi.org/10.1021/acsami.8b14667>
  30. J. Li, Y. Lu, Q. Ye, M. Cinke, J. Han et al., Carbon nanotube sensors for gas and organic vapor detection. *Nano Lett.* **3**(7), 929–933 (2003). <https://doi.org/10.1021/nl034220x>
  31. M. Donarelli, S. Prezioso, F. Perrozzi, F. Bisti, M. Nardone et al., Response to NO<sub>2</sub> and other gases of resistive chemically exfoliated MoS<sub>2</sub>-based gas sensors. *Sens. Actuators B Chem.* **207**, 602–613 (2015). <https://doi.org/10.1016/j.snb.2014.10.099>
  32. B. Cho, M.G. Hahm, M. Choi, J. Yoon, A.R. Kim et al., Charge-transfer-based gas sensing using atomic-layer MoS<sub>2</sub>. *Sci. Rep.* **5**(1), 8052 (2015). <https://doi.org/10.1038/srep08052>
  33. L. Yu, F. Guo, S. Liu, J. Qi, M. Yin et al., Hierarchical 3D flower-like MoS<sub>2</sub> spheres: post-thermal treatment in vacuum and their NO<sub>2</sub> sensing properties. *Mater. Lett.* **183**, 122–126 (2016). <https://doi.org/10.1016/j.matlet.2016.07.086>
  34. H. Li, Z. Yin, Q. He, H. Li, X. Huang et al., Fabrication of single- and multilayer MoS<sub>2</sub> film-based field-effect

- transistors for sensing NO at room temperature. *Small* **8**(1), 63–67 (2012). <https://doi.org/10.1002/sml.201101016>
35. S.-Y. Cho, S.J. Kim, Y. Lee, J.-S. Kim, W.-B. Jung et al., Highly enhanced gas adsorption properties in vertically aligned MoS<sub>2</sub> layers. *ACS Nano* **9**(9), 9314–9321 (2015). <https://doi.org/10.1021/acsnano.5b04504>
36. B. Liu, L. Chen, G. Liu, A.N. Abbas, M. Fathi et al., High-performance chemical sensing using Schottky-contacted chemical vapor deposition grown monolayer MoS<sub>2</sub> transistors. *ACS Nano* **8**(5), 5304–5314 (2014). <https://doi.org/10.1021/nn5015215>
37. W. Yuan, G. Shi, Graphene-based gas sensors. *J. Mater. Chem. A* **1**(35), 10078–10091 (2013). <https://doi.org/10.1039/C3TA11774J>
38. C. Soldano, A. Mahmood, E. Dujardin, Production, properties and potential of graphene. *Carbon* **48**(8), 2127–2150 (2010). <https://doi.org/10.1016/j.carbon.2010.01.058>
39. M. Zheng, K. Takei, B. Hsia, H. Fang, X. Zhang et al., Metal-catalyzed crystallization of amorphous carbon to graphene. *Appl. Phys. Lett.* **96**(6), 063110 (2010). <https://doi.org/10.1063/1.3318263>
40. J.H. Choi, J. Lee, M. Byeon, T.E. Hong, H. Park et al., Graphene-based gas sensors with high sensitivity and minimal sensor-to-sensor variation. *ACS Appl. Nano Mater.* **3**(3), 2257–2265 (2020). <https://doi.org/10.1021/acsnm.9b02378>
41. D. Li, R.B. Kaner, Graphene-based materials. *Science* **320**(5880), 1170–1171 (2008). <https://doi.org/10.1126/science.1158180>
42. Q. He, Z. Zeng, Z. Yin, H. Li, S. Wu et al., Fabrication of flexible MoS<sub>2</sub> thin-film transistor arrays for practical gas-sensing applications. *Small* **8**(19), 2994–2999 (2012). <https://doi.org/10.1002/sml.201201224>
43. K.S. Novoselov, A. Mishchenko, A. Carvalho, A.H. Castro-Neto, 2D materials and van der Waals heterostructures. *Science* **353**(6298), aac9439 (2016). <https://doi.org/10.1126/science.aac9439>
44. R. Mas-Ballesté, C. Gómez-Navarro, J. Gómez-Herero, F. Zamora, 2D materials: to graphene and beyond. *Nanoscale* **3**(1), 20–30 (2011). <https://doi.org/10.1039/C0NR00323A>
45. H. Li, Q. Zhang, C.C.R. Yap, B.K. Tay, T.H.T. Edwin et al., From bulk to monolayer MoS<sub>2</sub>: evolution of raman scattering. *Adv. Funct. Mater.* **22**(7), 1385–1390 (2012). <https://doi.org/10.1002/adfm.201102111>
46. N. Bertram, J. Cordes, Y.D. Kim, G. Ganteför, S. Gemming et al., Nanoplatelets made from MoS<sub>2</sub> and WS<sub>2</sub>. *Chem. Phys. Lett.* **418**(1), 36–39 (2006). <https://doi.org/10.1016/j.cplett.2005.10.046>
47. B. Dubertret, T. Heine, M. Terrones, The rise of two-dimensional materials. *Acc. Chem. Res.* **48**(1), 1–2 (2015). <https://doi.org/10.1021/ar5004434>
48. Y. Han, M.-Y. Li, G.-S. Jung, M.A. Marsalis, Z. Qin et al., Sub-nanometre channels embedded in two-dimensional materials. *Nat. Mater.* **17**(2), 129–133 (2018). <https://doi.org/10.1038/nmat5038>
49. A. Gupta, T. Sakhivel, S. Seal, Recent development in 2D materials beyond graphene. *Prog. Mater. Sci.* **73**, 44–126 (2015). <https://doi.org/10.1016/j.pmatsci.2015.02.002>
50. K.F. Mak, C. Lee, J. Hone, J. Shan, T.F. Heinz, Atomically thin MoS<sub>2</sub>: a new direct-gap semiconductor. *Phys. Rev. Lett.* **105**, 136805 (2010). <https://doi.org/10.1103/PhysRevLett.105.136805>
51. C. Mai, A. Barrette, Y. Yu, Y.G. Semenov, K.W. Kim et al., Many-body effects in valleytronics: direct measurement of valley lifetimes in single-layer MoS<sub>2</sub>. *Nano Lett.* **14**(1), 202–206 (2014). <https://doi.org/10.1021/nl403742j>
52. J.R. Schaibley, H. Yu, G. Clark, P. Rivera, J.S. Ross et al., Valleytronics in 2D materials. *Nat. Rev. Mater.* **1**(11), 16055 (2016). <https://doi.org/10.1038/natrevmats.2016.55>
53. S.J. Kim, K. Choi, B. Lee, Y. Kim, B.H. Hong, Materials for flexible, stretchable electronics: graphene and 2D materials. *Ann. Rev. Mater. Res.* **45**(1), 63–84 (2015). <https://doi.org/10.1146/annurev-matsci-070214-020901>
54. D. Jariwala, V.K. Sangwan, D.J. Late, J.E. Johns, V.P. Dravid et al., Band-like transport in high mobility unencapsulated single-layer MoS<sub>2</sub> transistors. *Appl. Phys. Lett.* **102**(17), 173107 (2013). <https://doi.org/10.1063/1.4803920>
55. B. Chakraborty, H.S.S.R. Matte, A.K. Sood, C.N.R. Rao, Layer-dependent resonant Raman scattering of a few layer MoS<sub>2</sub>. *J. Raman Spectrosc.* **44**(1), 92–96 (2013). <https://doi.org/10.1002/jrs.4147>
56. S.I. Khondaker, M.R. Islam, Bandgap engineering of MoS<sub>2</sub> flakes via oxygen plasma: a layer dependent study. *J. Phys. Chem. C* **120**(25), 13801–13806 (2016). <https://doi.org/10.1021/acs.jpcc.6b03247>
57. F. Schedin, A.K. Geim, S.V. Morozov, E.W. Hill, P. Blake et al., Detection of individual gas molecules adsorbed on graphene. *Nat. Mater.* **6**(9), 652–655 (2007). <https://doi.org/10.1038/nmat1967>
58. E.H. Hwang, S. Das Sarma, Acoustic phonon scattering limited carrier mobility in two-dimensional extrinsic graphene. *Phys. Rev. B* **77**(11), 115449 (2008). <https://doi.org/10.1103/PhysRevB.77.115449>
59. E.V. Castro, H. Ochoa, M.I. Katsnelson, R.V. Gorbachev, D.C. Elias et al., Limits on charge carrier mobility in suspended graphene due to flexural phonons. *Phys. Rev. Lett.* **105**(26), 266601 (2010). <https://doi.org/10.1103/PhysRevLett.105.266601>
60. S. Vadukumpully, J. Paul, N. Mahanta, S. Valiyaveetil, Flexible conductive graphene/poly(vinyl chloride) composite thin films with high mechanical strength and thermal stability. *Carbon* **49**(1), 198–205 (2011). <https://doi.org/10.1016/j.carbon.2010.09.004>
61. G. Ko, H.Y. Kim, J. Ahn, Y.M. Park, K.Y. Lee et al., Graphene-based nitrogen dioxide gas sensors. *Curr. Appl. Phys.* **10**(4), 1002–1004 (2010). <https://doi.org/10.1016/j.cap.2009.12.024>
62. S. Gupta Chatterjee, S. Chatterjee, A.K. Ray, A.K. Chakraborty, Graphene–metal oxide nanohybrids for toxic gas sensor: a review. *Sens. Actuators B Chem.* **221**, 1170–1181 (2015). <https://doi.org/10.1016/j.snb.2015.07.070>



63. J. Ma, M. Zhang, L. Dong, Y. Sun, Y. Su et al., Gas sensor based on defective graphene/pristine graphene hybrid towards high sensitivity detection of NO<sub>2</sub>. *AIP Adv.* **9**(7), 075207 (2019). <https://doi.org/10.1063/1.5099511>
64. F. Yavari, N. Koratkar, Graphene-based chemical sensors. *J. Phys. Chem. Lett.* **3**(13), 1746–1753 (2012). <https://doi.org/10.1021/jz300358t>
65. Z. Yan, J. Lin, Z. Peng, Z. Sun, Y. Zhu et al., Toward the synthesis of wafer-scale single-crystal graphene on copper foils. *ACS Nano* **6**(10), 9110–9117 (2012). <https://doi.org/10.1021/nn303352k>
66. T.A. Land, T. Michely, R.J. Behm, J.C. Hemminger, G. Comsa, STM investigation of single layer graphite structures produced on Pt(111) by hydrocarbon decomposition. *Surf. Sci.* **264**(3), 261–270 (1992). [https://doi.org/10.1016/0039-6028\(92\)90183-7](https://doi.org/10.1016/0039-6028(92)90183-7)
67. J. Coraux, A.T. N'Diaye, C. Busse, T. Michely, Structural coherency of graphene on Ir(111). *Nano Lett.* **8**(2), 565–570 (2008). <https://doi.org/10.1021/nl0728874>
68. W. Tian, W. Li, W. Yu, X. Liu, A review on lattice defects in graphene: types, generation, effects and regulation. *Micromachines* **8**(5), 163 (2017). <https://doi.org/10.3390/mi8050163>
69. A.K. Geim, K.S. Novoselov, The rise of graphene. *Nat. Mater.* **6**(3), 183–191 (2007). <https://doi.org/10.1038/nmat1849>
70. M. Chhowalla, H.S. Shin, G. Eda, L.-J. Li, K.P. Loh et al., The chemistry of two-dimensional layered transition metal dichalcogenide nanosheets. *Nat. Chem.* **5**(4), 263–275 (2013). <https://doi.org/10.1038/nchem.1589>
71. W. Choi, N. Choudhary, G.H. Han, J. Park, D. Akinwande et al., Recent development of two-dimensional transition metal dichalcogenides and their applications. *Mater. Today* **20**(3), 116–130 (2017). <https://doi.org/10.1016/j.matto.2016.10.002>
72. S.-J. Choi, I.-D. Kim, Recent developments in 2D nanomaterials for chemiresistive-type gas sensors. *Electron. Mater. Lett.* **14**(3), 221–260 (2018). <https://doi.org/10.1007/s13391-018-0044-z>
73. A. Voshell, M. Terrones, M. Rana, Review of optical properties of two-dimensional transition metal dichalcogenides. *SPIE* 107540L (2018) <https://doi.org/10.1117/12.2323132>
74. T.C. Berkelbach, D.R. Reichman, Optical and excitonic properties of atomically thin transition-metal dichalcogenides. *Annu. Rev. Condens. Matter Phys.* **9**, 379–396 (2018). <https://doi.org/10.1146/annurev-conmatphys-033117-054009>
75. P. Xiao, J. Mao, K. Ding, W. Luo, W. Hu et al., Solution-processed 3D RGO–MoS<sub>2</sub>/pyramid Si heterojunction for ultrahigh detectivity and ultra-broadband photodetection. *Adv. Mater.* **30**(31), 1801729 (2018). <https://doi.org/10.1002/adma.201801729>
76. J. Deng, L. Zong, M. Zhu, F. Liao, Y. Xie et al., MoS<sub>2</sub>/HfO<sub>2</sub>/silicon-on-insulator dual-photogating transistor with ambipolar photoresponsivity for high-resolution light wavelength detection. *Adv. Funct. Mater.* **29**(46), 1906242 (2019). <https://doi.org/10.1002/adfm.201906242>
77. N. Guo, L. Xiao, F. Gong, M. Luo, F. Wang et al., Light-driven WSe<sub>2</sub>–ZnO junction field-effect transistors for high-performance photodetection. *Adv. Sci.* **7**(1), 1901637 (2020). <https://doi.org/10.1002/advs.201901637>
78. K.J. Berean, J.Z. Ou, T. Daeneke, B.J. Carey, E.P. Nguyen et al., 2D MoS<sub>2</sub> PDMS nanocomposites for NO<sub>2</sub> separation. *Small* **11**(38), 5035–5040 (2015). <https://doi.org/10.1002/sml.201501129>
79. H. Khan, A. Zavabeti, J.Z. Ou, T. Daeneke, Y. Li et al., Two dimensional tungsten oxide nanosheets with unprecedented selectivity and sensitivity to NO<sub>2</sub>. 2017 IEEE Sensor 1–3 (2017). <https://doi.org/10.1109/ICSENS.2017.8234283>
80. X. Chen, X. Chen, Y. Han, C. Su, M. Zeng et al., Two-dimensional MoSe<sub>2</sub> nanosheets via liquid-phase exfoliation for high-performance room temperature NO<sub>2</sub> gas sensors. *Nanotechnology* **30**(44), 445503 (2019). <https://doi.org/10.1088/1361-6528/ab35ec>
81. Y. Han, Y. Liu, C. Su, S. Wang, H. Li et al., Interface engineered WS<sub>2</sub>/ZnS heterostructures for sensitive and reversible NO<sub>2</sub> room temperature sensing. *Sens. Actuators B Chem.* **296**, 126666 (2019). <https://doi.org/10.1016/j.snb.2019.126666>
82. Z. Yang, C. Su, S. Wang, Y. Han, X. Chen et al., Highly sensitive NO<sub>2</sub> gas sensors based on hexagonal SnS<sub>2</sub> nanoplates operating at room temperature. *Nanotechnology* **31**(7), 075501 (2019). <https://doi.org/10.1088/1361-6528/ab5271>
83. R. Guo, Y. Han, C. Su, X. Chen, M. Zeng et al., Ultrasensitive room temperature NO<sub>2</sub> sensors based on liquid phase exfoliated WSe<sub>2</sub> nanosheets. *Sens. Actuators B Chem.* **300**, 127013 (2019). <https://doi.org/10.1016/j.snb.2019.127013>
84. S.S. Varghese, S.H. Varghese, S. Swaminathan, K.K. Singh, V. Mittal, Two-dimensional materials for sensing: graphene and beyond. *Electronics* **4**(3), 651–687 (2015). <https://doi.org/10.3390/electronics4030651>
85. M. Kumar, A.V. Agrawal, M. Moradi, R. Yousefi, Chapter 6 - Nanosensors for gas sensing applications, in eds. by A. Abdeltif, A.A. Assadi, P. Nguyen-Tri, et al., *Nanomaterials for Air Remediation* (Elsevier, 2020), pp. 107–130. <https://doi.org/10.1016/B978-0-12-818821-7.00006-3>
86. S. Yang, C. Jiang, S.-H. Wei, Gas sensing in 2D materials. *Appl. Phys. Rev.* **4**(2), 021304 (2017). <https://doi.org/10.1063/1.4983310>
87. K.Y. Ko, J.-G. Song, Y. Kim, T. Choi, S. Shin et al., Improvement of gas-sensing performance of large-area tungsten disulfide nanosheets by surface functionalization. *ACS Nano* **10**(10), 9287–9296 (2016). <https://doi.org/10.1021/acsnano.6b03631>
88. H. Fang, S. Chuang, T.C. Chang, K. Takei, T. Takahashi et al., High-performance single layered WSe<sub>2</sub> p-FETs with chemically doped contacts. *Nano Lett.* **12**(7), 3788–3792 (2012). <https://doi.org/10.1021/nl301702r>
89. Z. Feng, Y. Xie, J. Chen, Y. Yu, S. Zheng et al., Highly sensitive MoTe<sub>2</sub> chemical sensor with fast recovery rate through gate biasing. *2D Mater.* **4**(2), 025018 (2017). <https://doi.org/10.1021/nl301702r>



90. B. Cho, A.R. Kim, D.J. Kim, H.-S. Chung, S.Y. Choi et al., Two-dimensional atomic-layered alloy junctions for high-performance wearable chemical sensor. *ACS Appl. Mater. Interfaces* **8**(30), 19635–19642 (2016). <https://doi.org/10.1021/acsami.6b05943>
91. K.P. Gattu, K. Ghule, A.A. Kashale, V.B. Patil, D.M. Phase et al., Bio-green synthesis of Ni-doped tin oxide nanoparticles and its influence on gas sensing properties. *RSC Adv.* **5**(89), 72849–72856 (2015). <https://doi.org/10.1039/C5RA13513C>
92. D. Lembke, S. Bertolazzi, A. Kis, Single-layer MoS<sub>2</sub> electronics. *Acc. Chem. Res.* **48**(1), 100–110 (2015). <https://doi.org/10.1021/ar500274q>
93. P. Raybaud, J. Hafner, G. Kresse, S. Kasztelan, H. Toulhoat, Structure, energetics, and electronic properties of the surface of a promoted MoS<sub>2</sub> catalyst: an ab initio local density functional study. *J. Catal.* **190**(1), 128–143 (2000). <https://doi.org/10.1006/jcat.1999.2743>
94. W. Yin, J. Yu, F. Lv, L. Yan, L.R. Zheng et al., Functionalized nano-MoS<sub>2</sub> with peroxidase catalytic and near-infrared photothermal activities for safe and synergetic wound antibacterial applications. *ACS Nano* **10**(12), 11000–11011 (2016). <https://doi.org/10.1021/acsnano.6b05810>
95. G. Eda, T. Fujita, H. Yamaguchi, D. Voiry, M. Chen et al., Coherent atomic and electronic heterostructures of single-layer MoS<sub>2</sub>. *ACS Nano* **6**(8), 7311–7317 (2012). <https://doi.org/10.1021/nn302422x>
96. K. Kalantar-zadeh, J.Z. Ou, Biosensors based on two-dimensional MoS<sub>2</sub>. *ACS Sens.* **1**(1), 5–16 (2016). <https://doi.org/10.1021/acssensors.5b00142>
97. F. Wypych, R. Schöllhorn, 1T-MoS<sub>2</sub>, a new metallic modification of molybdenum disulfide. *J. Chem. Soc. Chem. Commun.* (1992). <https://doi.org/10.1039/C39920001386>
98. A. Splendiani, L. Sun, Y. Zhang, T. Li, J. Kim et al., Emerging photoluminescence in monolayer MoS<sub>2</sub>. *Nano Lett.* **10**(4), 1271–1275 (2010). <https://doi.org/10.1021/nl903868w>
99. G. Eda, H. Yamaguchi, D. Voiry, T. Fujita, M. Chen et al., Photoluminescence from chemically exfoliated MoS<sub>2</sub>. *Nano Lett.* **11**(12), 5111–5116 (2011). <https://doi.org/10.1021/nl201874w>
100. W. Zhao, R.M. Ribeiro, G. Eda, Electronic structure and optical signatures of semiconducting transition metal dichalcogenide nanosheets. *Acc. Chem. Res.* **48**(1), 91–99 (2015). <https://doi.org/10.1021/ar500303m>
101. S. Zhang, J. Liu, K.H. Ruiz, R. Tu, M. Yang et al., Morphological evolution of vertically standing molybdenum disulfide nanosheets by chemical vapor deposition. *Materials* **11**(4), 631 (2018). <https://doi.org/10.3390/ma11040631>
102. X. Liu, T. Xu, X. Wu, Z. Zhang, J. Yu et al., Top-down fabrication of sub-nanometre semiconducting nanoribbons derived from molybdenum disulfide sheets. *Nat. Commun.* **4**(1), 1776 (2013). <https://doi.org/10.1038/ncomms2803>
103. B. Cho, J. Yoon, S.K. Lim, A.R. Kim, D.-H. Kim et al., Chemical sensing of 2D Graphene/MoS<sub>2</sub> heterostructure device. *ACS Appl. Mater. Interfaces* **7**(30), 16775–16780 (2015). <https://doi.org/10.1021/acsami.5b04541>
104. Z. Yin, H. Li, H. Li, L. Jiang, Y. Shi et al., Single-layer MoS<sub>2</sub> phototransistors. *ACS Nano* **6**(1), 74–80 (2012). <https://doi.org/10.1021/nn2024557>
105. R. Ganatra, Q. Zhang, Few-layer MoS<sub>2</sub>: a promising layered semiconductor. *ACS Nano* **8**(5), 4074–4099 (2014). <https://doi.org/10.1021/nn405938z>
106. K. Kaasbjerg, K.S. Thygesen, K.W. Jacobsen, Phonon-limited mobility in n-type single-layer MoS<sub>2</sub> from first principles. *Phys. Rev. B* **85**(11), 115317 (2012). <https://doi.org/10.1103/PhysRevB.85.115317>
107. C. Lee, H. Yan, L.E. Brus, T.F. Heinz, J. Hone et al., Anomalous lattice vibrations of single- and few-layer MoS<sub>2</sub>. *ACS Nano* **4**(5), 2695–2700 (2010). <https://doi.org/10.1021/nn1003937>
108. A.V. Agrawal, N. Kumar, S. Venkatesan, A. Zakhidov, C. Manspecker et al., Controlled growth of MoS<sub>2</sub> flakes from in-plane to edge-enriched 3d network and their surface-energy studies. *ACS Appl. Nano Mater.* **1**(5), 2356–2367 (2018). <https://doi.org/10.1021/acsanm.8b00467>
109. B. Chakraborty, A. Bera, D.V.S. Muthu, S. Bhowmick, U.V. Waghmare et al., Symmetry-dependent phonon renormalization in monolayer MoS<sub>2</sub> transistor. *Phys. Rev. B* **85**(16), 161403 (2012). <https://doi.org/10.1103/PhysRevB.85.161403>
110. Y.K. Hong, G. Yoo, J. Kwon, S. Hong, W.G. Song et al., High performance and transparent multilayer MoS<sub>2</sub> transistors: tuning Schottky barrier characteristics. *AIP Adv.* **6**(5), 055026 (2016). <https://doi.org/10.1063/1.4953062>
111. S. Das, R. Gulotty, A.V. Sumant, A. Roelofs, All two-dimensional, flexible, transparent, and thinnest thin film transistor. *Nano Lett.* **14**(5), 2861–2866 (2014). <https://doi.org/10.1021/nl5009037>
112. Q. Zhang, W. Bao, A. Gong, T. Gong, D. Ma et al., A highly sensitive, highly transparent, gel-gated MoS<sub>2</sub> phototransistor on biodegradable nanopaper. *Nanoscale* **8**(29), 14237–14242 (2016). <https://doi.org/10.1039/C6NR01534D>
113. Z.-T. Shi, W. Kang, J. Xu, Y.-W. Sun, M. Jiang et al., Hierarchical nanotubes assembled from MoS<sub>2</sub>-carbon monolayer sandwiched superstructure nanosheets for high-performance sodium ion batteries. *Nano Energy* **22**, 27–37 (2016). <https://doi.org/10.1016/j.nanoen.2016.02.009>
114. J. Kang, H. Sahin, F.M. Peeters, Mechanical properties of monolayer sulphides: a comparative study between MoS<sub>2</sub>, HfS<sub>2</sub> and TiS<sub>3</sub>. *Phys. Chem. Chem. Phys.* **17**(41), 27742–27749 (2015). <https://doi.org/10.1039/C5CP04576B>
115. J. Pu, Y. Yomogida, K.-K. Liu, L.-J. Li, Y. Iwasa et al., Highly flexible MoS<sub>2</sub> thin-film transistors with ion gel dielectrics. *Nano Lett.* **12**(8), 4013–4017 (2012). <https://doi.org/10.1021/nl301335q>
116. B. Radisavljevic, A. Radenovic, J. Brivio, V. Giacometti, A. Kis, Single-layer MoS<sub>2</sub> transistors. *Nat. Nanotechnol.* **6**(3), 147–150 (2011). <https://doi.org/10.1038/nnano.2010.279>
117. Q. Yue, Z. Shao, S. Chang, J. Li, Adsorption of gas molecules on monolayer MoS<sub>2</sub> and effect of applied electric field. *Nanoscale Res. Lett.* **8**(1), 425 (2013). <https://doi.org/10.1186/1556-276x-8-425>



118. H. Long, A. Harley-Trochimczyk, T. Pham, Z. Tang, T. Shi et al., High surface area MoS<sub>2</sub>/graphene hybrid aerogel for ultrasensitive NO<sub>2</sub> detection. *Adv. Funct. Mater.* **26**(28), 5158–5165 (2016). <https://doi.org/10.1002/adfm.201601562>
119. R. Kumar, N. Goel, M. Kumar, UV-activated MoS<sub>2</sub> based fast and reversible NO<sub>2</sub> sensor at room temperature. *ACS Sens.* **2**(11), 1744–1752 (2017). <https://doi.org/10.1021/acssensors.7b00731>
120. A.V. Agrawal, R. Kumar, S. Venkatesan, A. Zakhidov, G. Yang et al., Photoactivated mixed in-plane and edge-enriched p-type MoS<sub>2</sub> flake-based NO<sub>2</sub> sensor working at room temperature. *ACS Sens.* **3**(5), 998–1004 (2018). <https://doi.org/10.1021/acssensors.8b00146>
121. Y. Zhou, C. Zou, X. Lin, Y. Guo, UV light activated NO<sub>2</sub> gas sensing based on Au nanoparticles decorated few-layer MoS<sub>2</sub> thin film at room temperature. *Appl. Phys. Lett.* **113**(8), 082103 (2018)
122. J. Guo, R. Wen, J. Zhai, Z.L. Wang, Enhanced NO<sub>2</sub> gas sensing of a single-layer MoS<sub>2</sub> by photogating and piezophototronic effects. *Sci. Bull.* **64**(2), 128–135 (2019). <https://doi.org/10.1016/j.scib.2018.12.009>
123. Y. Xia, C. Hu, S. Guo, L. Zhang, M. Wang et al., Sulfur-vacancy-enriched MoS<sub>2</sub> nanosheets based heterostructures for near-infrared optoelectronic NO<sub>2</sub> sensing. *ACS Appl. Nano Mater.* **3**(1), 665–673 (2020). <https://doi.org/10.1021/acsnm.9b02180>
124. J. Lu, J.H. Lu, H. Liu, B. Liu, L. Gong et al., Microlandscaping of Au nanoparticles on few-layer MoS<sub>2</sub> films for chemical sensing. *Small* **11**(15), 1792–1800 (2015). <https://doi.org/10.1002/sml.201402591>
125. A.J. Cohen, P. Mori-Sánchez, W. Yang, Challenges for density functional theory. *Chem. Rev.* **112**(1), 289–320 (2012). <https://doi.org/10.1021/cr200107z>
126. R.O. Jones, Density functional theory: its origins, rise to prominence, and future. *Rev. Mod. Phys.* **87**(3), 897–923 (2015). <https://doi.org/10.1103/RevModPhys.87.897>
127. S. Tang, Z. Cao, Adsorption of nitrogen oxides on graphene and graphene oxides: insights from density functional calculations. *J. Chem. Phys.* **134**(4), 044710 (2011). <https://doi.org/10.1063/1.3541249>
128. D.I. Son, B.W. Kwon, D.H. Park, W.-S. Seo, Y. Yi et al., Emissive ZnO-graphene quantum dots for white-light-emitting diodes. *Nat. Nanotechnol.* **7**(7), 465–471 (2012). <https://doi.org/10.1038/nnano.2012.71>
129. T.S. Sreerupasad, A.A. Rodriguez, J. Colston, A. Graham, E. Shishkin et al., Electron-tunneling modulation in percolating network of graphene quantum dots: fabrication, phenomenological understanding, and humidity/pressure sensing applications. *Nano Lett.* **13**(4), 1757–1763 (2013). <https://doi.org/10.1021/nl4003443>
130. L.-L. Li, J. Ji, R. Fei, C.-Z. Wang, Q. Lu et al., A facile microwave avenue to electrochemiluminescent two-color graphene quantum dots. *Adv. Funct. Mater.* **22**(14), 2971–2979 (2012). <https://doi.org/10.1002/adfm.201200166>
131. J. Kong, N.R. Franklin, C. Zhou, M.G. Chapline, S. Peng et al., Nanotube molecular wires as chemical sensors. *Science* **287**(5453), 622–625 (2000). <https://doi.org/10.1126/science.287.5453.622>
132. S. Chopra, K. McGuire, N. Gothard, A.M. Rao, A. Pham, Selective gas detection using a carbon nanotube sensor. *Appl. Phys. Lett.* **83**(11), 2280–2282 (2003). <https://doi.org/10.1063/1.1610251>
133. O.K. Varghese, D. Gong, M. Paulose, K.G. Ong, C.A. Grimes, Hydrogen sensing using titania nanotubes. *Sens. Actuators B Chem.* **93**(1), 338–344 (2003). [https://doi.org/10.1016/S0925-4005\(03\)00222-3](https://doi.org/10.1016/S0925-4005(03)00222-3)
134. S. Wang, D. Huang, S. Xu, W. Jiang, T. Wang et al., Two-dimensional NiO nanosheets with enhanced room temperature NO<sub>2</sub> sensing performance via Al doping. *Phys. Chem. Chem. Phys.* **19**(29), 19043–19049 (2017). <https://doi.org/10.1039/C7CP03259E>
135. X. Chen, S. Wang, C. Su, Y. Han, C. Zou et al., Two-dimensional Cd-doped porous Co<sub>3</sub>O<sub>4</sub> nanosheets for enhanced room-temperature NO<sub>2</sub> sensing performance. *Sens. Actuators B Chem.* **305**, 127393 (2020). <https://doi.org/10.1016/j.snb.2019.127393>
136. N. Huo, S. Yang, Z. Wei, S.-S. Li, J.-B. Xia et al., Photore sponsive and gas sensing field-effect transistors based on multilayer WS<sub>2</sub> nanoflakes. *Sci. Rep.* **4**(1), 5209 (2014). <https://doi.org/10.1038/srep05209>
137. B. Li, S. Yang, N. Huo, Y. Li, J. Yang et al., Growth of large area few-layer or monolayer MoS<sub>2</sub> from controllable MoO<sub>3</sub> nanowire nuclei. *RSC Adv.* **4**(50), 26407–26412 (2014). <https://doi.org/10.1039/C4RA01632G>
138. Y.-H. Zhang, Y.-B. Chen, K.-G. Zhou, C.-H. Liu, J. Zeng et al., Improving gas sensing properties of graphene by introducing dopants and defects: a first-principles study. *Nanotechnology* **20**(18), 185504 (2009). <https://doi.org/10.1088/0957-484/20/18/185504>
139. G. Liu, Y. Lin, Nanomaterial labels in electrochemical immunosensors and immunoassays. *Talanta* **74**(3), 308–317 (2007). <https://doi.org/10.1016/j.talanta.2007.10.014>
140. G. Aragay, F. Pino, A. Merkoçi, Nanomaterials for sensing and destroying pesticides. *Chem. Rev.* **112**(10), 5317–5338 (2012). <https://doi.org/10.1021/cr300020c>
141. D. Grieshaber, R. MacKenzie, J. Vörös, E. Reimhult, Electrochemical biosensors—sensor principles and architectures. *Sensors* **8**(3), 1400–1458 (2008). <https://doi.org/10.3390/s80314000>
142. K. Saha, S.S. Agasti, C. Kim, X. Li, V.M. Rotello, Gold nanoparticles in chemical and biological sensing. *Chem. Rev.* **112**(5), 2739–2779 (2012). <https://doi.org/10.1021/cr2001178>
143. C. Zou, J. Hu, Y. Su, F. Shao, Z. Tao et al., Three-dimensional Fe<sub>3</sub>O<sub>4</sub>@reduced graphene oxide heterojunctions for high-performance room-temperature NO<sub>2</sub> sensors. *Front. Mater.* **6**, 195 (2019). <https://doi.org/10.3389/fmats.2019.00195>
144. R. Kumar, O. Al-Dossary, G. Kumar, A. Umar, Zinc oxide nanostructures for NO<sub>2</sub> gas-sensor applications: a

- review. *Nano Micro Lett.* **7**(2), 97–120 (2015). <https://doi.org/10.1007/s40820-014-0023-3>
145. J. Xu, Y.A. Shun, Q. Pan, J. Qin, Sensing characteristics of double layer film of ZnO. *Sens. Actuators B Chem.* **66**(1), 161–163 (2000). [https://doi.org/10.1016/S0925-4005\(00\)00327-0](https://doi.org/10.1016/S0925-4005(00)00327-0)
146. J.-H. Kim, A. Mirzaei, H.W. Kim, S.S. Kim, Low-voltage-driven sensors based on ZnO nanowires for room-temperature detection of NO<sub>2</sub> and CO gases. *ACS Appl. Mater. Interfaces* **11**(27), 24172–24183 (2019). <https://doi.org/10.1021/acsami.9b07208>
147. J. Zhang, Z. Qin, D. Zeng, C. Xie, Metal-oxide-semiconductor based gas sensors: screening, preparation, and integration. *Phys. Chem. Chem. Phys.* **19**(9), 6313–6329 (2017). <https://doi.org/10.1039/C6CP07799D>
148. M.M. Arafat, A.S.M.A. Haseeb, S.A. Akbar, 13.08 - Developments in semiconducting oxide-based gas-sensing materials, in by eds. S. Hashmi, G.F. Batalha, C.J. Van Tyne, et al., *Comprehensive Materials Processing* (Elsevier, 2014), pp. 205–219. <https://doi.org/10.1016/B978-0-08-096532-1.01307-8>
149. V. Krivetsky, A. Ponzoni, E. Comini, M. Rumyantseva, A. Gaskov, Selective modified SnO<sub>2</sub>-based materials for gas sensors arrays. *Procedia Chem.* **1**(1), 204–207 (2009). <https://doi.org/10.1016/j.proche.2009.07.051>
150. E. Comini, G. Faglia, G. Sberveglieri, Z. Pan, Z.L. Wang, Stable and highly sensitive gas sensors based on semiconducting oxide nanobelts. *Appl. Phys. Lett.* **81**(10), 1869–1871 (2002). <https://doi.org/10.1063/1.1504867>
151. J. Hao, D. Zhang, Q. Sun, S. Zheng, J. Sun et al., Hierarchical SnS<sub>2</sub>/SnO<sub>2</sub> nanoheterojunctions with increased active-sites and charge transfer for ultrasensitive NO<sub>2</sub> detection. *Nanoscale* **10**(15), 7210–7217 (2018). <https://doi.org/10.1039/C8NR01379A>
152. M.D. Ganji, N. Sharifi, M. Ghorbanzadeh Ahangari, A. Khosravi, Density functional theory calculations of hydrogen molecule adsorption on monolayer molybdenum and tungsten disulfide. *Phys. E Low Dimens. Syst. Nanostruct.* **57**, 28–34 (2014). <https://doi.org/10.1016/j.physe.2013.10.039>
153. M. Hijazi, V. Stambouli, M. Rieu, G. Tournier, C. Pijolat et al., Sensitive and selective ammonia gas sensor based on molecularly modified SnO<sub>2</sub>. *Multidiscip. Digit. Publ. Inst. Proc.* **1**(4), 399 (2017). <https://doi.org/10.3390/proceedings1040399>
154. Y. Zhong, W. Li, X. Zhao, X. Jiang, S. Lin et al., High-response room-temperature NO<sub>2</sub> sensor and ultrafast humidity sensor based on SnO<sub>2</sub> with rich oxygen vacancy. *ACS Appl. Mater. Interfaces* **11**(14), 13441–13449 (2019). <https://doi.org/10.1021/acsami.9b01737>
155. T. Zhang, S. Mubeen, N.V. Myung, M.A. Deshusses, Recent progress in carbon nanotube-based gas sensors. *Nanotechnology* **19**(33), 332001 (2008). <https://doi.org/10.1088/0957-4484/19/33/332001>
156. H. Choi, J.S. Choi, J.-S. Kim, J.-H. Choe, K.H. Chung et al., Flexible and transparent gas molecule sensor integrated with sensing and heating graphene layers. *Small* **10**(18), 3685–3691 (2014). <https://doi.org/10.1002/sml.201400434>
157. Z. Zanolli, J.C. Charlier, Defective carbon nanotubes for single-molecule sensing. *Phys. Rev. B* **80**(15), 155447 (2009). <https://doi.org/10.1103/PhysRevB.80.155447>
158. S. Santucci, S. Picozzi, F.D. Gregorio, L. Lozzi, C. Cantalini et al., NO<sub>2</sub> and CO gas adsorption on carbon nanotubes: Experiment and theory. *J. Chem. Phys.* **119**(20), 10904–10910 (2003). <https://doi.org/10.1063/1.1619948>
159. H. Xu, X. Chen, J. Zhang, J. Wang, B. Cao et al., NO<sub>2</sub> gas sensing with SnO<sub>2</sub>-ZnO/PANI composite thick film fabricated from porous nanosolid. *Sens. Actuators B Chem.* **176**, 166–173 (2013). <https://doi.org/10.1016/j.snb.2012.09.060>
160. J. Zhang, S. Wang, Y. Wang, Y. Wang, B. Zhu et al., NO<sub>2</sub> sensing performance of SnO<sub>2</sub> hollow-sphere sensor. *Sens. Actuators B Chem.* **135**(2), 610–617 (2009). <https://doi.org/10.1016/j.snb.2008.09.026>
161. Y. Xiao, Q. Yang, Z. Wang, R. Zhang, Y. Gao et al., Improvement of NO<sub>2</sub> gas sensing performance based on discoid tin oxide modified by reduced graphene oxide. *Sens. Actuators B Chem.* **227**, 419–426 (2016). <https://doi.org/10.1016/j.snb.2015.11.051>
162. M. Kumar, A. Kumar, A.C. Abhyankar, Influence of texture coefficient on surface morphology and sensing properties of W-doped nanocrystalline tin oxide thin films. *ACS Appl. Mater. Interfaces* **7**(6), 3571–3580 (2015). <https://doi.org/10.1021/am507397z>
163. Y.-J. Choi, I.-S. Hwang, J.-G. Park, K.J. Choi, J.-H. Park et al., Novel fabrication of a SnO<sub>2</sub> nanowire gas sensor with high sensitivity. *Nanotechnology* **19**(9), 095508 (2008). <https://doi.org/10.1088/0957-4484/19/9/095508>
164. W.-S. Kim, B.-S. Lee, D.-H. Kim, H.-C. Kim, W.-R. Yu et al., SnO<sub>2</sub> nanotubes fabricated using electrospinning and atomic layer deposition and their gas sensing performance. *Nanotechnology* **21**(24), 245605 (2010). <https://doi.org/10.1088/0957-4484/21/24/245605>
165. R. Leghrib, A. Felten, J.J. Pireaux, E. Llobet, Gas sensors based on doped-CNT/SnO<sub>2</sub> composites for NO<sub>2</sub> detection at room temperature. *Thin Solid Films* **520**(3), 966–970 (2011). <https://doi.org/10.1016/j.tsf.2011.04.186>
166. Z. Wang, Y. Zhang, S. Liu, T. Zhang, Preparation of Ag nanoparticles-SnO<sub>2</sub> nanoparticles-reduced graphene oxide hybrids and their application for detection of NO<sub>2</sub> at room temperature. *Sens. Actuators B Chem.* **222**, 893–903 (2016). <https://doi.org/10.1016/j.snb.2015.09.027>
167. S.H. Mohamed, SnO<sub>2</sub> dendrites-nanowires for optoelectronic and gas sensing applications. *J. Alloys Compd.* **510**(1), 119–124 (2012). <https://doi.org/10.1016/j.jallcom.2011.09.006>
168. S. Liu, Z. Wang, Y. Zhang, J. Li, T. Zhang, Sulfonated graphene anchored with tin oxide nanoparticles for detection of nitrogen dioxide at room temperature with enhanced sensing performances. *Sens. Actuators B Chem.* **228**, 134–143 (2016). <https://doi.org/10.1016/j.snb.2016.01.023>
169. Z. Zhang, M. Xu, L. Liu, X. Ruan, J. Yan et al., Novel SnO<sub>2</sub>@ZnO hierarchical nanostructures for highly sensitive and selective NO<sub>2</sub> gas sensing. *Sens. Actuators B Chem.* **257**, 714–727 (2018). <https://doi.org/10.1016/j.snb.2017.10.190>



170. V.V. Quang, N.V. Dung, N.S. Trong, N.D. Hoa, N.V. Duy et al., Outstanding gas-sensing performance of graphene/SnO<sub>2</sub> nanowire Schottky junctions. *Appl. Phys. Lett.* **105**(1), 013107 (2014). <https://doi.org/10.1063/1.4887486>
171. A. Sharma, M. Tomar, V. Gupta, WO<sub>3</sub> nanoclusters–SnO<sub>2</sub> film gas sensor heterostructure with enhanced response for NO<sub>2</sub>. *Sens. Actuators B Chem.* **176**, 675–684 (2013). <https://doi.org/10.1016/j.snb.2012.09.094>
172. J.-H. Kim, A. Katoch, S.-H. Kim, S.S. Kim, Chemiresistive sensing behavior of SnO<sub>2</sub> (n)–Cu<sub>2</sub>O (p) core–shell nanowires. *ACS Appl. Mater. Interfaces* **7**(28), 15351–15358 (2015). <https://doi.org/10.1021/acsami.5b03224>
173. J. Sun, P. Sun, D. Zhang, J. Xu, X. Liang et al., Growth of SnO<sub>2</sub> nanowire arrays by ultrasonic spray pyrolysis and their gas sensing performance. *RSC Adv.* **4**(82), 43429–43435 (2014). <https://doi.org/10.1039/C4RA05682E>
174. Y.J. Kwon, S.Y. Kang, P. Wu, Y. Peng, S.S. Kim et al., Selective improvement of NO<sub>2</sub> gas sensing behavior in SnO<sub>2</sub> nanowires by ion-beam irradiation. *ACS Appl. Mater. Interfaces* **8**(21), 13646–13658 (2016). <https://doi.org/10.1021/acsami.6b01619>
175. J.Z. Ou, W. Ge, B. Carey, T. Daeneke, A. Rotbart et al., Physisorption-based charge transfer in two-dimensional SnS<sub>2</sub> for selective and reversible NO<sub>2</sub> gas sensing. *ACS Nano* **9**(10), 10313–10323 (2015). <https://doi.org/10.1021/acs.nano.5b04343>
176. T. Wang, J. Hao, S. Zheng, Q. Sun, D. Zhang et al., Highly sensitive and rapidly responding room-temperature NO<sub>2</sub> gas sensors based on WO<sub>3</sub> nanorods/sulfonated graphene nanocomposites. *Nano Res.* **11**(2), 791–803 (2018). <https://doi.org/10.1007/s12274-017-1688-y>
177. H.W. Kim, H.G. Na, Y.J. Kwon, S.Y. Kang, M.S. Choi et al., Microwave-assisted synthesis of graphene–SnO<sub>2</sub> nanocomposites and their applications in gas sensors. *ACS Appl. Mater. Interfaces* **9**(37), 31667–31682 (2017). <https://doi.org/10.1021/acsami.7b02533>
178. J. Partridge, M. Field, J. Peng, A. Sadek, K. Kalantar-Zadeh et al., Nanostructured SnO<sub>2</sub> films prepared from evaporated Sn and their application as gas sensors. *Nanotechnology* **19**(12), 125504 (2008). <https://doi.org/10.1088/0957-4484/19/12/125504>
179. S. Liu, Z. Wang, Y. Zhang, C. Zhang, T. Zhang, High performance room temperature NO<sub>2</sub> sensors based on reduced graphene oxide-multiwalled carbon nanotubes-tin oxide nanoparticles hybrids. *Sens. Actuators B Chem.* **211**, 318–324 (2015). <https://doi.org/10.1016/j.snb.2015.01.127>
180. H. Zhang, Y. Wang, X. Zhu, Y. Li, W. Cai, Bilayer Au nanoparticle-decorated WO<sub>3</sub> porous thin films: on-chip fabrication and enhanced NO<sub>2</sub> gas sensing performances with high selectivity. *Sens. Actuators B Chem.* **280**, 192–200 (2019). <https://doi.org/10.1016/j.snb.2018.10.065>
181. I. Kortidis, H.C. Swart, S.S. Ray, D.E. Motaung, Characteristics of point defects on the room temperature ferromagnetic and highly NO<sub>2</sub> selectivity gas sensing of p-type Mn<sub>3</sub>O<sub>4</sub> nanorods. *Sens. Actuators B Chem.* **285**, 92–107 (2019). <https://doi.org/10.1016/j.snb.2019.01.007>
182. S. Zhao, Y. Shen, P. Zhou, X. Zhong, C. Han et al., Design of Au@WO<sub>3</sub> core–shell structured nanospheres for ppb-level NO<sub>2</sub> sensing. *Sens. Actuators B Chem.* **282**, 917–926 (2019). <https://doi.org/10.1016/j.snb.2018.11.142>
183. Y.H. Navale, S.T. Navale, F.J. Stadler, N.S. Ramgir, V.B. Patil, Enhanced NO<sub>2</sub> sensing aptness of ZnO nanowire/CuO nanoparticle heterostructure-based gas sensors. *Ceram. Int.* **45**(2, Part A), 1513–1522 (2019). <https://doi.org/10.1016/j.ceramint.2018.10.022>
184. Y. Song, F. Chen, Y. Zhang, S. Zhang, F. Liu et al., Fabrication of highly sensitive and selective room-temperature nitrogen dioxide sensors based on the ZnO nanoflowers. *Sens. Actuators B Chem.* **287**, 191–198 (2019). <https://doi.org/10.1016/j.snb.2019.01.146>
185. R.K. Sonker, B.C. Yadav, V. Gupta, M. Tomar, Fabrication and characterization of ZnO-TiO<sub>2</sub>-PANI (ZTP) micro/nanoballs for the detection of flammable and toxic gases. *J. Hazard. Mater.* **370**, 126–137 (2019). <https://doi.org/10.1016/j.jhazmat.2018.10.016>
186. H.-Y. Lee, Y.-C. Heish, C.-T. Lee, High sensitivity detection of nitrogen oxide gas at room temperature using zinc oxide-reduced graphene oxide sensing membrane. *J. Alloys Compd.* **773**, 950–954 (2019). <https://doi.org/10.1016/j.jallcom.2018.09.290>
187. M.S. Choi, J.H. Bang, A. Mirzaei, W. Oum, H.G. Na et al., Promotional effects of ZnO-branching and Au-functionalization on the surface of SnO<sub>2</sub> nanowires for NO<sub>2</sub> sensing. *J. Alloys Compd.* **786**, 27–39 (2019). <https://doi.org/10.1016/j.jallcom.2019.01.311>
188. H. Ma, L. Yu, X. Yuan, Y. Li, C. Li et al., Room temperature photoelectric NO<sub>2</sub> gas sensor based on direct growth of walnut-like In<sub>2</sub>O<sub>3</sub> nanostructures. *J. Alloys Compd.* **782**, 1121–1126 (2019). <https://doi.org/10.1016/j.jallcom.2018.12.180>
189. A. Giampiccolo, D.M. Tobaldi, S.G. Leonardi, B.J. Murdoch, M.P. Seabra et al., Sol gel graphene/TiO<sub>2</sub> nanoparticles for the photocatalytic-assisted sensing and abatement of NO<sub>2</sub>. *Appl. Catal. B Environ.* **243**, 183–194 (2019). <https://doi.org/10.1016/j.apcatb.2018.10.032>
190. M. Penza, R. Rossi, M. Alvisi, G. Cassano, M.A. Signore et al., Pt- and Pd-nanoclusters functionalized carbon nanotubes networked films for sub-ppm gas sensors. *Sens. Actuators B Chem.* **135**(1), 289–297 (2008). <https://doi.org/10.1016/j.snb.2008.08.024>
191. M.G. Chung, D.H. Kim, H.M. Lee, T. Kim, J.H. Choi et al., Highly sensitive NO<sub>2</sub> gas sensor based on ozone treated graphene. *Sens. Actuators B Chem.* **166–167**, 172–176 (2012). <https://doi.org/10.1016/j.snb.2012.02.036>
192. H.Y. Jeong, D.-S. Lee, H.K. Choi, D.H. Lee, J.-E. Kim et al., Flexible room-temperature NO<sub>2</sub> gas sensors based on carbon nanotubes/reduced graphene hybrid films. *Appl. Phys. Lett.* **96**(21), 213105 (2010). <https://doi.org/10.1063/1.3432446>
193. H. Zhang, Q. Li, J. Huang, Y. Du, S.C. Ruan, Reduced graphene oxide/Au nanocomposite for NO<sub>2</sub> sensing at low operating temperature. *Sensors* **16**(7), 1152 (2016). <https://doi.org/10.3390/s16071152>



194. X. Liu, J. Cui, J. Sun, X. Zhang, 3D graphene aerogel-supported SnO<sub>2</sub> nanoparticles for efficient detection of NO<sub>2</sub>. *RSC Adv.* **4**(43), 22601–22605 (2014). <https://doi.org/10.1039/C4RA02453B>
195. A. Aziz, N. Tiwale, S.A. Hodge, S.J. Attwood, G. Divitini et al., Core-shell electrospun polycrystalline ZnO nanofibers for ultra-sensitive NO<sub>2</sub> Gas sensing. *ACS Appl. Mater. Interfaces* **10**(50), 43817–43823 (2018). <https://doi.org/10.1021/acsami.8b17149>
196. N. Ramgir, R. Bhusari, N.S. Rawat, S.J. Patil, A.K. Debnath et al., TiO<sub>2</sub>/ZnO heterostructure nanowire based NO<sub>2</sub> sensor. *Mater. Sci. Semicond. Process.* **106**, 104770 (2020). <https://doi.org/10.1016/j.mssp.2019.104770>
197. A. Sharma, M. Tomar, V. Gupta, Room temperature trace level detection of NO<sub>2</sub> gas using SnO<sub>2</sub> modified carbon nanotubes based sensor. *J. Mater. Chem.* **22**(44), 23608–23616 (2012). <https://doi.org/10.1039/C2JM35172B>
198. M.-W. Ahn, K.-S. Park, J.-H. Heo, J.-G. Park, D.-W. Kim et al., Gas sensing properties of defect-controlled ZnO-nanowire gas sensor. *Appl. Phys. Lett.* **93**(26), 263103 (2008). <https://doi.org/10.1063/1.3046726>
199. M.W. Ahn, K.S. Park, J.H. Heo, D.W. Kim, K.J. Choi et al., On-chip fabrication of ZnO-nanowire gas sensor with high gas sensitivity. *Sens. Actuators B Chem.* **138**(1), 168–173 (2009). <https://doi.org/10.1016/j.snb.2009.02.008>
200. H. Zhang, J. Feng, T. Fei, S. Liu, T. Zhang, SnO<sub>2</sub> nanoparticles-reduced graphene oxide nanocomposites for NO<sub>2</sub> sensing at low operating temperature. *Sens. Actuators B Chem.* **190**, 472–478 (2014). <https://doi.org/10.1016/j.snb.2013.08.067>
201. S. Srivastava, K. Jain, V.N. Singh, S. Singh, N. Vijayan et al., Faster response of NO<sub>2</sub> sensing in graphene-WO<sub>3</sub> nanocomposites. *Nanotechnology* **23**(20), 205501 (2012). <https://doi.org/10.1088/0957-4484/23/20/205501>
202. N.G. Cho, D.J. Yang, M.-J. Jin, H.-G. Kim, H.L. Tuller et al., Highly sensitive SnO<sub>2</sub> hollow nanofiber-based NO<sub>2</sub> gas sensors. *Sens. Actuators B Chem.* **160**(1), 1468–1472 (2011). <https://doi.org/10.1016/j.snb.2011.07.035>
203. J. Zhang, S. Wang, Y. Wang, M. Xu, H. Xia et al., ZnO hollow spheres: preparation, characterization, and gas sensing properties. *Sens. Actuators B Chem.* **139**(2), 411–417 (2009). <https://doi.org/10.1016/j.snb.2009.03.014>
204. E. Oh, H.-Y. Choi, S.-H. Jung, S. Cho, J.C. Kim et al., High-performance NO<sub>2</sub> gas sensor based on ZnO nanorod grown by ultrasonic irradiation. *Sens. Actuators B Chem.* **141**(1), 239–243 (2009). <https://doi.org/10.1016/j.snb.2009.06.031>
205. J.H. Jun, J. Yun, K. Cho, I.-S. Hwang, J.-H. Lee et al., Necked ZnO nanoparticle-based NO<sub>2</sub> sensors with high and fast response. *Sens. Actuators B Chem.* **140**(2), 412–417 (2009). <https://doi.org/10.1016/j.snb.2009.05.019>
206. Z.U. Abideen, A. Katoch, J.-H. Kim, Y.J. Kwon, H.W. Kim et al., Excellent gas detection of ZnO nanofibers by loading with reduced graphene oxide nanosheets. *Sens. Actuators B Chem.* **221**, 1499–1507 (2015). <https://doi.org/10.1016/j.snb.2015.07.120>
207. R.K. Sonker, S.R. Sabhajeet, S. Singh, B.C. Yadav, Synthesis of ZnO nanopetals and its application as NO<sub>2</sub> gas sensor. *Mater. Lett.* **152**, 189–191 (2015). <https://doi.org/10.1016/j.matlet.2015.03.112>
208. X. Chen, Y. Shen, P. Zhou, S. Zhao, X. Zhong et al., NO<sub>2</sub> sensing properties of one-pot-synthesized ZnO nanowires with Pd functionalization. *Sens. Actuators B Chem.* **280**, 151–161 (2019). <https://doi.org/10.1016/j.snb.2018.10.063>
209. V. Kruefu, A. Wisitorsaat, A. Tuantranont, S. Phanichphant, Gas sensing properties of conducting polymer/Au-loaded ZnO nanoparticle composite materials at room temperature. *Nanoscale Res. Lett.* **9**(1), 467–467 (2014). <https://doi.org/10.1186/1556-276X-9-467>
210. A.V. Kolobov, J. Tominaga, From 3D to 2D: fabrication methods. *Two-Dimensional Transition-Metal Dichalcogenides* (Springer International Publishing, 2016), pp. 79–107. [https://doi.org/10.1007/978-3-319-31450-1\\_4](https://doi.org/10.1007/978-3-319-31450-1_4)
211. J.N. Coleman, M. Lotya, A. O'Neill, S.D. Bergin, P.J. King et al., Two-dimensional nanosheets produced by liquid exfoliation of layered materials. *Science* **331**(6017), 568–571 (2011). <https://doi.org/10.1126/science.1194975>
212. R.-L. Chu, G.-B. Liu, W. Yao, X. Xu, D. Xiao et al., Spin-orbit-coupled quantum wires and Majorana fermions on zigzag edges of monolayer transition-metal dichalcogenides. *Phys. Rev. B* **89**(15), 155317 (2014). <https://doi.org/10.1103/PhysRevB.89.155317>
213. K. Lee, R. Gatensby, N. McEvoy, T. Hallam, G.S. Duesberg, High-performance sensors based on molybdenum disulfide thin films. *Adv. Mater.* **25**(46), 6699–6702 (2013). <https://doi.org/10.1002/adma.201303230>
214. R. Kumar, N. Goel, M. Kumar, High performance NO<sub>2</sub> sensor using MoS<sub>2</sub> nanowires network. *Appl. Phys. Lett.* **112**(5), 053502 (2018). <https://doi.org/10.1063/1.5019296>
215. M.A. Lukowski, A.S. Daniel, F. Meng, A. Forticaux, L. Li et al., Enhanced hydrogen evolution catalysis from chemically exfoliated metallic MoS<sub>2</sub> nanosheets. *J. Am. Chem. Soc.* **135**(28), 10274–10277 (2013). <https://doi.org/10.1021/ja404523s>
216. R. Kappera, D. Voiry, S.E. Yalcin, B. Branch, G. Gupta et al., Phase-engineered low-resistance contacts for ultrathin MoS<sub>2</sub> transistors. *Nat. Mater.* **13**(12), 1128–1134 (2014). <https://doi.org/10.1038/nmat4080>
217. R. Kappera, D. Voiry, S.E. Yalcin, W. Jen, M. Acerce et al., Metallic 1T phase source/drain electrodes for field effect transistors from chemical vapor deposited MoS<sub>2</sub>. *APL Mater.* **2**(9), 092516 (2014). <https://doi.org/10.1063/1.4896077>
218. F.K. Perkins, A.L. Friedman, E. Cobas, P.M. Campbell, G.G. Jernigan et al., Chemical vapor sensing with monolayer MoS<sub>2</sub>. *Nano Lett.* **13**(2), 668–673 (2013). <https://doi.org/10.1021/nl3043079>
219. S. Tongay, J. Zhou, C. Ataca, J. Liu, J.S. Kang et al., Broad-range modulation of light emission in two-dimensional semiconductors by molecular physisorption gating. *Nano Lett.* **13**, 2831–2836 (2013). <https://doi.org/10.1021/nl401117z>
220. Z. Lin, Y. Zhao, C. Zhou, R. Zhong, X. Wang et al., Controllable growth of large-size crystalline MoS<sub>2</sub> and resist-free

- transfer assisted with a Cu thin film. *Sci. Rep.* **5**(1), 18596 (2015). <https://doi.org/10.1038/srep18596>
221. L. Zhan, W. Wan, Z. Zhu, Y. Xu, T.-M. Shih et al., Centimeter-scale nearly single-crystal monolayer MoS<sub>2</sub> via self-limiting vapor deposition epitaxy. *J. Phys. Chem. C* **121**(8), 4703–4707 (2017). <https://doi.org/10.1021/acs.jpcc.6b12785>
222. A.S. Pawbake, M.S. Pawar, S.R. Jadhkar, D.J. Late, Large area chemical vapor deposition of monolayer transition metal dichalcogenides and their temperature dependent Raman spectroscopy studies. *Nanoscale* **8**(5), 3008–3018 (2016). <https://doi.org/10.1039/C5NR07401K>
223. X. Ling, Y.-H. Lee, Y. Lin, W. Fang, L. Yu et al., Role of the seeding promoter in MoS<sub>2</sub> growth by chemical vapor deposition. *Nano Lett.* **14**(2), 464–472 (2014). <https://doi.org/10.1021/nl4033704>
224. H. Schmidt, S. Wang, L. Chu, M. Toh, R. Kumar et al., Transport properties of monolayer MoS<sub>2</sub> grown by chemical vapor deposition. *Nano Lett.* **14**(4), 1909–1913 (2014). <https://doi.org/10.1021/nl4046922>
225. S. Wu, C. Huang, G. Aivazian, J.S. Ross, D.H. Cobden et al., Vapor–solid growth of high optical quality MoS<sub>2</sub> monolayers with near-unity valley polarization. *ACS Nano* **7**(3), 2768–2772 (2013). <https://doi.org/10.1021/nn4002038>
226. J. Shi, D. Ma, G.-F. Han, Y. Zhang, Q. Ji et al., Controllable growth and transfer of monolayer MoS<sub>2</sub> on Au foils and its potential application in hydrogen evolution reaction. *ACS Nano* **8**(10), 10196–10204 (2014). <https://doi.org/10.1021/nl503211t>
227. H. Ago, H. Endo, P. Solís-Fernández, R. Takizawa, Y. Ohta et al., Controlled van der Waals epitaxy of monolayer MoS<sub>2</sub> triangular domains on graphene. *ACS Appl. Mater. Interfaces* **7**(9), 5265–5273 (2015). <https://doi.org/10.1021/am508569m>
228. J. Zhang, H. Yu, W. Chen, X. Tian, D. Liu et al., Scalable growth of high-quality polycrystalline MoS<sub>2</sub> monolayers on SiO<sub>2</sub> with tunable grain sizes. *ACS Nano* **8**(6), 6024–6030 (2014). <https://doi.org/10.1021/nn5020819>
229. S. Najmaei, J. Yuan, J. Zhang, P. Ajayan, J. Lou, Synthesis and defect investigation of two-dimensional molybdenum disulfide atomic layers. *Acc. Chem. Res.* **48**(1), 31–40 (2015). <https://doi.org/10.1021/ar500291j>
230. L. Zhang, K. Liu, A.B. Wong, J. Kim, X. Hong et al., Three-dimensional spirals of atomic layered MoS<sub>2</sub>. *Nano Lett.* **14**(11), 6418–6423 (2014). <https://doi.org/10.1021/nl502961e>
231. L. Chen, B. Liu, M. Ge, Y. Ma, A.N. Abbas et al., Step-edge-guided nucleation and growth of aligned WSe<sub>2</sub> on sapphire via a layer-over-layer growth mode. *ACS Nano* **9**(8), 8368–8375 (2015). <https://doi.org/10.1021/acsnano.5b03043>
232. A. Roy, R. Ghosh, A. Rai, A. Sanne, K. Kim et al., Intradomain periodic defects in monolayer MoS<sub>2</sub>. *Appl. Phys. Lett.* **110**(20), 201905 (2017). <https://doi.org/10.1063/1.4983789>
233. X. Zeng, H. Hirwa, M. Ortel, H.C. Nerl, V. Nicolosi et al., Growth of large sized two-dimensional MoS<sub>2</sub> flakes in aqueous solution. *Nanoscale* **9**(19), 6575–6580 (2017). <https://doi.org/10.1039/C7NR00701A>
234. A. O’Neill, U. Khan, J.N. Coleman, Preparation of high concentration dispersions of exfoliated MoS<sub>2</sub> with increased Flake Size. *Chem. Mater.* **24**(12), 2414–2421 (2012). <https://doi.org/10.1021/cm301515z>
235. N. Liu, P. Kim, J.H. Kim, J.H. Ye, S. Kim et al., Large-area atomically thin MoS<sub>2</sub> nanosheets prepared using electrochemical exfoliation. *ACS Nano* **8**(7), 6902–6910 (2014). <https://doi.org/10.1021/nn5016242>
236. Z. Dai, W. Jin, M. Grady, J.T. Sadowski, J.I. Dadap et al., Surface structure of bulk 2H-MoS<sub>2</sub>(0001) and exfoliated suspended monolayer MoS<sub>2</sub>: a selected area low energy electron diffraction study. *Surf. Sci.* **660**, 16–21 (2017). <https://doi.org/10.1016/j.susc.2017.02.005>
237. D.L.C. Ky, B.-C. Tran Khac, C.T. Le, Y.S. Kim, K.-H. Chung, Friction characteristics of mechanically exfoliated and CVD-grown single-layer MoS<sub>2</sub>. *Friction* **6**(4), 395–406 (2018). <https://doi.org/10.1007/s40544-017-0172-8>
238. G.Z. Magda, J. Pető, G. Dobrik, C. Hwang, L.P. Biró et al., Exfoliation of large-area transition metal chalcogenide single layers. *Sci. Rep.* **5**(1), 14714 (2015). <https://doi.org/10.1038/srep14714>
239. Y.-K. Huang, J.D. Cain, L. Peng, S. Hao, T. Chasapis et al., Evaporative thinning: a facile synthesis method for high quality ultrathin layers of 2D crystals. *ACS Nano* **8**(10), 10851–10857 (2014). <https://doi.org/10.1021/nn504664p>
240. D. Kong, H. Wang, J.J. Cha, M. Pasta, K.J. Koski et al., Synthesis of MoS<sub>2</sub> and MoSe<sub>2</sub> films with vertically aligned layers. *Nano Lett.* **13**(3), 1341–1347 (2013). <https://doi.org/10.1021/nl400258t>
241. M.V. Bollinger, J.V. Lauritsen, K.W. Jacobsen, J.K. Nørskov, S. Helveg et al., One-dimensional metallic edge states in MoS. *Phys. Rev. Lett.* **87**(19), 196803 (2001). <https://doi.org/10.1103/PhysRevLett.87.196803>
242. W. Zhou, X. Zou, S. Najmaei, Z. Liu, Y. Shi et al., Intrinsic structural defects in monolayer molybdenum disulfide. *Nano Lett.* **13**(6), 2615–2622 (2013). <https://doi.org/10.1021/nl4007479>
243. K.F. Mak, K. He, C. Lee, G.H. Lee, J. Hone et al., Tightly bound trions in monolayer MoS<sub>2</sub>. *Nat. Mater.* **12**(3), 207–211 (2013). <https://doi.org/10.1038/nmat3505>
244. S. Mouri, Y. Miyauchi, K. Matsuda, Tunable photoluminescence of monolayer MoS<sub>2</sub> via chemical doping. *Nano Lett.* **13**(12), 5944–5948 (2013). <https://doi.org/10.1021/nl403036h>
245. A.K.M. Newaz, D. Prasai, J.I. Ziegler, D. Caudel, S. Robinson et al., Electrical control of optical properties of monolayer MoS<sub>2</sub>. *Solid State Commun.* **155**, 49–52 (2013). <https://doi.org/10.1016/j.ssc.2012.11.010>
246. H. Nan, Z. Wang, W. Wang, Z. Liang, Y. Lu et al., Strong photoluminescence enhancement of MoS<sub>2</sub> through defect engineering and oxygen bonding. *ACS Nano* **8**(6), 5738–5745 (2014). <https://doi.org/10.1021/nn500532f>
247. S. Tongay, J. Zhou, C. Ataca, J. Liu, J.S. Kang et al., Broad-range modulation of light emission in two-dimensional semiconductors by molecular physisorption gating. *Nano*

- Lett. **13**(6), 2831–2836 (2013). <https://doi.org/10.1021/nl4011172>
248. G. Finkelstein, H. Shtrikman, I. Bar-Joseph, Optical spectroscopy of a two-dimensional electron gas near the metal-insulator transition. *Phys. Rev. Lett.* **74**(6), 976–979 (1995). <https://doi.org/10.1103/PhysRevLett.74.976>
249. A.V. Agrawal, K. Kaur, M. Kumar, Interfacial study of vertically aligned n-type MoS<sub>2</sub> flakes heterojunction with p-type Cu-Zn-Sn-S for self-powered, fast and high performance broadband photodetector. *Appl. Surf. Sci.* **514**, 145901 (2020). <https://doi.org/10.1016/j.apsusc.2020.145901>
250. T.F. Jaramillo, K.P. Jørgensen, J. Bonde, J.H. Nielsen, S. Horch et al., Identification of active edge sites for electrochemical H<sub>2</sub> evolution from MoS<sub>2</sub> nanocatalysts. *Science* **317**(5834), 100–102 (2007). <https://doi.org/10.1126/science.1141483>
251. C. Kim, J.-C. Park, S. Y. Choi, Y. Kim, S.-Y. Seo et al., Self-formed channel devices based on vertically grown 2d materials with large-surface-area and their potential for chemical sensor applications. *Small* **14**(15), 1704116 (2018). <https://doi.org/10.1002/sml.201704116>
252. Y.-S. Shim, K.C. Kwon, J.M. Suh, K.S. Choi, Y.G. Song et al., Synthesis of numerous edge sites in MoS<sub>2</sub> via SiO<sub>2</sub> nanorods platform for highly sensitive gas sensor. *ACS Appl. Mater. Interfaces* **10**(37), 31594–31602 (2018). <https://doi.org/10.1021/acsami.8b08114>
253. J. Kibsgaard, Z. Chen, B.N. Reinecke, T.F. Jaramillo, Engineering the surface structure of MoS<sub>2</sub> to preferentially expose active edge sites for electrocatalysis. *Nat. Mater.* **11**(11), 963–969 (2012). <https://doi.org/10.1038/nmat3439>
254. L. Yang, H. Hong, Q. Fu, Y. Huang, J. Zhang et al., Single-crystal atomic-layered molybdenum disulfide nanobelts with high surface activity. *ACS Nano* **9**(6), 6478–6483 (2015). <https://doi.org/10.1021/acs.nano.5b02188>
255. A.V. Agrawal, R. Kumar, S. Venkatesan, A. Zakhidov, Z. Zhu et al., Fast detection and low power hydrogen sensor using edge-oriented vertically aligned 3-D network of MoS<sub>2</sub> flakes at room temperature. *Appl. Phys. Lett.* **111**(9), 093102 (2017). <https://doi.org/10.1063/1.5000825>
256. A. Singh, M.A. Uddin, T. Sudarshan, G. Koley, Tunable reverse-biased graphene/silicon heterojunction Schottky diode sensor. *Small* **10**(8), 1555–1565 (2014). <https://doi.org/10.1002/sml.201302818>
257. M.A. Uddin, A.K. Singh, T.S. Sudarshan, G. Koley, Functionalized graphene/silicon chemi-diode H<sub>2</sub> sensor with tunable sensitivity. *Nanotechnology* **25**(12), 125501 (2014). <https://doi.org/10.1088/0957-4484/25/12/125501>
258. A.N. Abbas, B. Liu, L. Chen, Y. Ma, S. Cong et al., Black phosphorus gas sensors. *ACS Nano* **9**(5), 5618–5624 (2015). <https://doi.org/10.1021/acs.nano.5b01961>
259. Y. Xu, C. Cheng, S. Du, J. Yang, B. Yu et al., Contacts between two- and three-dimensional materials: ohmic, Schottky, and p–n heterojunctions. *ACS Nano* **10**(5), 4895–4919 (2016). <https://doi.org/10.1021/acs.nano.6b01842>
260. G. Lu, L.E. Ocola, J. Chen, Reduced graphene oxide for room-temperature gas sensors. *Nanotechnology* **20**(44), 445502 (2009). <https://doi.org/10.1088/0957-4484/20/44/445502>
261. M. Zhu, X. Li, S. Chung, L. Zhao, X. Li et al., Photo-induced selective gas detection based on reduced graphene oxide/Si Schottky diode. *Carbon* **84**, 138–145 (2015). <https://doi.org/10.1016/j.carbon.2014.12.008>
262. Metal-Semiconductor Contacts (Ed.), *Physics of Semiconductor Devices* (2006), pp. 134–196. <https://doi.org/10.1002/9780470068328.ch3>
263. K.S. Novoselov, D. Jiang, F. Schedin, T.J. Booth, V.V. Khotkevich et al., Two-dimensional atomic crystals. *Proc. Natl. Aca. Sci. USA* **102**(30), 10451–10453 (2005). <https://doi.org/10.1073/pnas.0502848102>
264. Q.H. Wang, K. Kalantar-Zadeh, A. Kis, J.N. Coleman, M.S. Strano, Electronics and optoelectronics of two-dimensional transition metal dichalcogenides. *Nat. Nanotechnol.* **7**(11), 699–712 (2012). <https://doi.org/10.1038/nnano.2012.193>
265. J. Zhou, Y. Gu, Y. Hu, W. Mai, P.-H. Yeh et al., Gigantic enhancement in response and reset time of ZnO UV nanosensor by utilizing Schottky contact and surface functionalization. *Appl. Phys. Lett.* **94**(19), 191103 (2009). <https://doi.org/10.1063/1.3133358>
266. T.-Y. Wei, P.-H. Yeh, S.-Y. Lu, Z.L. Wang, Gigantic enhancement in sensitivity using schottky contacted nanowire nanosensor. *J. Am. Chem. Soc.* **131**(48), 17690–17695 (2009). <https://doi.org/10.1021/ja907585c>
267. S. McDonnell, R. Addou, C. Buie, R.M. Wallace, C.L. Hinkle, Defect-dominated doping and contact resistance in MoS<sub>2</sub>. *ACS Nano* **8**(3), 2880–2888 (2014). <https://doi.org/10.1021/nn500044q>
268. Y.Y. Illarionov, T. Knobloch, M. Waltl, G. Rzepa, A. Pospischil et al., Energetic mapping of oxide traps in MoS<sub>2</sub> field-effect transistors. *2D Mater.* **4**(2), 025108 (2017). <https://doi.org/10.1088/2053-1583/aa734a>
269. M.C. Hersam, Defects at the two-dimensional limit. *J. Phys. Chem. Lett.* **6**(14), 2738–2739 (2015). <https://doi.org/10.1021/acs.jpcclett.5b01218>
270. F. Banhart, J. Kotakoski, A.V. Krasheninnikov, Structural defects in graphene. *ACS Nano* **5**(1), 26–41 (2011). <https://doi.org/10.1021/nn102598m>
271. P. Vancsó, G.Z. Magda, J. Pető, J.-Y. Noh, Y.-S. Kim et al., The intrinsic defect structure of exfoliated MoS<sub>2</sub> single layers revealed by scanning tunneling microscopy. *Sci. Rep.* **6**(1), 29726 (2016). <https://doi.org/10.1038/srep29726>
272. H. Qiu, L. Pan, Z. Yao, J. Li, Y. Shi et al., Electrical characterization of back-gated bi-layer MoS<sub>2</sub> field-effect transistors and the effect of ambient on their performances. *Appl. Phys. Lett.* **100**(12), 123104 (2012). <https://doi.org/10.1063/1.3696045>
273. K. Barthelmi, J. Klein, A. Hötger, L. Sigl, F. Sigger et al., Atomistic defects as single-photon emitters in atomically thin MoS<sub>2</sub>. *Appl. Phys. Lett.* **117**(7), 070501 (2020). <https://doi.org/10.1063/5.0018557>
274. B. Stampfer, F. Zhang, Y.Y. Illarionov, T. Knobloch, P. Wu et al., Characterization of single defects in ultrascaled MoS<sub>2</sub> field-effect transistors. *ACS Nano* **12**(6), 5368–5375 (2018). <https://doi.org/10.1021/acs.nano.8b00268>



275. G. Lee, G. Yang, A. Cho, J.W. Han, J. Kim, Defect-engineered graphene chemical sensors with ultrahigh sensitivity. *Phys. Chem. Chem. Phys.* **18**(21), 14198–14204 (2016). <https://doi.org/10.1039/C5CP04422G>
276. B. Kumar, K. Min, M. Bashirzadeh, A.B. Farimani, M.H. Bae et al., The role of external defects in chemical sensing of graphene field-effect transistors. *Nano Lett.* **13**(5), 1962–1968 (2013). <https://doi.org/10.1021/nl304734g>
277. H. Terrones, R. Lv, M. Terrones, M.S. Dresselhaus, The role of defects and doping in 2D graphene sheets and 1D nanoribbons. *Rep. Prog. Phys.* **75**(6), 062501 (2012). <https://doi.org/10.1088/0034-4885/75/6/062501>
278. Y.-H. Zhang, L.-F. Han, Y.-H. Xiao, D.-Z. Jia, Z.-H. Guo et al., Understanding dopant and defect effect on H<sub>2</sub>S sensing performances of graphene: a first-principles study. *Comput. Mater. Sci.* **69**, 222–228 (2013). <https://doi.org/10.1016/j.commatsci.2012.11.048>
279. F.A. Villamena, Chapter 2—chemistry of reactive species, in ed. by F.A. Villamena, *Reactive Species Detection in Biology* (Elsevier, 2017), pp. 13–64. <https://doi.org/10.1016/B978-0-12-420017-3.00005-0>
280. O. Leenaerts, B. Partoens, F.M. Peeters, Adsorption of H<sub>2</sub>O, NH<sub>3</sub>, CO, NO<sub>2</sub>, and NO on graphene: a first-principles study. *Phys. Rev. B* **77**, 125416 (2008). <https://doi.org/10.1103/PhysRevB.77.125416>
281. H. Li, M. Huang, G. Cao, Markedly different adsorption behaviors of gas molecules on defective monolayer MoS<sub>2</sub>: a first-principles study. *Phys. Chem. Chem. Phys.* **18**(22), 15110–15117 (2016). <https://doi.org/10.1039/C6CP01362G>
282. H. Qiu, T. Xu, Z. Wang, W. Ren, H. Nan et al., Hopping transport through defect-induced localized states in molybdenum disulphide. *Nat. Commun.* **4**(1), 2642 (2013). <https://doi.org/10.1038/ncomms3642>
283. D. Liu, Y. Guo, L. Fang, J. Robertson, Sulfur vacancies in monolayer MoS<sub>2</sub> and its electrical contacts. *Appl. Phys. Lett.* **103**(18), 183113 (2013). <https://doi.org/10.1063/1.4824893>
284. H.G. Rosa, L. Junpeng, L.C. Gomes, M.J.L.F. Rodrigues, S.C. Haur et al., Second-harmonic spectroscopy for defects engineering monitoring in transition metal dichalcogenides. *Adv. Opt. Mater.* **6**(5), 1701327 (2018). <https://doi.org/10.1002/adom.201701327>
285. M.P.K. Sahoo, J. Wang, Y. Zhang, T. Shimada, T. Kitamura, Modulation of gas adsorption and magnetic properties of monolayer-MoS<sub>2</sub> by antisite defect and strain. *J. Phys. Chem. C* **120**(26), 14113–14121 (2016). <https://doi.org/10.1021/acs.jpcc.6b03284>
286. Y. Linghu, C. Wu, Gas molecules on defective and nonmetal-doped MoS<sub>2</sub> monolayers. *J. Phys. Chem. C* **124**(2), 1511–1522 (2020). <https://doi.org/10.1021/acs.jpcc.9b10450>
287. Y. Linghu, C. Wu, Gas molecules on defective and nonmetal doped MoS<sub>2</sub> monolayers. *J. Phys. Chem. C* **124**(2), 1511–1522 (2020). <https://doi.org/10.1021/acs.jpcc.9b10450>
288. D. Zhao, X. Fan, Z. Luo, Y. An, Y. Hu, Enhanced gas-sensing performance of graphene by doping transition metal atoms: a first-principles study. *Phys. Lett. A* **382**(40), 2965–2973 (2018). <https://doi.org/10.1016/j.physleta.2018.06.046>
289. H.-P. Komsa, S. Kurasch, O. Lehtinen, U. Kaiser, A.V. Krashe-ninnikov, From point to extended defects in two-dimensional MoS<sub>2</sub>: evolution of atomic structure under electron irradiation. *Phys. Rev. B* **88**(3), 035301 (2013). <https://doi.org/10.1103/PhysRevB.88.035301>
290. Y. Jing, X. Tan, Z. Zhou, P. Shen, Tuning electronic and optical properties of MoS<sub>2</sub> monolayer via molecular charge transfer. *J. Mater. Chem. A* **2**(40), 16892–16897 (2014). <https://doi.org/10.1039/C4TA03660C>
291. J. Suh, T.-E. Park, D.-Y. Lin, D. Fu, J. Park et al., Doping against the native propensity of MoS<sub>2</sub>: degenerate hole doping by cation substitution. *Nano Lett.* **14**(12), 6976–6982 (2014). <https://doi.org/10.1021/nl503251h>
292. S. Qin, W. Lei, D. Liu, Y. Chen, In-situ and tunable nitrogen-doping of MoS<sub>2</sub> nanosheets. *Sci. Rep.* **4**(1), 7582 (2014). <https://doi.org/10.1038/srep07582>
293. B.B. Xiao, P. Zhang, L.P. Han, Z. Wen, Functional MoS<sub>2</sub> by the Co/Ni doping as the catalyst for oxygen reduction reaction. *Appl. Surf. Sci.* **354**, 221–228 (2015). <https://doi.org/10.1016/j.apsusc.2014.12.134>
294. J. Dai, J. Yuan, Adsorption of molecular oxygen on doped graphene: atomic, electronic, and magnetic properties. *Phys. Rev. B* **81**(16), 165414 (2010). <https://doi.org/10.1103/PhysRevB.81.165414>
295. Y.-H. Lu, M. Zhou, C. Zhang, Y.-P. Feng, Metal-embedded graphene: a possible catalyst with high activity. *J. Phys. Chem. C* **113**(47), 20156–20160 (2009). <https://doi.org/10.1021/jp908829m>
296. Y. Fan, J. Zhang, Y. Qiu, J. Zhu, Y. Zhang et al., A DFT study of transition metal (Fe, Co, Ni, Cu, Ag, Au, Rh, Pd, Pt and Ir)-embedded monolayer MoS<sub>2</sub> for gas adsorption. *Comput. Mater. Sci.* **138**, 255–266 (2017). <https://doi.org/10.1016/j.commatsci.2017.06.029>
297. H. Luo, Y. Cao, J. Zhou, J. Feng, J. Cao et al., Adsorption of NO<sub>2</sub>, NH<sub>3</sub> on monolayer MoS<sub>2</sub> doped with Al, Si, and P: a first-principles study. *Chem. Phys. Lett.* **643**, 27–33 (2016). <https://doi.org/10.1016/j.cplett.2015.10.077>
298. J. Zhu, H. Zhang, Y. Tong, L. Zhao, Y. Zhang et al., First-principles investigations of metal (V, Nb, Ta)-doped monolayer MoS<sub>2</sub>: structural stability, electronic properties and adsorption of gas molecules. *Appl. Surf. Sci.* **419**, 522–530 (2017). <https://doi.org/10.1016/j.apsusc.2017.04.157>
299. J. Song, H. Lou, Improvement of gas-adsorption performances of Ag-functionalized monolayer MoS<sub>2</sub> surfaces: a first-principles study. *J. Appl. Phys.* **123**(17), 175303 (2018). <https://doi.org/10.1063/1.5022829>
300. O. Leenaerts, B. Partoens, F.M. Peeters, Paramagnetic adsorbates on graphene: a charge transfer analysis. *Appl. Phys. Lett.* **92**(24), 243125 (2008). <https://doi.org/10.1063/1.2949753>
301. J.T. Robinson, F.K. Perkins, E.S. Snow, Z. Wei, P.E. Sheehan, Reduced graphene oxide molecular sensors. *Nano Lett.* **8**(10), 3137–3140 (2008). <https://doi.org/10.1021/nl8013007>
302. J. Heising, M.G. Kanatzidis, Exfoliated and restacked MoS<sub>2</sub> and WS<sub>2</sub>: ionic or neutral species? Encapsulation and ordering of hard electropositive cations. *J. Am. Chem. Soc.* **121**(50), 11720–11732 (1999). <https://doi.org/10.1021/ja991644d>



303. Y. Kim, S.-K. Kang, N.-C. Oh, H.-D. Lee, S.-M. Lee et al., Improved sensitivity in schottky contacted two-dimensional MoS<sub>2</sub> gas sensor. *ACS Appl. Mater. Interfaces* **11**(42), 38902–38909 (2019). <https://doi.org/10.1021/acsami.9b10861>
304. R. Kumar, P.K. Kulriya, M. Mishra, F. Singh, G. Gupta et al., Highly selective and reversible NO<sub>2</sub> gas sensor using vertically aligned MoS<sub>2</sub> flake networks. *Nanotechnology* **29**(46), 464001 (2018). <https://doi.org/10.1088/1361-6528/aade20>
305. T. Xu, Y. Pei, Y. Liu, D. Wu, Z. Shi et al., High-response NO<sub>2</sub> resistive gas sensor based on bilayer MoS<sub>2</sub> grown by a new two-step chemical vapor deposition method. *J. Alloys Compd.* **725**, 253–259 (2017). <https://doi.org/10.1016/j.jallcom.2017.06.105>
306. Y. Zhang, W. Zeng, Y. Li, Hydrothermal synthesis and controlled growth of hierarchical 3D flower-like MoS<sub>2</sub> nanospheres assisted with CTAB and their NO<sub>2</sub> gas sensing properties. *Appl. Surf. Sci.* **455**, 276–282 (2018). <https://doi.org/10.1016/j.apsusc.2018.05.224>
307. Y. Li, Z. Song, Y. Li, S. Chen, S. Li et al., Hierarchical hollow MoS<sub>2</sub> microspheres as materials for conductometric NO<sub>2</sub> gas sensors. *Sens. Actuators B Chem.* **282**, 259–267 (2019). <https://doi.org/10.1016/j.snb.2018.11.069>
308. N.T. Thang, L.T. Hong, N.H. Thoan, C.M. Hung, N. Van Duy et al., Controlled synthesis of ultrathin MoS<sub>2</sub> nanoflowers for highly enhanced NO<sub>2</sub> sensing at room temperature. *RSC Adv.* **10**(22), 12759–12771 (2020). <https://doi.org/10.1039/D0RA0121J>
309. W. Li, Y. Zhang, X. Long, J. Cao, X. Xin et al., Gas sensors based on mechanically exfoliated MoS<sub>2</sub> nanosheets for room-temperature NO(2) detection. *Sensors* **19**(9), 2123 (2019). <https://doi.org/10.3390/s19092123>
310. R. Kumar, N. Goel, A.V. Agrawal, R. Raliya, S. Rajamani et al., Boosting sensing performance of vacancy-containing vertically aligned MoS<sub>2</sub> using rGO particles. *IEEE Sens. J.* **19**(22), 10214–10220 (2019). <https://doi.org/10.1109/JSEN.2019.2932106>
311. N. Barsan, U. Weimar, Conduction model of metal oxide gas sensors. *J. Electroceram.* **7**(3), 143–167 (2001). <https://doi.org/10.1023/A:1014405811371>
312. P. Zhang, X. Lu, Y. Huang, J. Deng, L. Zhang et al., MoS<sub>2</sub> nanosheets decorated with gold nanoparticles for rechargeable Li–O<sub>2</sub> batteries. *J. Mater. Chem. A* **3**(28), 14562–14566 (2015). <https://doi.org/10.1039/C5TA02945G>
313. B.B. Li, S.Z. Qiao, X.R. Zheng, X.J. Yang, Z.D. Cui et al., Pd coated MoS<sub>2</sub> nanoflowers for highly efficient hydrogen evolution reaction under irradiation. *J. Power Sources* **284**, 68–76 (2015). <https://doi.org/10.1016/j.jpowsour.2015.03.021>
314. T.S. Sreeprasad, P. Nguyen, N. Kim, V. Berry, Controlled, defect-guided, metal-nanoparticle incorporation onto MoS<sub>2</sub> via chemical and microwave routes: electrical, thermal, and structural properties. *Nano Lett.* **13**(9), 4434–4441 (2013). <https://doi.org/10.1021/nl402278y>
315. X. Yang, H. Yu, X. Guo, Q. Ding, T. Pullerits et al., Plasmon-exciton coupling of monolayer MoS<sub>2</sub>-Ag nanoparticles hybrids for surface catalytic reaction. *Mater. Today Energy* **5**, 72–78 (2017). <https://doi.org/10.1016/j.mtener.2017.05.005>
316. X. Yang, W. Liu, M. Xiong, Y. Zhang, T. Liang et al., Au nanoparticles on ultrathin MoS<sub>2</sub> sheets for plasmonic organic solar cells. *J. Mater. Chem. A* **2**(36), 14798–14806 (2014). <https://doi.org/10.1039/C4TA03178D>
317. N. Singh, R.K. Gupta, P.S. Lee, Gold-nanoparticle-functionalized In<sub>2</sub>O<sub>3</sub> nanowires as CO gas sensors with a significant enhancement in response. *ACS Appl. Mater. Interfaces* **3**(7), 2246–2252 (2011). <https://doi.org/10.1021/am101259t>
318. V. Dobrokhotov, D.N. McIlroy, M.G. Norton, A. Abuzir, W.J. Yeh et al., Principles and mechanisms of gas sensing by GaN nanowires functionalized with gold nanoparticles. *J. Appl. Phys.* **99**(10), 104302 (2006). <https://doi.org/10.1063/1.2195420>
319. A. Kolmakov, D.O. Klenov, Y. Lilach, S. Stemmer, M. Moskovits, Enhanced gas sensing by individual SnO<sub>2</sub> nanowires and nanobelts functionalized with Pd catalyst particles. *Nano Lett.* **5**(4), 667–673 (2005). <https://doi.org/10.1021/nl050082v>
320. C. Liu, Y. Zhang, J. Hu, J. Ren, Y. Song et al., Defects suppression in MoS<sub>2</sub> caused by W doped for enhanced response/recovery behaviors against NO<sub>2</sub>. *Mater. Lett.* **273**, 127961 (2020). <https://doi.org/10.1016/j.matlet.2020.127961>
321. I.-S. Hwang, J.-K. Choi, H.-S. Woo, S.-J. Kim, S.-Y. Jung et al., Facile control of C<sub>2</sub>H<sub>5</sub>OH sensing characteristics by decorating discrete Ag nanoclusters on SnO<sub>2</sub> nanowire networks. *ACS Appl. Mater. Interfaces* **3**(8), 3140–3145 (2011). <https://doi.org/10.1021/am200647f>
322. S. Kaewgun, C.A. Nolph, B.I. Lee, Enhancing photocatalytic activity of polymorphic titania nanoparticles by NMP solvent-based ambient condition process. *Catal. Lett.* **123**(3), 173–180 (2008). <https://doi.org/10.1007/s10562-008-9490-9>
323. J. Wu, H. Li, Z. Yin, H. Li, J. Liu et al., Layer thinning and etching of mechanically exfoliated MoS<sub>2</sub> nanosheets by thermal annealing in air. *Small* **9**(19), 3314–3319 (2013). <https://doi.org/10.1002/sml.201301542>
324. M.J. Madou, S.R. Morrison, 10—thin-film gas sensors, in eds. by M.J. Madou, S.R. Morrison, *Chemical Sensing with Solid State Devices* (Academic Press, 1989), pp. 419–435. <https://doi.org/10.1016/B978-0-12-464965-1.50015-6>
325. Y. Zhou, C. Gao, Y. Guo, UV assisted ultrasensitive trace NO<sub>2</sub> gas sensing based on few-layer MoS<sub>2</sub> nanosheet–ZnO nanowire heterojunctions at room temperature. *J. Mater. Chem. A* **6**(22), 10286–10296 (2018). <https://doi.org/10.1039/C8TA02679C>
326. B. Cho, A.R. Kim, Y. Park, J. Yoon, Y.-J. Lee et al., Bifunctional sensing characteristics of chemical vapor deposition synthesized atomic-layered MoS<sub>2</sub>. *ACS Appl. Mater. Interfaces* **7**(4), 2952–2959 (2015). <https://doi.org/10.1021/am508535x>
327. G. Chen, T.M. Paronyan, E.M. Pigos, A.R. Harutyunyan, Enhanced gas sensing in pristine carbon nanotubes under continuous ultraviolet light illumination. *Sci. Rep.* **2**(1), 343 (2012). <https://doi.org/10.1038/srep00343>
328. Y. Kang, S. Pyo, E. Jo, J. Kim, Light-assisted recovery of reacted MoS<sub>2</sub> for reversible NO<sub>2</sub> sensing at room temperature. *Nanotechnology* **30**(35), 355504 (2019). <https://doi.org/10.1088/1361-6528/ab2277>

329. J. Wang, J. Deng, Y. Li, H. Yuan, M. Xu, ZnO nanocrystal-coated MoS<sub>2</sub> nanosheets with enhanced ultraviolet light gas sensitive activity studied by surface photovoltage technique. *Ceram. Int.* **46**(8, Part A), 11427–11431 (2020). <https://doi.org/10.1016/j.ceramint.2020.01.157>
330. K. Chang, W. Chen, l-Cysteine-assisted synthesis of layered MoS<sub>2</sub>/graphene composites with excellent electrochemical performances for lithium ion batteries. *ACS Nano* **5**(6), 4720–4728 (2011). <https://doi.org/10.1021/nn200659w>
331. X. Zheng, J. Xu, K. Yan, H. Wang, Z. Wang et al., Space-confined growth of MoS<sub>2</sub> nanosheets within graphite: the layered hybrid of MoS<sub>2</sub> and graphene as an active catalyst for hydrogen evolution reaction. *Chem. Mater.* **26**(7), 2344–2353 (2014). <https://doi.org/10.1021/cm500347r>
332. Y. Niu, R. Wang, W. Jiao, G. Ding, L. Hao et al., MoS<sub>2</sub> graphene fiber based gas sensing devices. *Carbon* **95**, 34–41 (2015). <https://doi.org/10.1016/j.carbon.2015.08.002>
333. Y. Zhou, G. Liu, X. Zhu, Y. Guo, Ultrasensitive NO<sub>2</sub> gas sensing based on rGO/MoS<sub>2</sub> nanocomposite film at low temperature. *Sens. Actuators B Chem.* **251**, 280–290 (2017). <https://doi.org/10.1016/j.snb.2017.05.060>
334. H.S. Hong, N.H. Phuong, N.T. Huong, N.H. Nam, N.T. Hue, Highly sensitive and low detection limit of resistive NO<sub>2</sub> gas sensor based on a MoS<sub>2</sub>/graphene two-dimensional heterostructures. *Appl. Surf. Sci.* **492**, 449–454 (2019). <https://doi.org/10.1016/j.apsusc.2019.06.230>
335. M. Sangeetha, D. Madhan, Ultra-sensitive molybdenum disulfide (MoS<sub>2</sub>)/graphene based hybrid sensor for the detection of NO<sub>2</sub> and formaldehyde gases by fiber optic clad modified method. *Opt. Laser Technol.* **127**, 106193 (2020). <https://doi.org/10.1016/j.optlastec.2020.106193>
336. S. Shao, L. Che, Y. Chen, M. Lai, S. Huang et al., A novel RGO-MoS<sub>2</sub>-CdS nanocomposite film for application in the ultrasensitive NO<sub>2</sub> detection. *J. Alloys Compd.* **774**, 1–10 (2019). <https://doi.org/10.1016/j.jallcom.2018.09.271>
337. M.W. Jung, S.M. Kang, K.-H. Nam, K.-S. An, B.-C. Ku, Highly transparent and flexible NO<sub>2</sub> gas sensor film based on MoS<sub>2</sub>/rGO composites using soft lithographic patterning. *Appl. Surface Sci.* **456**, 7–12 (2018). <https://doi.org/10.1016/j.apsusc.2018.06.086>
338. M. Ikram, Y. Zhao, A.U. Rehman, K. Kan, W. Zhang et al., Multilayer flower like MoS<sub>2</sub> conjugated with thin layer In(OH)<sub>3</sub> for high-performance NO<sub>x</sub> gas sensor at room temperature. *J. Alloys Compd.* **735**, 1439–1448 (2018). <https://doi.org/10.1016/j.jallcom.2017.11.229>
339. R. Kumar, N. Goel, M. Mishra, G. Gupta, M. Fanetti et al., Growth of MoS<sub>2</sub>-MoO<sub>3</sub> hybrid microflowers via controlled vapor transport process for efficient gas sensing at room temperature. *Adv. Mater. Interfaces* **5**(10), 1800071 (2018). <https://doi.org/10.1002/admi.201800071>
340. S. Shi, R. Hu, E. Wu, Q. Li, X. Chen et al., Highly-sensitive gas sensor based on two-dimensional material field effect transistor. *Nanotechnology* **29**(43), 435502 (2018). <https://doi.org/10.1088/1361-6528/aad94d>
341. L. Liu, M. Ikram, L. Ma, X. Zhang, H. Lv et al., Edge-exposed MoS<sub>2</sub> nanospheres assembled with SnS<sub>2</sub> nanosheet to boost NO<sub>2</sub> gas sensing at room temperature. *J. Hazard. Mater.* **393**, 122325 (2020). <https://doi.org/10.1016/j.jhazmat.2020.122325>
342. G. Deokar, P. Vancsó, R. Arenal, F. Ravoux, J. Casanova-Cháfer et al., MoS<sub>2</sub>-carbon nanotube hybrid material growth and gas sensing. *Adv. Mater. Interfaces* **4**(24), 1700801 (2017). <https://doi.org/10.1002/admi.201700801>
343. S. Zhao, Z. Li, G. Wang, J. Liao, S. Lv et al., Highly enhanced response of MoS<sub>2</sub>/porous silicon nanowire heterojunctions to NO<sub>2</sub> at room temperature. *RSC Adv.* **8**(20), 11070–11077 (2018). <https://doi.org/10.1039/C7RA13484C>
344. S. Zhao, G. Wang, J. Liao, S. Lv, Z. Zhu et al., Vertically aligned MoS<sub>2</sub>/ZnO nanowires nanostructures with highly enhanced NO<sub>2</sub> sensing activities. *Appl. Surf. Sci.* **456**, 808–816 (2018). <https://doi.org/10.1016/j.apsusc.2018.06.103>
345. X. Li, Y. Zhou, H. Tai, Y. Jiang, Z. Li, Nanocomposite films of p-type MoS<sub>2</sub> nanosheets/n-type ZnO nanowires: sensitive and low-temperature ppb-level NO<sub>2</sub> detection. *Mater. Lett.* **262**, 127148 (2020). <https://doi.org/10.1016/j.matlet.2019.127148>
346. Z. Yang, D. Zhang, H. Chen, MOF-derived indium oxide hollow microtubes/MoS<sub>2</sub> nanoparticles for NO<sub>2</sub> gas sensing. *Sens. Actuators B Chem.* **300**, 127037 (2019). <https://doi.org/10.1016/j.snb.2019.127037>
347. Y. Han, D. Huang, Y. Ma, G. He, J. Hu et al., Design of hetero-nanostructures on MoS<sub>2</sub> nanosheets to boost NO<sub>2</sub> room-temperature sensing. *ACS Appl. Mater. Interfaces* **10**(26), 22640–22649 (2018). <https://doi.org/10.1021/acsami.8b05811>
348. Y. Han, Y. Ma, Y. Liu, S. Xu, X. Chen et al., Construction of MoS<sub>2</sub>/SnO<sub>2</sub> heterostructures for sensitive NO<sub>2</sub> detection at room temperature. *Appl. Surf. Sci.* **493**, 613–619 (2019). <https://doi.org/10.1016/j.apsusc.2019.07.052>
349. X. Xin, Y. Zhang, X. Guan, J. Cao, W. Li et al., Enhanced performances of PbS quantum-dots-modified MoS<sub>2</sub> composite for NO<sub>2</sub> detection at room temperature. *ACS Appl. Mater. Interfaces* **11**(9), 9438–9447 (2019). <https://doi.org/10.1021/acsami.8b20984>
350. J. Jaiswal, A. Sanger, P. Tiwari, R. Chandra, MoS<sub>2</sub> hybrid heterostructure thin film decorated with CdTe quantum dots for room temperature NO<sub>2</sub> gas sensor. *Sens. Actuators B Chem.* **305**, 127437 (2020). <https://doi.org/10.1016/j.snb.2019.127437>
351. Z. Wang, T. Zhang, C. Zhao, T. Han, T. Fei et al., Rational synthesis of molybdenum disulfide nanoparticles decorated reduced graphene oxide hybrids and their application for high-performance NO<sub>2</sub> sensing. *Sens. Actuators B Chem.* **260**, 508–518 (2018). <https://doi.org/10.1016/j.snb.2017.12.181>
352. S. Cui, Z. Wen, X. Huang, J. Chang, J. Chen, Stabilizing MoS<sub>2</sub> nanosheets through SnO<sub>2</sub> nanocrystal decoration for high-performance gas sensing in air. *Small* **11**(19), 2305–2313 (2015). <https://doi.org/10.1002/sml.201402923>